UNIVERSITY OF SOUTHAMPTON

FACULTY OF ENGINEERING, SCIENCE AND MATHEMATICS

School of Engineering Sciences

Structural Performance of Spacecraft Honeycomb Panels

By

Gabriel Bianchi MEng

Thesis for the Engineering Doctorate Degree

April 2011

UNIVERSITY OF SOUTHAMPTON
SCHOOL OF ENGINEERING SCIENCES

Engineering Doctorate

STRUCTURAL PERFORMANCE OF SPACECRAFT HONEYCOMB PANELS

By Gabriel Bianchi

ABSTRACT

Honeycomb sandwich structures (commonly referred to as honeycomb sandwich panels) have found wide spread application in the aerospace industry thanks to their excellent properties, in particular their high strength-to-weight and high stiffness-to-weight ratios. Surrey Satellite Technology Ltd. (SSTL), like many other space companies, often use honeycomb sandwich panels as part of the primary and secondary structures of the small satellites they develop.

Although honeycomb panels have been used for the past 50 years gaining a better understanding of these sandwich structures, and the methods and solutions used to produce structural assemblies from them is still a major concern in the aerospace industry. Whether directly or indirectly, there are still significant research efforts ongoing that affect these areas. This work focuses on some of these issues and covers several research fields including material science, tribology and adhesive bonding technology.

The first area of focus of this work deals with the structural performance of honeycomb panels alone and mainly concentrates on hexagonal honeycomb cores. An experimental investigation using the rail shear test was conducted to study the shear behaviour of hexagonal honeycomb cores. This involved both static and fatigue tests using numerous honeycomb panel test samples with the loading direction at various angles to the core ribbon. From these tests it was found that core shear strength did not have a linear relationship with loading orientation and that contrary to what is commonly assumed the transverse direction (to the ribbon) is not always necessarily the weakest orientation.

The optimal design and performance of the load introduction points was the second area of focus for this work which covers equipment inserts and bolted joints. Two types of inserts where investigated in this work: hot bonded inserts and cold bonded inserts. A study on hot bonded and cold bonded inserts was conducted to assess their performance and effectively compare the two insert systems. A large portion of the study was experimental and involved carrying out numerous insert pull-out tests to measure static pull strength capability. From the study it was found that contrary to what was expected cold bonded potted inserts outperformed the hot bonded inserts in terms of static strength capability. Using finite element it was found that this was due to the different filler materials used for the two insert systems.

The last area covered in this work concerns friction grip bolted joint between honeycomb panels. Here a simple method to analyze the efficiency of shear joint units is proposed. An extensive test campaign was also carried out to determine the influence of various parameters on the friction coefficient. Surface abrasion was found to be a reliable way of achieving high values of friction coefficient.

Contents

List of Figures

List of Tables

Nomenclature

Abbreviations and Acronyms

ASTM	American Society for Testing and Materials
CAD	computer aided design
CFRP	carbon fibre reinforced plastic
ESA	European Space Agency
FEA	finite element analysis
FE	finite element
GRP	glass reinforced plastic
IDH	Insert Design Handbook
LVDT	linear variable differential transformer
MPC	multi point constraint
SQM	structural qualification model
SSTL	Surrey Satellite Technology Ltd.

List of Symbols

A_{bob}	area of bobbin insert surface in contact with one face sheet
b	potting radius
b_R	real potting radius
c	core thickness
C*	$= \beta/(\beta+1)$
D	cumulative fatigue damage
E	Young's Modulus
F_{kreq}	minimum preload value required for friction grip
F_M	preload in each bolt
F_Q	externally applied shear load
f	facing sheet thickness
G_S	shear modulus of cell wall base material
G_{xz}	core shear modulus in the L (ribbon) direction
G_{yz}	core shear modulus in the W direction
H	surface hardness
h_i	insert height
h_p	potting height
K	hardness coefficient
Kcr	shear buckling instability factor
K_G	core shear modulus factor
K_T	torque coefficient
l	$l=l_1=l_2$
l_c	coupon length
l_1	length of inclined cell wall
l_2	length of ribbon direction cell wall
m	number of bolts
N	number of cycles
n	number of faying surfaces
P	load
P_{SS}	static strength capability of insert
P_{crit}	insert strength capability for core shear failure
$P_{P,crit}$	insert strength capability for tensile failure of the core underneath the potting

$P_{R,crit}$	insert strength capability for failure of the potting underneath the insert
P_{NR}	load carried by tensile stress in the potting
$P_{NR,crit}$	critical load carried by tensile stresses in the potting
P_{Shear}	insert shear strength
p	thread pitch
R	fatigue stress ratio
R_a	average surface roughness
r	radial distance from insert centre
r_b	effective bearing radius of the bearing contact area under the head or nut
r_t	effective contact radius between threads
$r_{\tau,max}$	radial position of maximum core shear stress
Sr	slip resistance
T	torque
T_p	preload torque
T_t	thread friction torque
T_b	bearing friction torque
t	Single cell wall thickness
t'	Doubble cell wall thickness = 2t
u	displacement
V	equivalent volume of cell
V_i	volume of ith cell wall
w	coupon width
α	half angle of the thread profile angle
β	c/f
γ	strain
η	adhesion parameter
θ	angle of inclined cell wall
μ_b	friction coefficient between the bearing surfaces of the bolt head or nut
μ_S	slip coefficient
μ_t	thread friction coefficient
υ	Poisson's ratio
$\sigma_{C,crit}$	tensile or compressive strength of the core
$\sigma_{R,crit}$	tensile strength of the potting

σ_{max}	maximum stress
σ_{mix}	minimum stress
$\tau_{ad,crit}$	critical shear strength of adhesive
$\tau_{C,crit}$	circular shear strength of the core
τ_{max}	maximum core shear stress
τ_{xz}	shear stress in the L (ribbon) direction
τ_{yz}	shear stress in the W direction
Ψ	plasticity index

Acknowledgments

First of all, I would like to thank Prof. Guglielmo Aglietti for his academic supervision throughout my Engineering Doctorate (EngD). His sound technical advice and guidance has been invaluable, and his constant support and encouragement really spurred me on at the right times. Similarly I would also like to thank Dr. Guy Richardson who acted as my industrial supervisor. The advice he gave me from his direct involvement in numerous spacecraft development programs over the years was also invaluable and helped me ensure that the work I was doing was relevant to the challenges currently faced by the industry within my area of research.

My EngD was sponsored by Surrey Satellite Technology Ltd. (SSTL) and their financial and technical support is gratefully acknowledged. SSTL also supplied most of the test samples which were used in my experimental work.

Next, I would like to thank my Mum and Dad for their moral and emotional support and for cheering me up during the tougher times of my doctorate. Special thoughts go to my Nan who unfortunately passed away before I could finish my thesis. She was always very kind to me and was very proud of the work I was doing. I would also like to thank my uncle, Jeremy, who really fostered my interest in the technical world by taking me to exhibitions and museums when I was a little boy.

Apart from my supervisors other people have also provided me with assistance during the course of my EngD. In particular I would like to acknowledge the help of the following two people: Mr. David Costello for making sure that I was always nicely stocked up on test coupons from SSTL; Mr. Simon Klitz for modifying and making up special parts for my tests.

Lastly, I would like to thank all my friends who have made my time in Southampton so enjoyable and fun with coffee breaks, squash games, outings, parties and all sorts of activities that distracted me from my work. Special thanks go to Michele and Stefano who were kind enough to let me stay at theirs when I was based in Guildford and had work to do in Southampton. I would also like to thank Stefano for kindly assisting me with the printing operations and the submission of the first draft of this thesis while I was busy working at SSTL.

Declaration of Authorship

I, **Gabriel Bianchi** declare that the thesis entitled **Development of Efficient and Cost-effective Spacecraft Structures based on Honeycomb Panel Assemblies** and the work presented in the thesis are both my own, and have been generated by me as the result of my own original research. I confirm that:

- this work was done wholly or mainly while in candidature for a research degree at this University;
- where any part of this thesis has previously been submitted for a degree or any other qualification at this University or any other institution, this has been clearly stated;
- where I have consulted the published work of others, this is always clearly attributed;
- where I have quoted from the work of others, the source is always given. With the exception of such quotations, this thesis is entirely my own work;
- I have acknowledged all main sources of help;
- where the thesis is based on work done by myself jointly with others, I have made clear exactly what was done by others and what I have contributed myself;
- Parts of this work have been published as listed in Appendix A.

Signed: ……..

Date:……

Chapter 1

1 Introduction

1.1 Background

Honeycomb panels are widely used in the aerospace industry due to their high specific strength and stiffness properties. At Surrey Satellite Technology Ltd. (SSTL) honeycomb panels are extensively employed in the primary and secondary structures of the small spacecraft they develop. In the past 25 years SSTL has gained significant heritage in designing and producing small satellites in the 50-600 kg range (an example of one of these satellites can be seen in Figure 1-1).

Figure 1-1: Artist impression of Giove-A in orbit (image © ESA)

However, most of this heritage has been gained from SSTL's early work developing microsatellites in the 50-100 kg range. The structure of these traditional SSTL spacecrafts were constructed from machined metallic components and only a

small amount of honeycomb panels were used as secondary structures. This design approach works well for very small spacecrafts but it is not mass efficient for larger spacecraft. In 2003 SSTL began work on its first large spacecraft using structural honeycomb panels. This spacecraft development was unusual in that no mass optimization was carried out at all. Instead a simple and lower cost approach using standard (over engineered) joint connections consisting of large aluminum block inserts in the panel and five Titanium M5 fixings per block was taken. Even with this over engineered approach there were issues with these joints which highlighted the importance of considering the efficiency of these structural connections. The honeycomb panels were also over engineered due to the limited knowledge of their structural dynamic performance.

Hence there was a desire to gain a better understanding of honeycomb sandwich structures and the methods and solutions used to develop more efficient structural assemblies from them. This is a key requirement for the development of more efficient spacecraft structures leading to the following benefits:

- Achieving confidence in design without having to rely on over conservative factors of safety or extensive test campaigns.

- Greater freedom to explore potentially advantageous new design solutions without having to rely heavily on heritage.

- Exploit the structural capabilities of honeycomb panels to a greater extent and drive down mass.

Despite the fact that honeycomb panels have been around since the ‘60s, gaining more confidence on their structural capabilities and a better understanding of the techniques used to join them to other honeycomb panels or structural components are still major concerns to the whole aerospace industry and not just SSTL. The fact that significant research efforts are still ongoing in these areas confirms that

there is still significant room for improvements. These areas represent the main focuses of this work.

1.2 Drive for More Efficient Spacecraft Structures

A spacecraft is subjected to various environments during the arc of its life. From a structural point of view the most important environmental condition is usually launch during which the highest mechanical loads are seen. The launch environment is characterized by multiple load sources which occur during different stages of the launch. There are quasi-static loads generated from thrust when the engine is burning steadily. There are transient loads occurring when the engines ignite and shut down. Acoustic loads generated by engine rumble consisting of sound pressure waves with many different frequencies which cause the structure to vibrate randomly. Finally there are shock loads (pyro shocks) generated by the pyrotechnic devices commonly used to separate the stages of the launcher. These are characterized by high frequency (> 1000 Hz), high intensity vibrations. Therefore the structure must be strong enough to withstand high quasi-static loads, harsh dynamic loads and shock loads. However, due to the high cost of launching satellites into orbit (which can reach as much as 50% of mission costs [1]), the structure also needs to be light. This means that satellites need to be designed with a high degree of structural efficiency and that there is a constant desire to improve this efficiency.

1.3 Scope

The areas of interest described so far are very broad so the research work had to be focused and prioritized on more specific topics which were considered of greater practical importance. The scope of the project can be summarized as follows:

- Honeycomb Panels
    - Static shear strength of honeycomb cores
    - Fatigue shear strength of honeycomb cores

- Equipment Inserts
    - Static strength capability of hot bonded and cold bonded inserts
    - Influence of insert system filler material on static strength capability
- Bolted Joints
    - Mass efficiency of bolted joint units
    - Friction between the faying surfaces of in-plane bolted joints

These areas are briefly introduced and described in the following subsections. They are then covered in full detail in the relevant chapters.

1.4 Development of Spacecraft Structures

The structure has a very important function; it interfaces with the launch vehicle and holds all the other components in their specified arrangement making the spacecraft function as a whole. The structure also has the role of protecting the components from negative radiation and thermal environments, and providing thermal paths for components that need to dissipate heat. The structure must provide mounting of all the components connecting them to one another transferring loads between them without undergoing failure or subjecting the components to loads which would cause them to fail. Another requirement for the structure is to minimize the transmissibility of microvibrations generated during in-orbit operation by moving parts on the spacecraft (e.g. reaction wheels) which may adversely affect sensitive payloads or instruments. For earth observation satellites and space telescopes this is becoming an incrisingly important requirement due to the development of evermore capable and sensitive optical payloads.

Developing an efficient spacecraft structure is a challenging undertaking, involving several iterations of design, analysis and test. The books by Sarafin [2] and Wijker

[3] provide most of the fundamental information on the design and development of spacecraft structures.

The first step is to define the requirements, which is closely followed and runs in parallel with, configuring the spacecraft, developing concepts and carrying out trade studies whilst considering costs of analysis, manufacturing, test and operation.

For the initial concept the focus is on meeting the most challenging requirements. As the initial concept is developed further more detailed requirements are being generated, those then flow to the next design iteration. Several iteration cycles are generally necessary before a specific configuration is settled upon and it is possible to move on to detailed design development. The whole process involves a large amount of analysis work covering: structural dynamics, stress analysis, stiffness, thermoelastics, and mass property predictions (centre of gravity and inertia tensor). The work carried out here makes most of its contributions in the stress analysis and dynamic load analysis of spacecraft structures.

The analysis of dynamic loads involves predicting natural frequencies, modes of vibration, damping and response to time varying forces and vibrations. This is a very important and challenging part of the analysis work. Another book by Wijker provides most of the basic knowledge in this field [4].

Most of the analysis work involves developing mathematical models of the spacecraft to represent its structural characteristics such as stiffness and mass properties. The most commonly used tool for analyzing spacecraft structures is the finite element method (FEM). Using FEM it is possible to model complex structures by analytically representing them with mass and stiffness matrices which can be solved using computers. FEM is extensively used in almost every stage of developing a spacecraft structure.

FE models are generated based on up-to-date CAD models, and are analysed to determine the structural characteristics of the spacecraft. The results are then used to update and improve the efficiency of the design from the original baseline. Some of the main results that are obtained from the FE models are the panel stresses, the joint loads, and the equipment inserts loads. A good knowledge of the behavior and the allowables of these structural elements is key in order to appropriately modify the design of the structure. It is in this iterative loop that this research work has its main contributions.

1.5 Honeycomb Panels

Honeycomb sandwich construction is a reliable and cost effective way of producing high strength, lightweight spacecraft structures. Sandwich technology is well established and has been well understood since the mid 1960s [5,6]. Amongst the many types of sandwich structures developed to date, honeycomb panels are one of the best known and most utilized. Honeycomb panels are advanced sandwich consisting of low modulus lightweight cellular (honeycomb) core sandwiched between high modulus, high strength face sheets (see Figure 1-2). The assembly maximizes stiffness-to-weight ratio and bending strength-to-weight ratio, resulting in a panel structure that is particularly effective at carrying distributed loads.

One of the main properties defining the structural performance of a honeycomb panel is the core type. Apart from maintaining a separation between the two face sheets to increase the bending stiffness of the panel, the honeycomb core also has the role carrying out-of-plane shear stresses. In order to select the appropriate honeycomb cores it is key to have accurate and reliable information about their structural performance. This is why a study was carried out to investigate the static and dynamic shear behavior of some of the hexagonal honeycomb cores typically used at SSTL.

The core fatigue work carried out as part of this thesis has resulted modifications to how SSTL analyses and optimizes it honeycomb panels and provided the material allowables that are used in this activity.

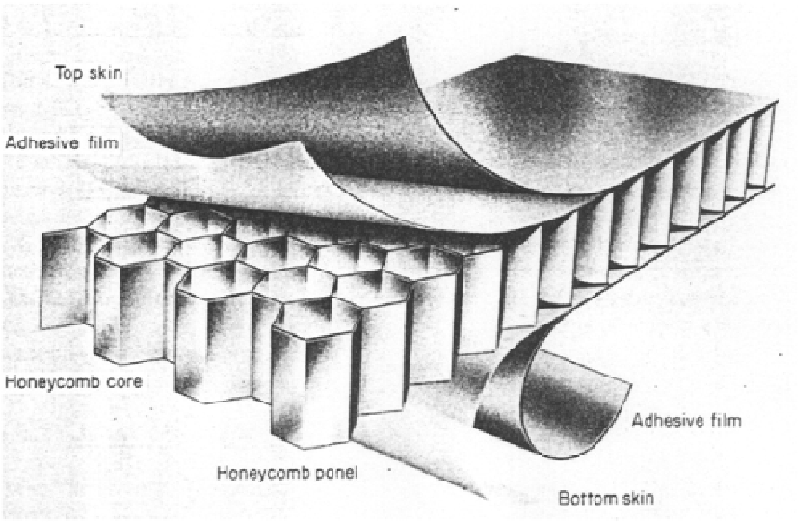

Figure 1-2: Honeycomb panel sandwich construction [2]

1.6 Equipment Inserts

Because of the weakness of the core, honeycomb sandwich structures are not suited to carrying point or line loads. Under such loading conditions, the soft honeycomb core can crush, leading to several modes of failure. This problem is normally solved by the introduction of a hard point (often in the form of a metallic insert), at the point of loading. Hence, inserts provide a means of effectively attaching equipment or other structural elements to the honeycomb panel without adding significant additional weight. Although inserts have been widely used in the aerospace industry, little material has been published in the field.

Inserts can be split in two important categories depending on the method of integration into the honeycomb panel; hence a distinction is made between hot bonded inserts and cold bonded inserts. Hot bonded inserts are integrated during sandwich panel production; whereas cold bonded inserts are potted with curing resin into an existing panel.

Cold bonded inserts are the most used type of inserts in the space industry and have been studied to a greater extent compared to hot bonded inserts which are normally used at Surrey Satellite Technology Ltd. (SSTL). Amongst the limited works published so far on the topic of inserts in general, none specifically focus on hot bonded inserts. This lack of knowledge is of concern to designers at SSTL. To address this, one of the project aims is to conduct a study on hot bonded inserts to assess their performance and effectively compare them with cold bonded inserts. The study was largely experimental and involved conducting numerous insert pull-out tests on both types of inserts.

1.7 Bolted Joints between Honeycomb Panels

Honeycomb panels are normally connected via bolted joints. Bolted joints exhibit many advantages e.g. ease of assembly, reassemblage, repairing of damaged structural parts, and contribute to structural damping [7]. As with the attachment of equipment, a local reinforcement of the core is required at the panel edge where the joint is to be placed. This feature makes this type of bolted joints different and slightly more complex than conventional ones.

Bolted connections between honeycomb panels are normally designed as friction grip joints were the external loads are carried by frictional resistance between the faying surfaces. Sufficient frictional resistance is ensured by applying sufficient preload to the clamped parts of the joint.

One of the disadvantages in using bolted joints and mechanical fastenings in general is that they add more mass than other attachment methods such as welds or adhesive bonds [2]. In a spacecraft where the primary structure consists of an assembly of honeycomb panels, bolted joints can represent a significant proportion of the mass of the structural subsystem. Considerable mass savings can thus be gained by improving the efficiency of bolted connections in terms of load carrying capability per unit mass. In light of this, work was carried out to develop a

procedure to minimize the mass of bolted connections while maintaining structural reliability.

One of the ways in which this can be achieved is to increase the friction coefficient between the faying parts of the joint. The higher the friction coefficient the less clamping force is required to maintain friction grip conditions meaning that smaller and lighter bolts can be used. Countless works have been published on the topic of friction since the first laws of friction were defined by Guillaume Amontons [8] in the late 17th century. However, most of the modern research in this field focuses on ways to reduce friction and wear. Hence a study was carried out to investigate methods for increasing friction and achieving consistently high values of friction coefficient for friction grip joint applications.

The joint optimisation work carried out as part of this thesis was used as the basis of the standard honeycomb panel joints currently used on all SSTL new spacecraft. This includes the NigeriaSat-2 spacecraft which was successfully launched in August 2011 and GMPT, SSTL's 3.5 tonne geostationary spacecraft which is currently under development and will undergo it first structural qualification test in 2012. The joint friction work has been picked up by SSTL and is a current R&D activity. SSTLs intention is to incorporate controlled friction surfaces into the standard honeycomb panel structural joints for all large spacecraft from 2012 onwards.

1.8 Structure of Thesis

The thesis is comprised of 8 Chapters. Since more than one area was covered in this work the literature review is spread across the chapters according to the topics covered rather than being concentrated in one single chapter at the beginning. The main body of the thesis is organized in the following parts corresponding to the main areas that were covered:

1. Honeycomb Core (Chaps. 2 and 3)
2. Equipment Inserts (Chap. 4)
3. Bolted Joints between Honeycomb Panels (Chaps. 5-7)

The contents of the individual chapters are briefly described in what follows:

Chapter 2 provides an introduction to the work carried out on the behavior of honeycomb cores under out-of-plane shear stresses. The chapter describes the test campaign that was conducted as part of this study together with the results that were obtained. From these results it is shown how the shear strength and the shear stiffness of the tested cores were found to have a non-linear relationship with loading orientation.

Chapter 3 covers the finite element investigation that was carried out to further investigate the relationship between loading orientation and the behavior of the honeycomb core. From the results presented it is shown that this behavior is mainly due to the fact that, if the loading is not aligned with one of the principal orientations, the displacement of the core is not aligned with the loading direction. In this chapter it is also shown how it was possible to model the core failure behavior using non-linear finite element analysis.

Chapter 4 covers the second area of focus of this work which deals with equipment inserts. The chapter describes the test campaign that was carried out on hot bonded and cold bonded inserts to investigate their pull-out performance. From the results presented it is shown, despite their weaker form of construction, the tested cold bonded inserts had higher pull-out strength than the hot boned inserts. The chapter also presents the finite element study that was carried out to further investigate the two insert systems. From the results of this study it is demonstrated that this difference is mainly due to the different filler materials used for the two insert systems.

Chapter 5 introduces the third area of focus of the thesis which concentrates on bolted joints between honeycomb panels. The chapter contains most of the literature review relevant to this area of focus. The chapter also presents a simple method used to improve the efficiency of bolted joints.

Chapter 6 presents the test campaign that was carried out to investigate the performance of friction grip joints. From the results presented it is shown how controlled surface abrasion can be used to increase the friction coefficient of these joints.

Chapter 7 presents the test campaign that was conducted to investigate the bearing behavior of the joints tested for friction in Chapter 6. From these tests it was possible to obtain useful data regarding the shear strength hot bonded inserts.

Chapter 8 summarizes the major conclusions of the thesis.

Chapter 2

2 Honeycomb Cores under Out-of-plane Shear Stresses

2.1 Introduction

Despite the many attributes of honeycomb panels, as for other advanced composites, their application in primary aircraft and spacecraft structures has been limited in the past by the poor knowledge of their behavior under complex static and dynamic loads. In fact, even though these sandwich composites have been studied since they were first developed, research efforts are still ongoing in order to gain a better understanding of their static and fatigue behavior and make their use more widespread and attractive in more demanding structural applications.

The honeycomb core has a major influence on the structural performance of a honeycomb panel. It provides a separation between the two face sheets increasing the second moment of inertia and hence the overall stiffness of the panel. However, the core must also be stiff enough to ensure that when the panel is bent, the two face sheets do not slide over each other. This is mainly depends on the out-of-plane shear moduli of the core. The determination of this mechanical property is thus very important but, as will be explained in what follows, is also a complex task.

One of the main advantages of honeycomb panels and sandwich panels, is that their stiffness characteristics be controlled based on the geometrical parameters of the core. Hence the designer can optimize the panel design to the final application. However, the designer will also need reliable information about the strength performance of the cores he can choose from. For standard aerospace cores the principal static strength properties can be generally found in manuals and standards (e.g. ESA Composite Design Handbook [9]). However, these do not provide much information regarding their fatigue performance. During acceptance testing, transport, and launch a spacecraft panel will see many load cycles (up to ~300,000). Obtaining more reliable information about the fatigue behavior of these

honeycomb cores is very important when considering their use in these demanding applications. However, at present, there appears to be gap in the literature concerning the behavior of honeycomb cores under dynamic out-of-plane shear stresses.

The variation of static core shear strength and shear modulus with loading orientation is another area which has not been investigated in the literature. These areas represent the focus of the work presented here which is based on an extensive test campaign carried out to investigate the shear behavior of aluminum alloy hexagonal honeycomb cores under both static and cyclic loads. The test campaign involved conducting both static and fatigue rail shear tests in accordance with ASTM standards C273 and C394 [10,11] respectively. The results obtained from the static tests were further investigated using the finite element method to model the failure modes.

2.2 Literature Review and Principal Knowledge

Much research work has been carried out on sandwich construction and on honeycomb cores in past. The fundamentals of sandwich construction and reviews of experimental and analytical methods are described in an early works by Allen [12], Plantema [5] and Marshal [13], and recent works by Zenkert [14] and Vinson [15]. A significant proportion of the works published in this area focus on the static mechanical properties of honeycomb cores. Due to their particular geometry, honeycomb cores are highly orthotropic and exhibit significantly different properties from their isotropic base material. Nine material parameters are required to describe the mechanical behavior of honeycomb cores: the two in-plane Young's moduli (E_x, E_y), the out-of-plane Young's Modulus (E_z), the in-plane shear modulus (G_{xy}), the out-of-plane shear moduli (G_{xz}, G_{yz}), and the three Poisson's ratios (υ_x, υ_y, υ_z). An image illustrating the coordinate system adopted in this work for the above symbols is shown in Figure 2-1.

Many theoretical and experimental approaches can be found in the literature to determine the equivalent material properties of honeycomb cores. An extensive list of these can be found in Noor et al. [16] and more recently in Hohe and Becker [17]. In Schwingshackl et al [18] several of these analytical and experimental methods are examined and compared with the results obtained from ASTM standard tests. In this work an alternative dynamic method is also proposed to obtain the orthotropic mechanical properties of honeycomb cores.

Gibson and Ashby [19] studied the in-plane stiffness of honeycomb cores according to the bending model of cell edges. Masters and Evans [20]developed a theoretical model for predicting the in-plane elastic stiffness of honeycomb cores based on the deformation of honeycomb cells. Becker [21] studied the effective in-plane stiffness of honeycomb cores and the thickness effect using the closed form description.

The determination of the out-of-plane shear moduli of honeycomb cores is more challenging. Several noteworthy works [19,22-25] have been published in this area. These are of particular relevance to this work and are covered in more detail in the following subsections.

To present date, few studies have been conducted on the shear strength and shear failure modes of honeycomb cores. In Heimbs [26]a virtual testing technique using dynamic finite element simulation is proposed as an alternative to costly prototype testing when considering new sandwich core designs. The technique was developed to predict both the mechanical behavior and the failure mechanism and a comparison of numerical and experimental results is presented for Nomex honeycomb core and two types of foldcore. Lee *et al*. [27] investigated the compressive and shear deformation behavior and failure mechanism of sandwich composites consisting of Nomex honeycomb cores and 2024 aluminium alloy face sheets. Pan *et al*. [28] experimentally investigated the shear deformation behavior and failure process of 5056 aluminum alloy honeycomb cores using the single

block shear test and compared the results with a theoretical model based on shear strength formulas for thin plates.

As explained earlier the fatigue performance of honeycomb cores is also important when considering their use for spacecraft applications. The basics of material fatigue are covered in section 2.2.2. Although several works have been published on the fatigue performance of composites in general, the ones that specifically focus on honeycomb cores are relatively few. Belouettar et al. [29] carried out an experimental investigation on the fatigue behavior of aluminum and composite honeycomb materials using the four point bend test method. Hwang and Han [30] proposed using modulus variation as a means of monitoring fatigue damage in composites. Several investigators [31-33] have considered the effectiveness of stiffness degradation in composite materials as a way of measuring damage accumulation. It is generally recognized that residual strength exhibits minimum decrease with increasing number of cycles until very close to the end of life of the specimen, when it changes very abruptly and then failure occurs. On the other hand the investigators that propose modulus variation concept for fatigue monitoring have noticed a more gradual variation of stiffness with fatigue life for the specimens they have tested. However, this was not seen by Belouttar et al [29] for the honeycomb cores they tested, instead the stiffness varied in a similar manner to the strength.

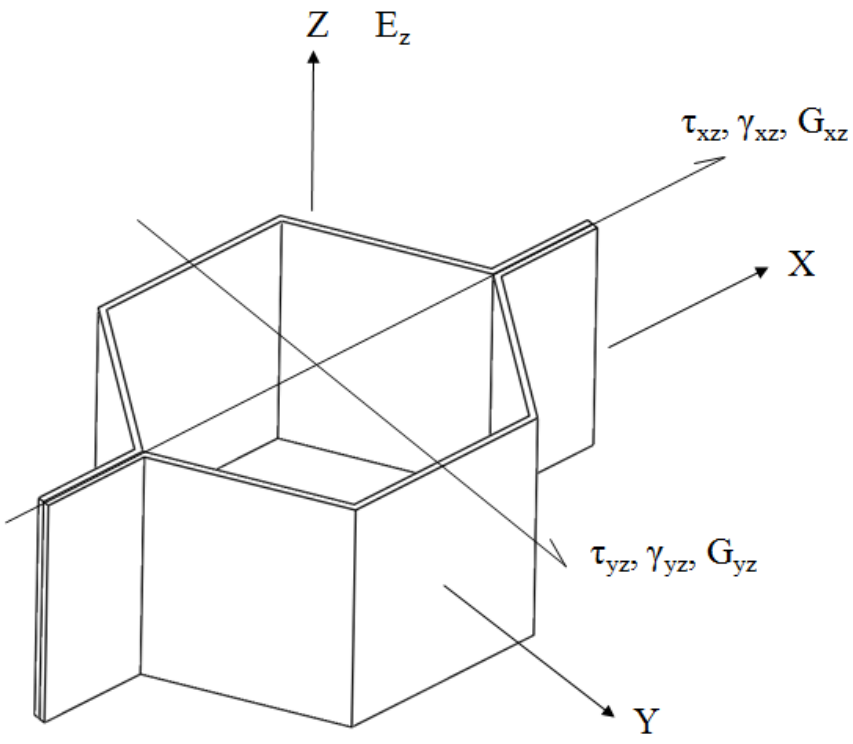

Figure 2-1: Single honeycomb cell illustrating the adopted coordinate reference system

2.2.1 Calculation of the Shear Moduli of Honeycombs

Theories exist for all of the nine orthotropic properties of honeycomb cores. But the determination of the out-of-plane shear moduli, which are most relevant to this work, is particularly complicated. The stress distribution in a sheared honeycomb is not simple; each cell wall is subjected to a non-uniform deformation due to the constraints placed on its neighbours, and the initially plane honeycomb may not remain plane. Exact calculations are only possible using numerical methods. Amongst the analytical methods available it is possible to define two fundamental approaches: the energy methods and the laminate theory methods. These are covered in the following subsections.

2.2.1.1 Energy Method

Upper and lower bounds for the two shear moduli can be formulated relatively easily using a method proposed by Kelsey et al [22] and Gibson and Ashby [19].

The two bounds are obtained using the theorems of minimum potential energy and of minimum complementary energy proposed by Shames [23]. The first theorem gives the upper bound. It states that the strain energy calculated from any postulated set of displacements which are compatible with the external boundary conditions and with themselves will be a minimum for the exact displacement distribution. The theorem can be expressed as an inequality which for the shear in the x direction takes the form

$$\frac{1}{2}G_{xz}\gamma_{xz}^2 V \le \frac{1}{2}\sum_i \left(G_s \gamma_i^2 V_i\right) \qquad \textbf{(2-1)}$$

where V is the equivalent cell volume, γ_{xz} is the equivalent cell strain, G_s is the shear modulus of the cell wall base material, γ_i are the shear strains in the three cell walls and V_i are their volumes.

The second theorem provides a lower bound for the moduli. It states, that, among the stress distributions that satisfy equilibrium at each point and are in equilibrium with the external loads, the strain energy is a minimum for the exact stress distribution. For the x direction it can be expressed as the following inequality

$$\frac{1}{2}\frac{\tau_{xz}^2}{G_{xz}}V \le \frac{1}{2}\sum_i \left(\frac{\tau_i^2}{G_s}V_i\right) \qquad \textbf{(2-2)}$$

For honeycomb cores produced from metal foil using the expansion process (i.e. for $t'/t = 2$), it can be shown that, evaluating the above theorems for the relevant directions, the following shear moduli can be found for the x and y directions

$$\frac{l_2/l_1 + \sin\theta}{(1+l_2/l_1)(l_2/l_1)\cos\theta}\left(\frac{t}{l_2}\right) \le \frac{G_{xz}}{G_s} \le \frac{l_2/l_1 + \sin^2\theta}{(l_2/l_1+\sin\theta)(l_2/l_1)\cos\theta}\left(\frac{t}{l_2}\right) \qquad \textbf{(2-3)}$$

$$\frac{G_{yz}}{G_s} = \frac{\cos\theta}{l_2/l_1 + \sin\theta}\left(\frac{t}{l_2}\right) \qquad \textbf{(2-4)}$$

where l_1, l_2, t and θ are geometrical properties of the honeycomb cell which are explained in Figure 2-2. From Eq. 2-4 it can be seen that for the y direction both theorems give the same solution. The two bounds are also equal in the x direction for regular hexagonal cells if the wall thicknesses are all equal. This however is not normally the case since the expansion process commonly used to produce honeycomb cores results in cell walls with double thickness in the ribbon direction.

Grediac [24] used the finite element method to study the shear moduli of honeycomb cores and compared the results with the upper and lower bounds obtained from the two energy theories. A representative unit cell was modeled and the height of the cell, c, was varied to see how it influenced the shear modulus G_{xz}. The following relationship was thus found

$$G_{xz} = G_{xz}^{low} + \frac{k_G}{c/l_1}\left(G_{xz}^{high} - G_{xz}^{low}\right) \qquad \textbf{(2-5)}$$

where c/l_1 is the aspect ratio of the cell wall, and k_G is a real number. For the hexagonal cell geometries considered in this work a k_G value of 0.787 was found based on the calculated moduli from the FE models.

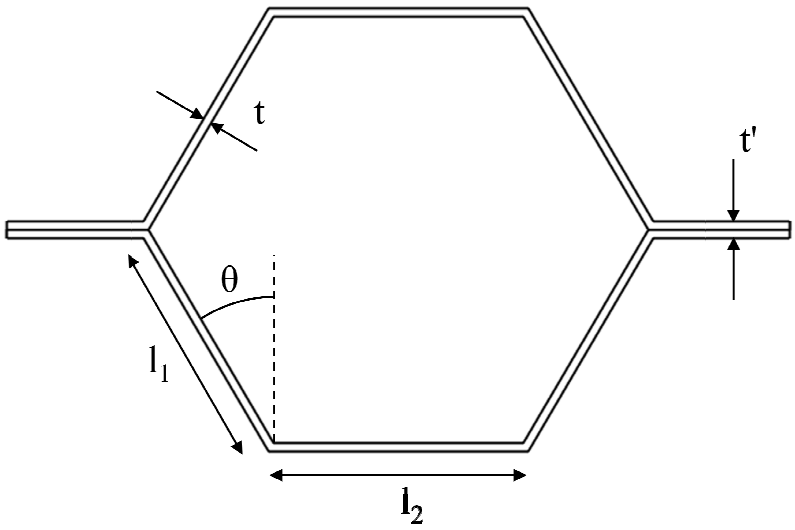

Figure 2-2: Geometry of representative honeycomb cell

2.2.1.2 Laminate Theory Method

Meraghni *et al* [25] also developed an analytical method to analyze the out-of-plane shear moduli of honeycomb cores. The method is based on the laminate theory which was modified and adapted to core materials. The advantage of this method is that it can be applied to different core geometries – the model was also adapted to tubular core in this paper. For hexagonal cores produced via the expansion process, the shear moduli obtained using this method are as follows

$$\frac{G_{xz}}{G_s} = \frac{1}{2}\frac{(1+\sin\theta)}{\cos\theta(\sin\theta+1)}\left(\frac{t}{l_1}\right) \quad \textbf{(2-6)}$$

$$\frac{G_{yz}}{G_s} = \frac{1}{2}\frac{(t+l_1\sin\theta)}{(1+\sin\theta)(t+l_1\cos\theta)}\left(\frac{t}{l_1}\right) \quad \textbf{(2-7)}$$

In [25] this analytical method was used to study how the mechanical properties of hexagonal and tubular cores are influenced by variations in the geometrical parameters (e.g. core height, cell size, etc.). The results from the analytical models were compared with experimental and FEM data and a good agreement were generally found.

2.2.2 Fatigue

Material fatigue is a phenomenon by which structural damage is accumulated as a result of cyclic loading. Fatigue can lead to failures at stress levels significantly lower than the material's ultimate tensile stress or yield stress. Fatigue is becoming an increasing concern in spacecraft structures. The advances in stress and load prediction methods have led to the development of evermore efficient and highly stressed structures. The expectation on mission durations has also increased, resulting in greater loading and thermal cycles. Unfortunately, as stress levels and load cycles have increased, many of today's high performance materials cannot resist fatigue damage as well as the lower strength materials commonly used

decades ago. Honeycomb cores are particularly susceptible to fatigue damage due to out-of-plane shear stresses resulting from cyclic panel bending loads.

Fatigue initiates by the formation of microscopic cracks at the surface which grow with every load cycle until a critical crack length is reached, at which point failure occurs. Fatigue cracks always begin at stress concentrations coinciding with discontinuities in the surface (e.g. sharp corners or surface imperfections). Fatigue is of concern whenever a part is characterized by stress concentrations or has to undergo a high number of stress cycles. Honeycomb cores are not characterized by significant stress concentrations; however, for spacecraft applications a typical honeycomb panel will undergo a high number of loading cycles during qualification vibration testing and launch.

By conducting cyclic load tests on standard sized specimens, it is possible to gather fatigue design data which is normally depicted with S-N curves, showing stress levels versus number of cycles to failure (see Figure 2-3). S-N data is generally characterized by a high scatter and more than one data point is required at each stress level in order to obtain a statistically representative curve of best fit. This makes fatigue testing particularly time consuming and costly.

The fatigue life (i.e. number of cycles to failure) mainly depends on the peak stress σ_{max}, the stress concentration factor, K_t, and the stress ratio,

$$R = \frac{\sigma_{min}}{\sigma_{max}} \tag{2-8}$$

which is the ratio of minimum to maximum stress. The most severe loading environment occurs when the stress is fully reversed, $\sigma_{min} = -\sigma_{max}$, resulting in R=-1. In general S-N curves flatten out with increasing number of cycles, and become asymptotic to the fatigue endurance limit, which is the stress level at which the part can withstand an infinite number of cycles. However, not all materials have an endurance limit. For example, aluminum is a material that does not have a practical endurance limit.

For spacecraft structures the stress levels are generally above the endurance limit hence it is necessary to quantify the fatigue damage accumulated. The most established method for predicting cumulative fatigue damage is the Palmgren-Miner method, also known as Miners rule. With this metho fatigue damage is estimated based on S-N curve data and a predicted loading spectrum which specifies how many loading cycles will be seen between certain stress ranges. The predicted cumulative damage ratio, D, is then given by

$$D = \sum_{i=1}^{m} \frac{n_i}{N_i} \tag{2-9}$$

where n_i is the predicted number of cycles for the i-th load level, N_i is the corresponding number of cycles on the S-N curve, and m is the number of load levels. Failure is predicted if $D \geq 1$.[34] For good design D must be below 1 after safety (scatter) factor is applied.

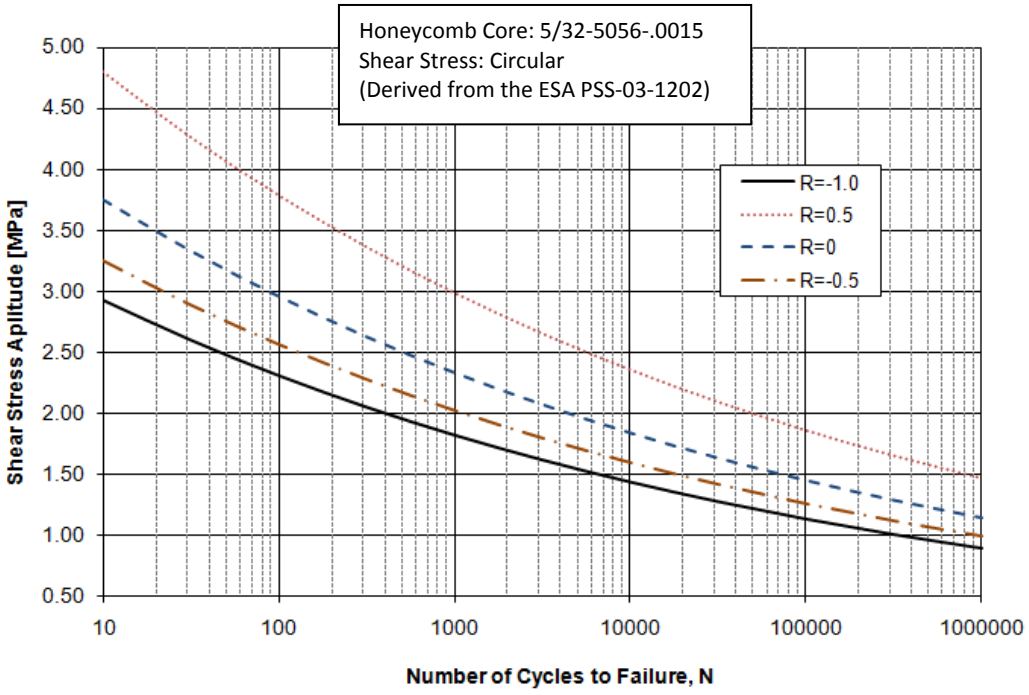

Figure 2-3: Example of fatigue S-N curves (derived from [35])

2.3 Testing of Honeycomb Cores

An extensive test campaign was carried out using the rail shear test method. Several early papers (Norris [36], Reingelstetter et al [37], Werren and Norris [38]) can be identified as having led to today's standardized methods which provide guidelines for the experimental determination of the main mechanical parameters of honeycomb cores. The rail shear test method used here is based on ASTM (American Society for Testing and Materials) standards. The following subsections describe the material specimens and the test procedure used to test them.

2.3.1 Material Specimens

Two types of specimens incorporating two types of aluminum hexagonal cores with designations 5/32-5056-0.0015 and 1/8-5056-0.002 were tested under both static and fatigue loads (see Table 2-1). These cores have densities of 5.3 lb/ft^3 (85 kg/m^3) and 8.1 lb/ft^3 (130 kg/m^3) respectively and cell size of 4 mm and 3.2 mm respectively. For conciseness the two core types will be referred to using their density in lb/ft^3 in the rest of this work. Both cores are produced in a conventional manner by expanding stacks of ribbon foils which were bonded to each other at regular intervals (see Figure 2-4). This process produces cell walls with double thickness along the ribbon direction where the bonds are located. It is usual to refer to the ribbon direction and the expansion directions as the longitudinal (L) and transverse (W) directions respectively (see Figure 2-5). Owing to the double thickness of the ribbon orientated cell walls the honeycomb core has significantly higher stiffness and shear strength in the L direction.

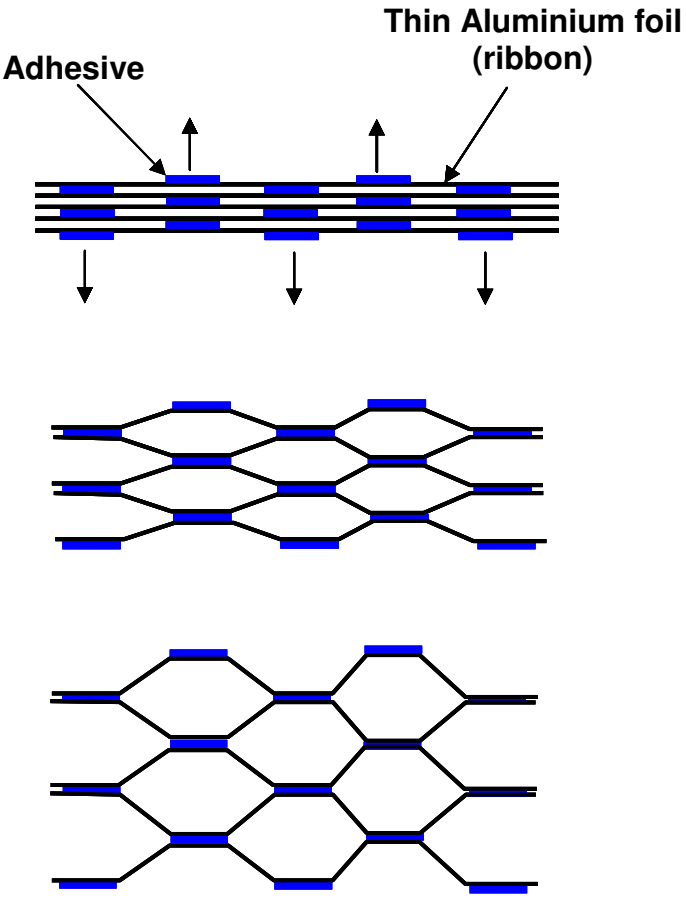

Figure 2-4: Expansion process

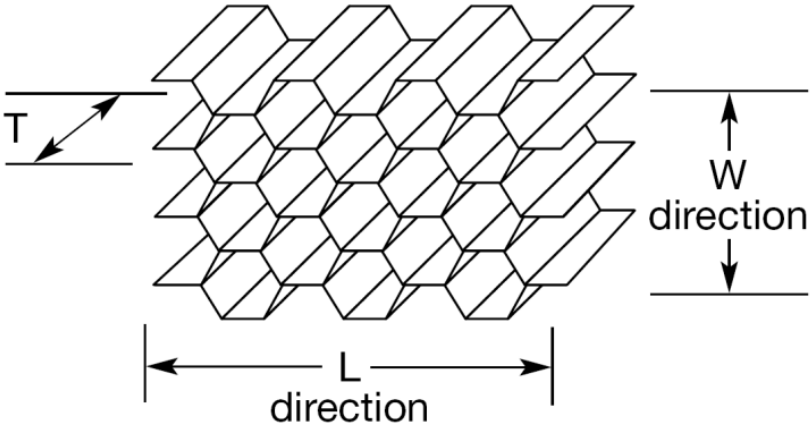

Figure 2-5: Naming conventions of honeycomb core directions

Although the main focus of the investigation is the honeycomb core, the test coupons incorporated the entire sandwich structure which also included the face sheets. This was done to check the overall manufacturing quality and expose any anomalous failure modes – in particular adhesive failures between the core and the face sheets. The face sheets were bonded to the core using Redux 319 adhesive film. For both types of cores the coupons were 15 mm thick and incorporate 0.5 mm thick 2014 aluminium alloy face skins. Both the static and fatigue test coupons were sized in accordance to ASTM standard C273, and were 190 mm in length and 60 mm in width (see Figure 2-6). The coupons were obtained by sectioning large panels to the specified dimensions. By appropriately sectioning the panels, coupons (for both core types) were made for the principal orientations L and W (with the ribbon walls aligned parallel and normal to the longitudinal axis of the coupon respectfully). These are the orientations that are normally looked at when investigating the shear properties of hexagonal honeycomb cores; however, to investigate the variation of core behavior with loading orientation coupons were also made with cell orientations at angles other than 0º or 90º to the longitudinal axis of the coupon. Table 2-2 and Figure 2-7 detail and illustrate the cell orientations that were investigated in the static and fatigue tests that were carried out.

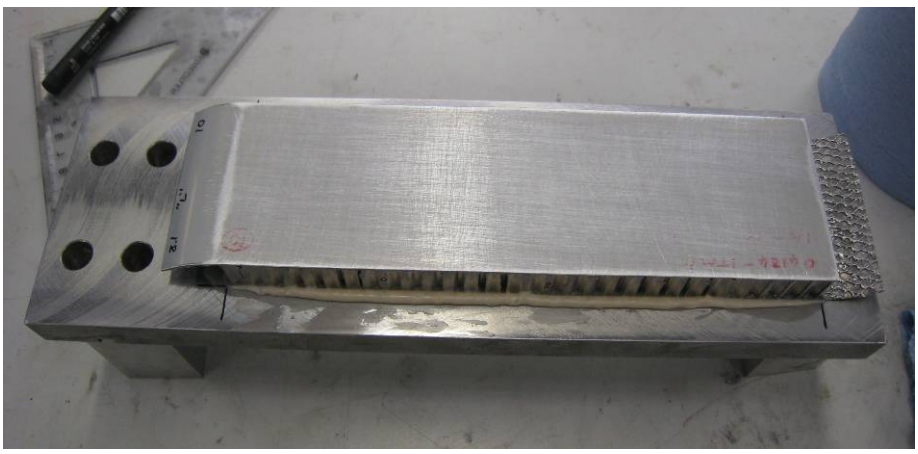

Figure 2-6: Example of one of the test coupons bonded to one of the loading plates

Property	Core Type	
	5/32-5056-0.0015	1/8-5056-0.002
Cell Size [mm]	4.0	3.2
Density [kg/m^3]	85	130
Shear Strength L [MPa]	3.66	6.20
Shear Modulus L [MPa]	586	986
Shear Strength W [MPa]	2.14	3.59
Shear Modulus W [MPa]	228	301

Table 2-1: Quoted properties of tested cores [9]

Core Type	Orientations	
	Static	Fatigue
5/32-5056-0.0015	0º (L), 45º, 90º (W)	0º (L), 45º, 90º (W)
1/8-5056-0.002	0º (L), 22.5º, 45º, 67.5º, 90º (W)	90º (W)

Table 2-2: Tested core orientations

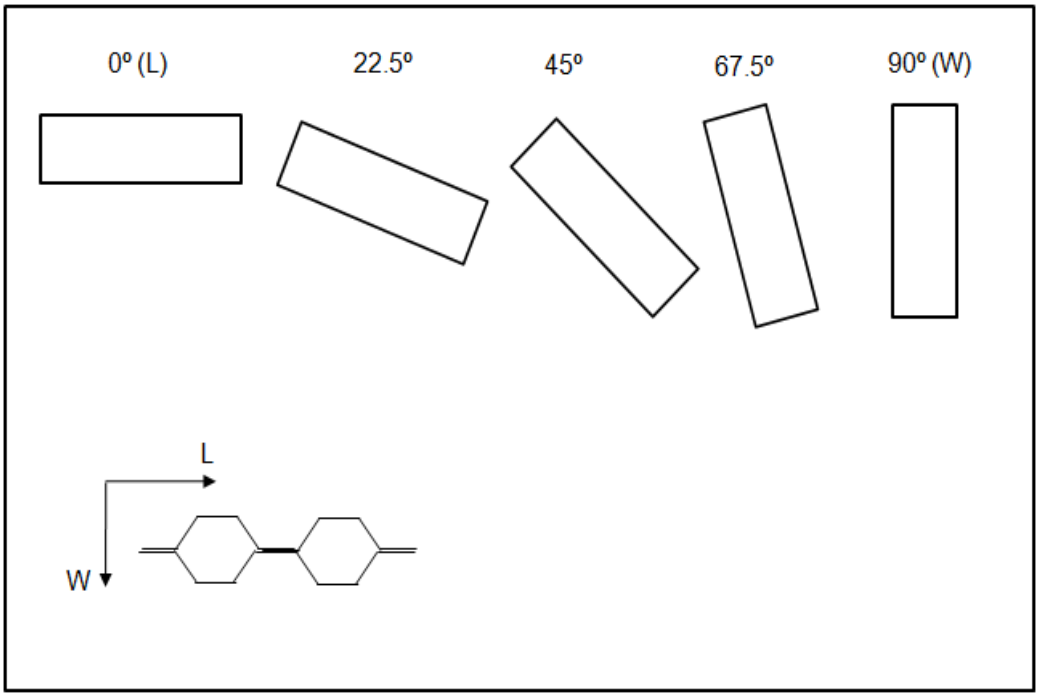

Figure 2-7: Tested core orientations

2.3.2 Experimental Method

Both static and fatigue tests were conducted through the shear test fixture shown in Figure 2-8. The force is transmitted to the coupon through bonded loading plates that are subject to opposing tensile or compressive displacements which result in a shear force on the sandwich core. In order to maintain self alignment and to eliminate bending moments two universal joints are used at both ends of the test fixture. In accordance to ASTM standard C273 the plate length and the distance between the universal joints is such that the line of action of the load passes through the diagonally opposite corners of the sandwich. The test does not produce pure shear stress, but the coupon length is prescribed so that secondary stresses have a minimum effect.

All the tests were conducted on an Instron 8802 universal servo-hydraulic testing machine controlled by an Instron electronic unit. The machine is equipped with a 100 kN load cell and a linear variable differential transformer (LVDT) incorporated in the cross-head to measure the stroke. The load and cross-head displacement signals were recorded through an external PC using a data acquisition system. For the static tests the relative motion between the bonding plates was accurately measured using a strain gauge extensometer (see Figure 2-9).

Figure 2-8: Image of test fixture in operation

Figure 2-9: Strain gage extensometer applied to bonding plates

2.4 Static Test Results

As discussed in section 2.3.1 static tensile tests for 5.3 and 8.1 cored coupons were conducted for various cell orientations. All the tests were carried out at room temperature (~22ºC) in displacement control at a cross-head speed of 0.5 mm/min. Failure load was taken as the peak of the load vs. displacement curves. The corresponding values of shear stress were found using the following expression

$$\tau = \frac{P}{l_c \times w} \tag{2-10}$$

where τ is the shear stress, P is the load applied to the coupon, l_c is the length of the coupon, and w is the width of the coupon. As the relative movement of the bonding plates was directly and accurately measured using an extensometer, from the obtained curve slopes, it was also possible to calculate the shear moduli. This was done using the following expression

$$G = \frac{(\Delta P / \Delta u)c}{l_c \times w} \tag{2-11}$$

where G is the shear modulus, $\Delta P/\Delta u$ is the slope of the load-displacement curve and c is the thickness of the core.

2.4.1 Principal Orientation Tests

Even though the 5.3 and 8.1 cores are standard aerospace grade cores and values for their shear modulus and ultimate strength for the principal L and W orientations can be found in reference manuals or standards (e.g. European Space Agency (ESA) Composite Design Handbook [9]), static testing was carried out in these orientations to see how closely the cores matched the quoted values. The load vs. crosshead displacement curves obtained from the tests are shown in Figure 2-12. As expected, for both core types, the maximum achieved loads are significantly greater for the L oriented coupons than for the W oriented coupons. From the graph it can also be seen that, owing to its higher density, the 8.1 core has significantly

greater shear strength than the 5.3 core. For all the tests reported here failure occurred in the honeycomb cores of the coupons which plastically deformed due to shear buckling of the cell walls (see Figure 2-13). However, when the first attempts were made at testing an initial batch of 8.1 cored L direction coupons it was found that failure occurred prematurely at the adhesive interface between the core and the face sheets (see Figure 2-10 for an example). The problem was investigated by conducting a series of flatwise tensile tests on square coupons obtained from the same 8.1 core panel (see Figure 2-11). These coupons were 75 x 75 mm in size and the tests were carried out in accordance to ASTM standard C297 [39]. From these tests it was found that the film adhesive bond was not strong enough to match the strength of the core. A second panel was subsequently produced using a double layer of adhesive film for each interface. This was found to offer the required adhesive strength and the 8.1 cored coupons which were subsequently produced all had a double layer of adhesive film. The shear test results presented here were only obtained from these coupons.

Looking at Figure 2-12 no significant difference in slope can be seen in the linear regions of the curves indicating that the stiffness of the cores cannot be captured from the crosshead displacement data. This is because at crosshead level the displacement of the large test fixture is also being measured. In order to also obtain stiffness data from the coupons the relative movement between the bonding plates was directly measured using an extensometer. Curves based on extensometer data from these tests are presented in the section 2.4.2 together with curves obtained from testing in other orientations.

Using Equations (2-10) it was possible to obtain the shear stress values corresponding to the load maximums obtained from the tests. From the extensometer data and using Equation (2-11) it was possible to obtain the shear modulus values. The experimentally derived shear strength and shear modulus results are summarized in Table 2-3 where they are also compared with the quoted typical values from the ESA Composite Design Handbook [9]. The shear strength

results are all slightly higher but compare relatively well with the quoted values with the highest difference of the order of just 10% for the 5.3 core in the L orientation. The shear modulus results also compare very well with the quoted values for both the 5.3 and the 8.1 core. Overall then the tests confirm that the cores tested display the mechanical properties expected for their specifications. As the quoted values were obtained using the ASTM standard method, the results also confirm that the test method conforms to ASTM C273 and that fixturing system was working correctly.

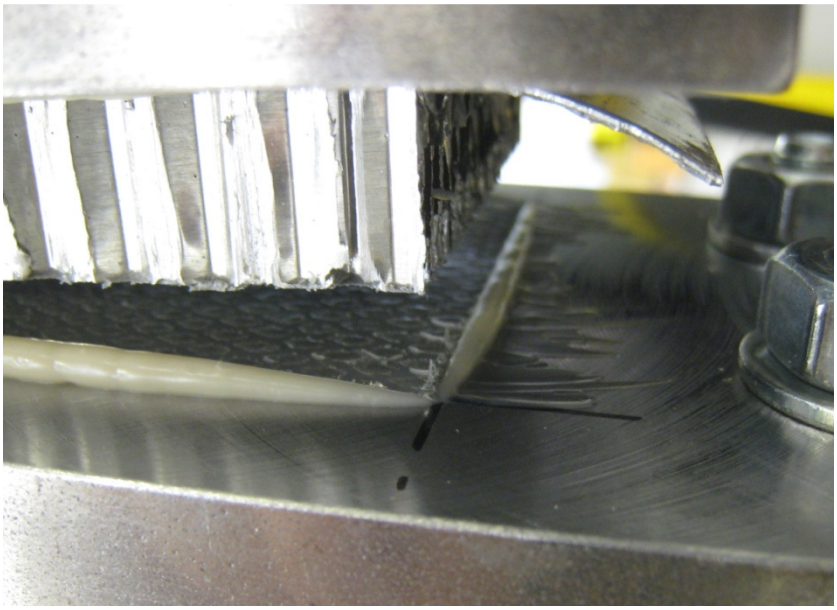

Figure 2-10: Premature core/facing sheet debonding failure for an early 8.1 coupon

Figure 2-11: Flatwise tensile testing of a square 8.1 cored coupon

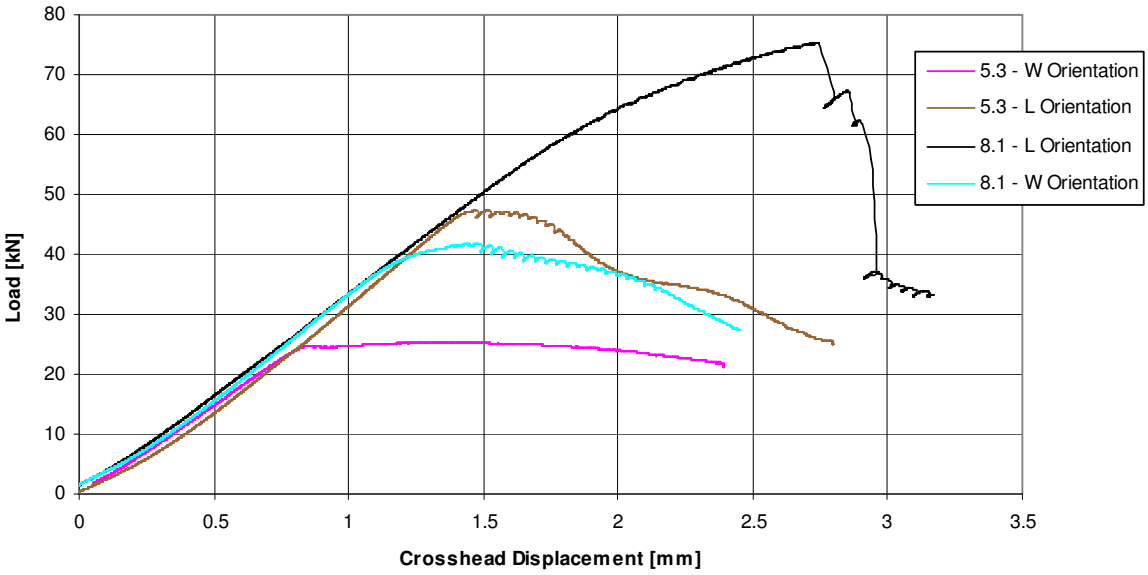

Figure 2-12: Load versus cross-head displacement curves obtained by testing the two core types in the principal orientations

	5.3 Core				8.1 Core			
	Strength [MPa]		Modulus [MPa]		Strength [MPa]		Modulus [MPa]	
	L	W	L	W	L	W	L	W
Experimental Results	4.16	2.18	586.0	228.0	6.61	3.60	1036.6	343.8
Quoted Typical Values	3.65	2.14	576.5	245.2	6.21	3.59	986.0	352.0

Table 2-3: Result obtained by testing in the principal orientations and comparison with quoted values from [9]

(a) L Orientation

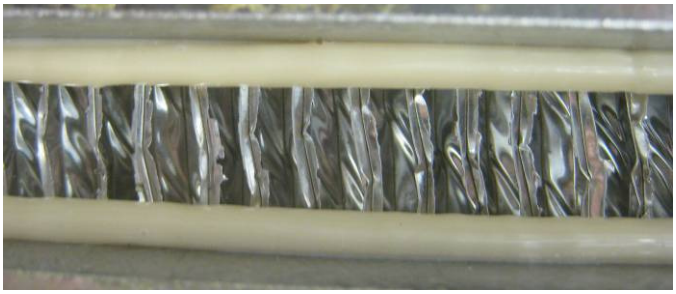

(b) W Orientation

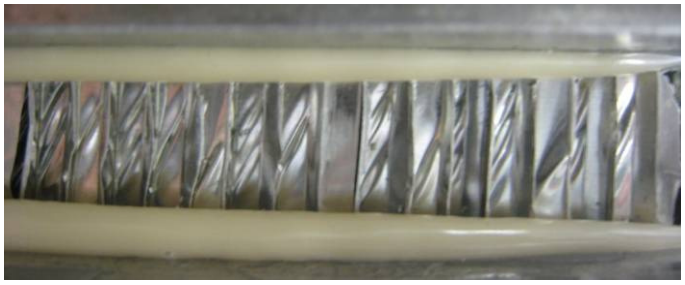

(c) 45 Orientation

Figure 2-13: Failure mode of core in L, W and 45 orientations

2.4.2 Angled Orientation Tests

From Table 2-3 it can be seen that for both core types the variation in mechanical shear properties from the L orientation to the W orientation is significant. To investigate how these properties transition from the L orientation to the W orientation a series of tests were conducted on coupons with cells oriented at various angles to the longitudinal axis of the coupon (see Table 2-2). The orientations tested were limited by the number of coupons that could be obtained from the available panel specimens. For the 5.3 core, three 45 deg orientation coupons were tested in addition to the principal orientations. The averaged results are summarized in Table 2-4 and Figure 2-14 shows a typical load vs extensometer displacement curves for the 45 deg orientation plotted with the principal orientations. From the graph it can be seen that using the extensometer measurement it is possible to capture the stiffness variation between the different core orientations. For the 45 deg orientation it would be reasonable to expect a structural behavior somewhere between the L orientation and the W orientation, but from this graph it can be clearly seen that, although the stiffness of the core increases, its strength does not when going from the W orientation to the 45 deg orientation; on the contrary it decreases slightly (this is also confirmed from the results obtained from the fatigue tests presented in Section 5).

As can be seen from Table 2-2 for the 8.1 core more orientations were tested. The averaged results from these tests are summarized in Table 2-5 and typical load vs extensometer displacement curves obtained for these tests are shown in Figure 2-15. For the L orientation test the extensometer was only used for the initial part of the test to obtain the shear modulus of the core and was then removed to prevent the possibility of damaging the extensometer as a result of coupon/loading panel debonding (hence why the curve shown for this test is truncated). This could have happened since in the L orientation the shear strength of the 8.1 core is close to the maximum strength that can be achieved from the adhesive used to bond the coupons to the loading plates. However, for this test no adhesive failure occurred

and the coupon failed in the core as intended (the full load vs crosshead displacement curve can be seen in Figure 2-12). From Figure 2-15 it can be seen that, as for the 5.3 core, while the shear modulus increases slightly the shear strength does not when going from the W orientation to the 45 deg orientation. On the contrary there is a slight decrease in shear strength and looking at the 67.5 deg orientation there is even a greater decrease. This can be clearly seen in Figure 2-16 where the maximum shear strength results obtained from the tests are plotted against cell orientation. From this graph it can be seen that for both core types the shear strength only increases significantly when the loading orientation decreases below 45 deg, below which as loading orientation decreases the strength increase rate grows until the maximum strength is reached at 0 deg (i.e. the L orientation). A similar behavior can be seen in Figure 2-17 for the shear modulus variation with loading orientation.

Direction	Modulus [MPa]		Shear Strength [MPa]		Coupons Tested
	Average Value	Standard Deviation	Average Value	Standard Deviation	
0º (L)	576.49	N/A	4.16	N/A	1
45º	305.84	14.34	2.12	0.05	3
90º (W)	245.15	N/A	2.18	N/A	1

Table 2-4: Summary of 5.3 core results

Direction	Modulus [MPa]		Shear Strength [MPa]		Coupons Tested
	Average Value	Standard Deviation	Average Value	Standard Deviation	
0º (L)	1036.00	N/A	6.61	N/A	1
22.5 º	661.43	24.97	4.32	0.09	3
45º	389.07	16.62	3.67	0.10	3
67.5 º	319.29	16.34	3.29	0.09	3
90º (W)	343.76	N/A	3.60	N/A	1

Table 2-5: Summary of 8.1 core results

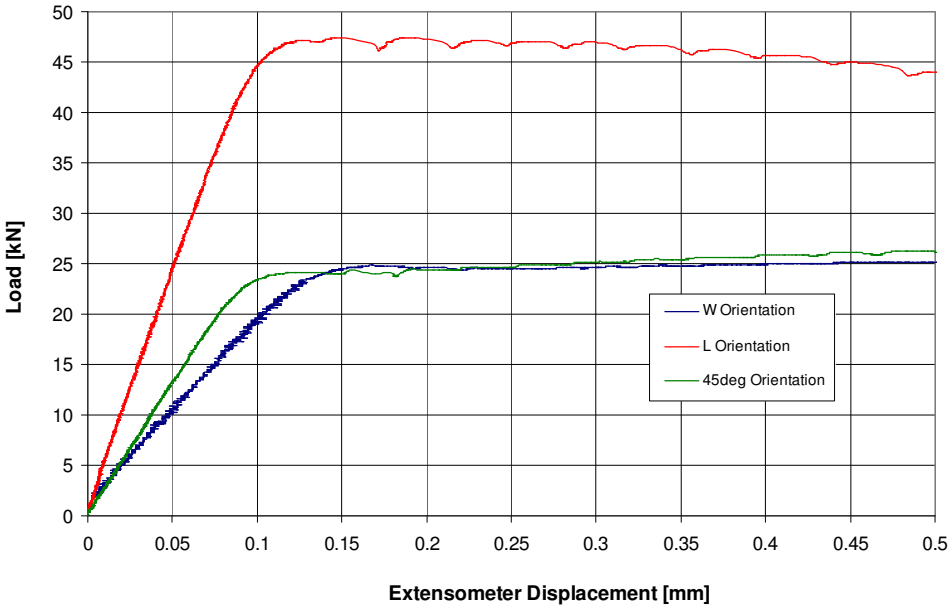

Figure 2-14: Typical load vs extensometer displacement curves obtained for the 5.3 core

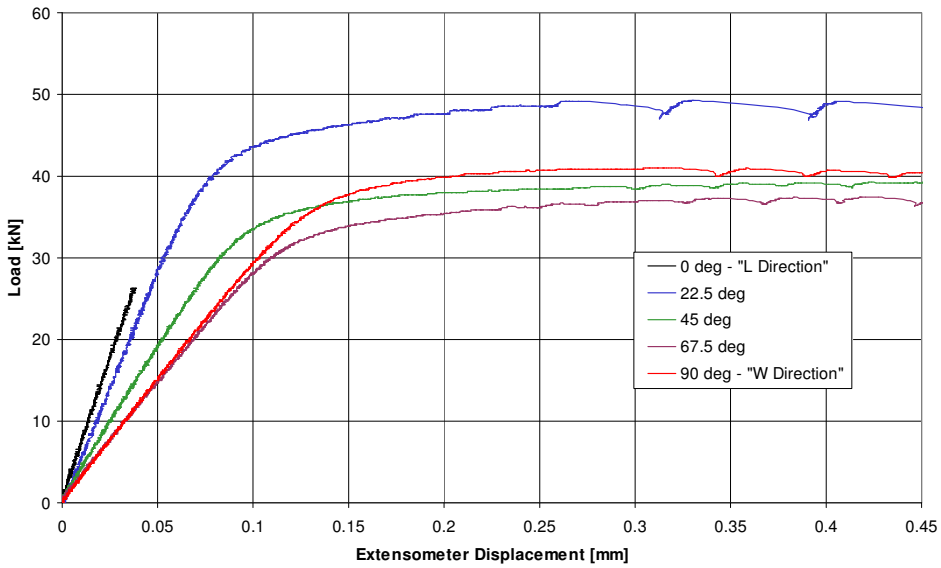

Figure 2-15: Typical load vs extensometer displacement curves obtained for the 8.1 core

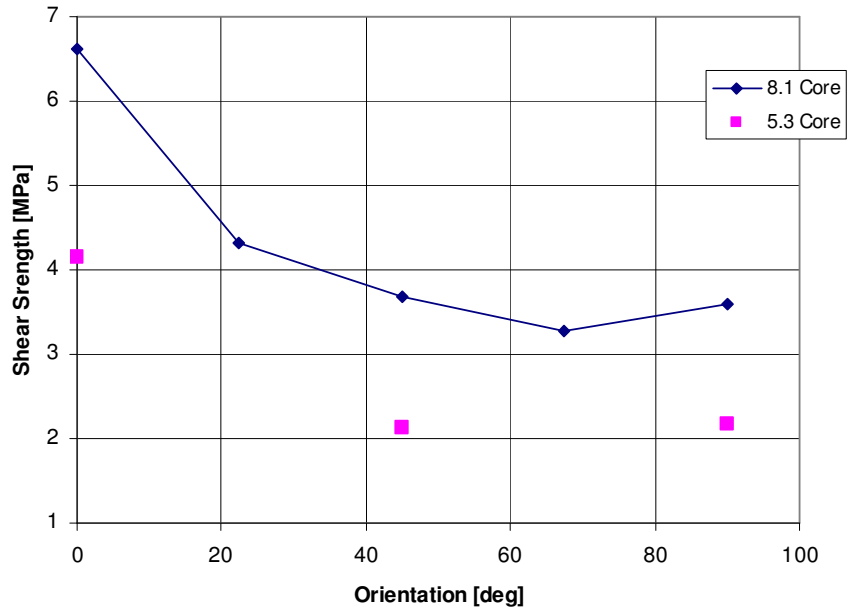

Figure 2-16: Variation of measured shear strength with cell orientation for the 8.1 core

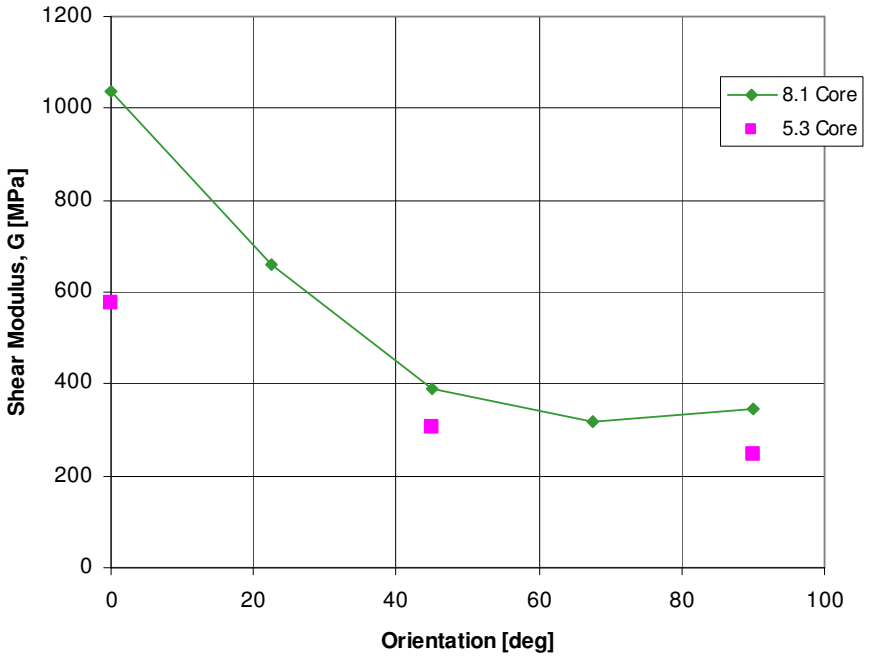

Figure 2-17: Variation of measured shear modulus with cell orientation for the 8.1 core

2.5 Fatigue Test Results

The objective of the fatigue tests was to obtain basic knowledge of the fatigue behavior of the tested honeycomb cores by producing S-N diagrams and observing the failure modes. For the 5.3 core tests were conducted for the L, W and 45° orientations. For the 8.1 core, tests were carried out only for the W orientation. Tests for the L orientation were not carried out since it was not possible to guarantee a strong enough bond between the specimen and the loading plates (due to the high strength of the specimen itself in this orientation). All tests were conducted at room temperature in load control at load amplitude values chosen on the basis of the static test results. For all the tests the applied load was sinusoidal with a ratio R = -1 (i.e. fully reversed). The fully reversed load profile subjects the coupon to alternating tensile and compressive stresses and was chosen because it induces the highest fatigue damage and hence is representative of the most severe loading scenarios. The fatigue life of the coupons is characterized in terms of the number of cycles to ultimate failure. For all the tested coupons failure was in the core and no core/face sheet debonding occurred.

The S-N fatigue curves obtained for the 5.3 core in both the L and the W orientations are both shown in Figure 2-18. As expected the lifetime of the core is significantly longer in the L configuration than in the W configuration for equivalent values of stress amplitude. However, from the trendlines, it is possible to see that as stress amplitude reduces the lifetime increases slightly more rapidly for the W orientation. Plotting these fatigue curves in terms of normalized load level (expressed as percentage of static ultimate load) versus displacement (see Figure 2-19) it is possible to see that, for load levels above ~20%, the achieved lifetime for the W configuration is actually higher than for the L configuration. This indicates that even though the core is significantly stronger in the L direction it seems to be (in relative terms) more effective at resisting fatigue damage in W direction.

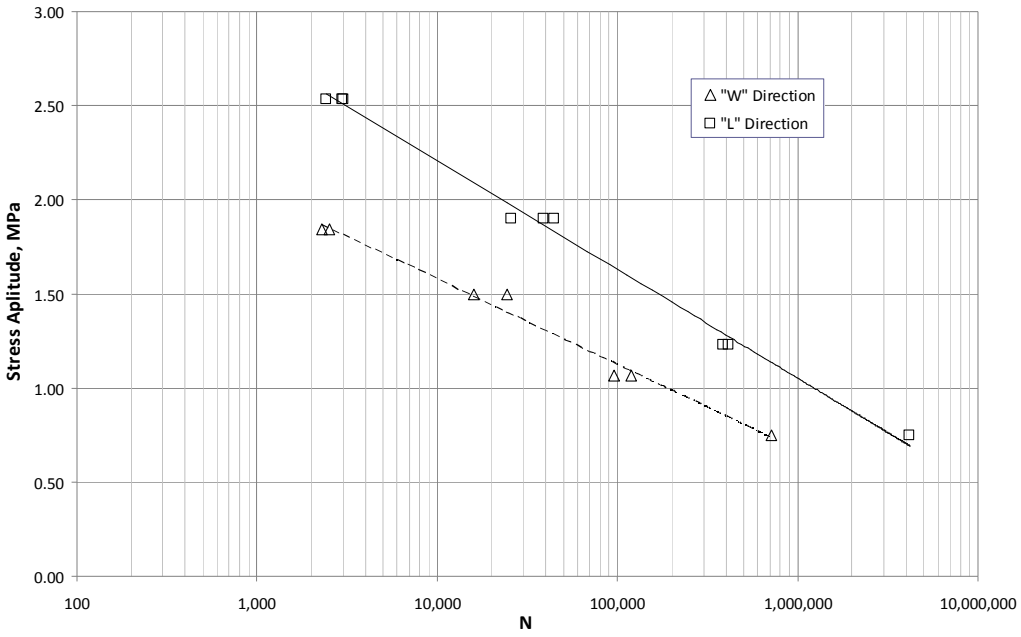

Figure 2-18: S-N curve for tested 5.3 cored coupons in L and W directions

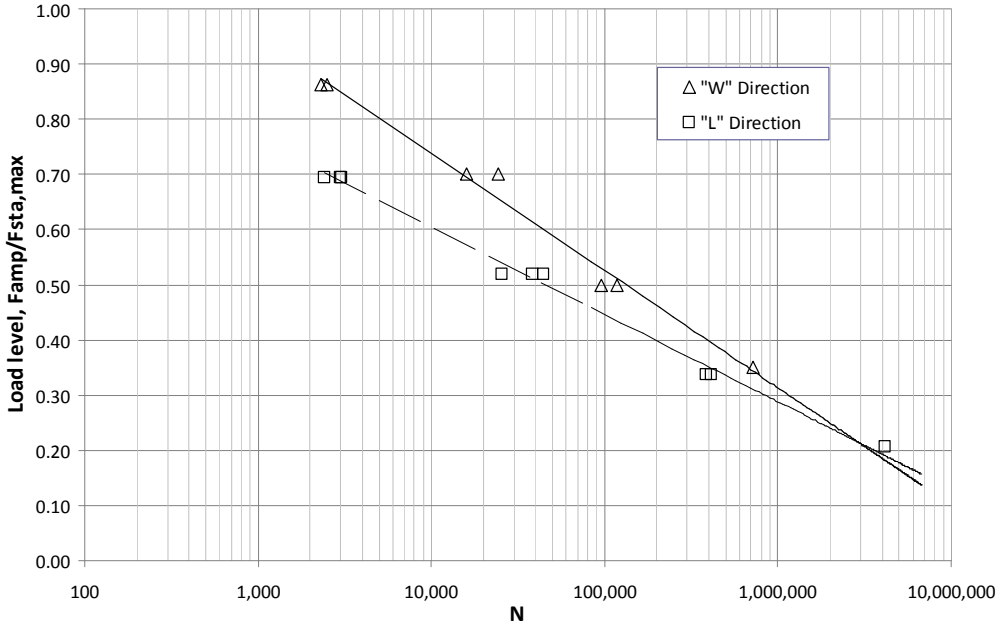

Figure 2-19: Load level versus cycle no. curves for tested 5.3 cored coupons in L and W directions

From visual inspection of the free sides of the failed coupons a difference was noticed in the failure modes experienced at different load levels. At high load levels both coupon types fail in a very similar way to the coupons that were subjected to the static tests, with the core plastically deforming as the cell walls buckle under shear, but no visible cracks appearing. For lower load levels the development of cracks was observed during the lifetime of both the L and W configuration samples (see Figure 2-20 and Figure 2-21). However, it was also noticed that crack development is different for the two cell orientations.

For the L configuration cracks appear to initiate at the face sheets and propagate diagonally towards the centre as the test progresses (see Figure 2-20), while for the W orientation cracks initiate on the inclined single thickness cell walls at cell wall boundaries and develop diagonally to the next boundary (see Figure 2-21). For equivalent load levels the cracks develop to a significantly greater length in the L orientation than in the W orientation. This is because in the W orientation the cell wall boundaries also act as crack boundaries since each diagonal cell wall is connected to one half of a double cell wall which is aligned at 90º to the loading axis (see Figure 2-22 (a)). On the contrary in the L orientation none of the cell walls are at 90º with the loading axis and consequently all the cell walls are subject to shear stresses and cracks are allowed to grow along each ribbon from cell wall to cell wall (see Figure 2-22 (b)). These differences in crack propagation are likely to have a significant effect on the fatigue life of the specimens and offer a good explanation as to why the core is more effective at resisting fatigue damage in the W direction; particularly for lower stress amplitudes (i.e. high cycle fatigue) where cracks have to reach a large critical length before failure occurs.

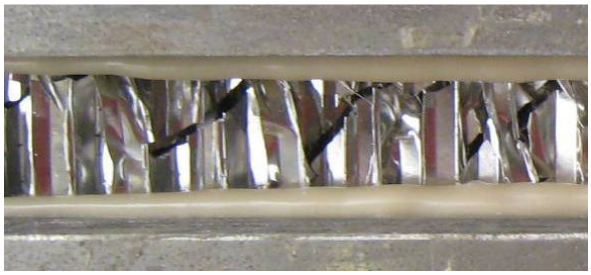

Figure 2-20: Crack development in core after fatigue testing in L direction at 34% of the static ultimate load ~400000 cycles

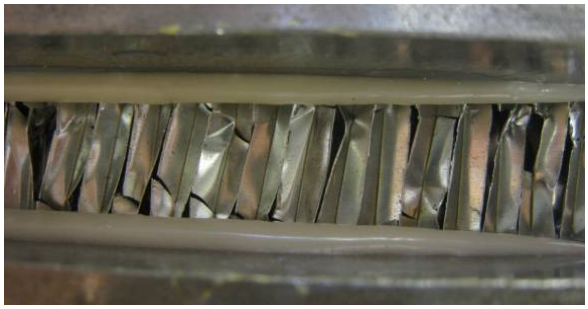

Figure 2-21: Crack development in core after fatigue testing in W direction at 35% of the static ultimate load ~718394 cycles

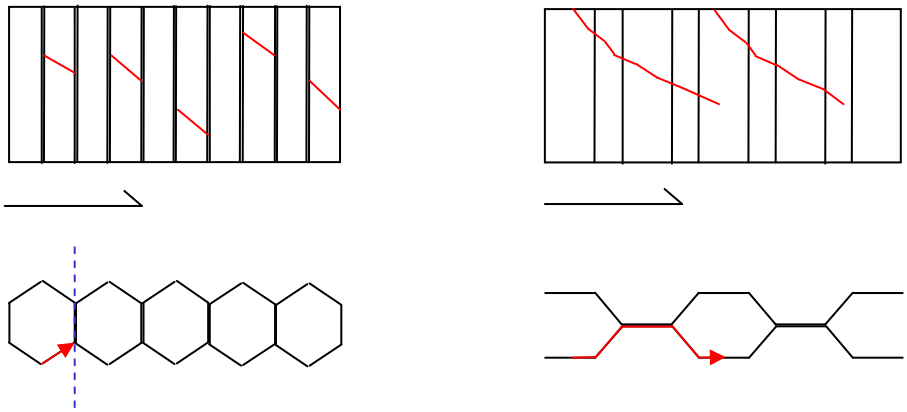

(a) W Direction **(b)** L Direction

Figure 2-22: Differences in crack development for the L and W directions

For the 5.3 core, fatigue tests were also carried out for the 45deg orientation. The S-N curve obtained from these tests is shown in Figure 2-23 where it is also compared with the curves obtained for the L and W orientations. From the S-N diagram it can be clearly seen that the lifetime of the coupon is slightly lower in the

45 deg orientation compared to the W orientation for equivalent load levels. This is in agreement with the slightly lower static strength that was obtained from static testing.

Figure 2-24 shows the fatigue curve obtained for the 8.1 core in the W orientation compared with the one obtained for the 5.3 core in the W direction. From the graph it can be seen that the lifetime of the 8.1 core is significantly higher owing to its higher static strength.

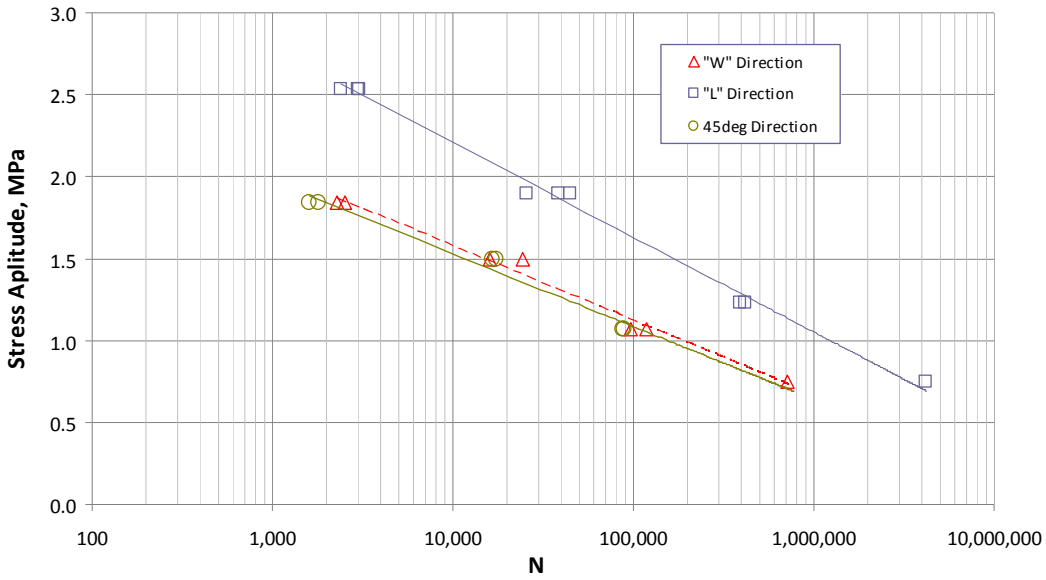

Figure 2-23: Load S-N curve for tested 5.3 cored coupons in L, W and 45deg directions

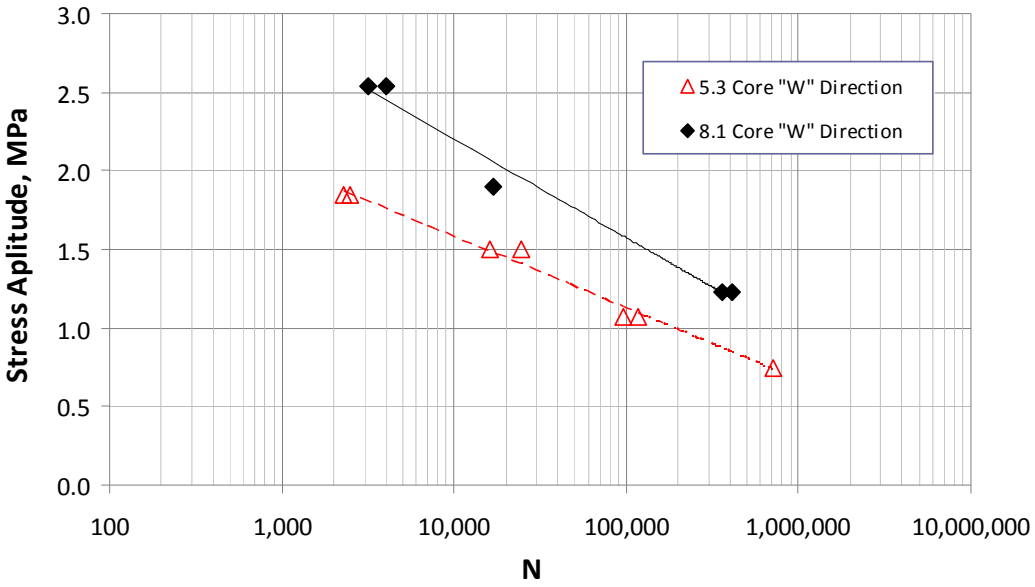

Figure 2-24: Load level versus cycle no. curves for tested 8.1and 5.3 cores in the W directions

The displacement amplitude of the crosshead was also recorded during the fatigue tests to see how the stiffness varied during the lifetime of the specimens. From this data it was found that there is very little variation in displacement amplitude and consequently of the sample stiffness during most of the fatigue lifetime. Any significant changes in displacement amplitude were very quickly followed by coupon failure. This suggests that stiffness is probably not an effective monitoring measure for the health of honeycomb cores subject to shear loads.

2.6 Conclusions

Static and fatigue shear block tests were carried out on both 5.3 and 8.1 cored coupons in various orientations. For the static tests conducted in the principal orientations the results were found to be in agreement with the typical quoted values of both core types. On the first attempts that were made at testing the 8.1 core in the L direction it was observed that failure occurred prematurely by deboning of the core/face sheet adhesive interfaces. This was further investigated by conducting flatwise tensile tests and the problem was solved by using double

layers of film adhesive of subsequently produced coupons. This highlights the importance of ensuring that the adhesive bond between the face sheets and the core is strong enough to match the strength of the selected core. If this cannot be achieved it is not possible to gain any benefit from selecting a higher density core and the end result is only to add more unnecessary mass to the structure.

Data relevant to tests carried out at angles other than the principal orientations is not available in reference manuals and no studies are reported in the literature. From the tests carried out here it was found that for both core types the shear strength and the shear modulus had a non-linear relationship with loading orientation. Contrary to what is normally assumed, it was also found that (albeit by a small margin) the W orientation was not the weakest orientation. For both core types it was found that the shear strength only increases significantly when the loading orientation is decreased below 45deg below which the increase rate grows until the maximum strength is reached at 0 deg (i.e. the L orientation).

As will be covered in the next chapter, using the finite element method it was determined that this non-linear relationship is due to the tendency of the core to also displace cross-axis with respect to the loading orientation when the load is not applied parallel to one of the principal orientations.

As expected, from the fatigue tests it was found that for equivalent stress amplitudes, the fatigue lifetime of the specimens was longer in the L direction compared to the W direction. This is because the core has a significantly higher static ultimate strength in the L direction; however, in terms of load level (i.e. percentage of static ultimate strength) versus lifetime it was found that the core is actually more effective at resisting fatigue damage in the W orientation. By visual inspection of the failed specimens it was found that this may be attributed to the fact that crack propagation appears to be significantly inhibited by cell wall boundaries in the W orientation. However, it should be emphasized, that this does not mean that the W direction is optimum for fatigue since in absolute terms fatigue life is significantly longer in the L direction. For the 5.3 core fatigue tests

were also conducted for the 45deg orientation. From the S-N curve obtained from these tests it was observed that the lifetime of the coupon in this orientation was slightly lower compared to the W orientation.

Chapter 3

3 FE Modeling of Honeycomb Core

3.1 Introduction

To further study the effect of loading orientation on the shear strength of honeycomb cores and to better understand the experimental results presented in Chapter 2 an investigation using the finite element method was also carried out. FEM has been used to study honeycomb cores since the end of the 1980s. The early studies were carried out to find the elastic parameters of honeycomb cores. Apart from Grediac's work [24] mentioned in Chapter 2 there are several other authors who have used FEM to study the elastic behavior of sandwich cores. In Guo and Gibson [40] a two-dimensional beam finite element approach is used to adjust Gibson's and Ashby's [19] in plane Young's moduli E_x and E_y. In Chamis et al [41] a three-dimensional finite element model is used to adjust the analytical equations based on a mechanics of material concept. A similar study has been conducted more recently by Allegri et al [42] on carbon honeycomb.

Over the last decade with advances in computational power it has become possible to model, not only the elastic behavior prior to cell wall buckling but also the cell wall folding mechanisms in the post-damage region. Based on these advances many efforts have been made to develop virtual testing techniques to assess novel core geometries without the requirement for expensive experimental test campaigns. Many of these simulation techniques are based on explicit nonlinear finite element analysis and focus on predicting the crush behavior of honeycomb cores subjected to out-of-plane compression. Aminanda et al [43] used the commercial FE code RADIOSS, Aktay et al [44] used PAM-CRASH, and Gotoh et al [45]used LS-DYNA to simulate the out-of-plane crush behavior of aluminum and Nomex® honeycomb cores. For all of these works ideal, uniform hexagonal core geometries without any imperfections were modeled. However, in reality all cellular structures are characterized by geometrical imperfections arising from the

manufacturing process, which have a strong influence on their final strength. An ideal model always over predicts buckling strength leading to poor non-conservative engineering predictions. Hohe and Becker [17] is one of the first works to address this problem which is covered in more detail in section 3.4. Several works have looked at the influence of imperfections on the mechanical behavior of honeycomb cores under in-plane loads: Li et al [46] considered the effect of irregular cell wall thickness and irregular cell geometry, Yang et al [47] considered the effect of irregular cell wall thickness and uneven cell walls, Yang and Huang [48] considered the effect of imperfections in cell wall junctions, and Simone and Gibson [49] considered the influence of cell wall curvature.

The influence of manufacturing imperfections on the out-of-plane compressive behavior of honeycomb cores has also been investigated in the literature. Xue and Hutchinson [50] used mode shading to model cell imperfections using ABAQUS noticing a strong influence on the resulting stress-strain curves. In Heimbs [26] imperfections are accounted for using node shading and cell wall property reduction (cell wall thickness and material data) to model the crush behavior of hexagonal Nomex® honeycomb, and Kevlar® and carbon fold cores.

Few works have looked at the influence of imperfections on the in-plane shear behavior of modeled cellular cores. In Heimbs [51] this is also covered and a significant effort was made to model the post-buckling cell wall folding behavior of the core. In this work the deformation of fold cores was modeled up to as much as 40% of shear strain.

In the present research the main focus was not to carry out “virtual tests” but rather to predict the buckling and corresponding peak in the stress-strain curve to further investigate the effect of loading orientation on the strength of honeycomb cores. Imperfection modeling was used as a tool to obtain more realistic results which correlated with the available test results.

3.2 Finite Element Modeling Tools

Modeling of honeycomb core failure mechanisms cannot be achieved using conventional linear finite element analysis. The following subsections briefly describe the nonlinear analysis techniques used for the analyses described in this section.

3.2.1 Nonlinear Analysis

Linear finite element analysis implies a linear relationship between the load applied to a structure and its response. The stiffness matrix remains the same in linear analysis and a solution is arrived at in one single step, by a single decomposition of the stiffness matrix. Linear analysis is quick and computationally inexpensive however it has inherent limitations. It cannot be used to model large deformations and material yield. Furthermore the loads are assumed to be applied slowly in order to maintain the structure in equilibrium.

The analysis of honeycomb core shear failure mechanisms requires the use of nonlinear finite element techniques. The early development of nonlinear analysis was mainly pushed forward by the nuclear and aerospace industries [52]. In the nuclear industry nonlinearities need to be accounted for mainly due to the requirement of having to model the high temperature behavior of materials. In the aerospace industry nonlinearities are mainly due to large deformations and buckling. These are the nonlinearities that need to be considered when modeling honeycomb cores.

In a nonlinear problem the stiffness matrix changes with deformations and the response is no longer linearly related to the applied loads. To solve such a problem it is necessary to divide the analysis in steps, calculating the displacements and then re-evaluating the stiffness matrix in an iterative process where the results from each step are used as the starting point for the next step. Therefore the stiffness matrix needs to be generated and decomposed several times adding time and computational cost to the analysis. Nonlinear analysis offers many strategies which

can be used to divide the loading into logical steps, and achieving equilibrium at the end of each step. The best strategy to use depends on the structure, the type of loading and the nonlinear effect which needs to be modeled.

3.2.2 Newton-Raphson Iteration Method

In nonlinear analysis there are various iteration techniques available to solve the equilibrium problem at each load increment. The most established of these is the Newton-Raphson method which was used for all the analyses carried out in this work. This method is based on the following equation

$$\boldsymbol{K(u)\delta u = F - R(u)} \tag{3-1}$$

where K is the tangent-stiffness matrix, u is the nodal displacement vector, R is the internal nodal-load vector (resulting from the internal stresses),and F is the external nodal load vector.

Convergence is obtained by an iterative process which, for a one-dimensional problem, is depicted in Figure 3-1. The Newton-Raphson method can be either be applied in load control or displacement control. In this work the method was always applied in displacement control in order to achieve convergence in the post-buckling region.

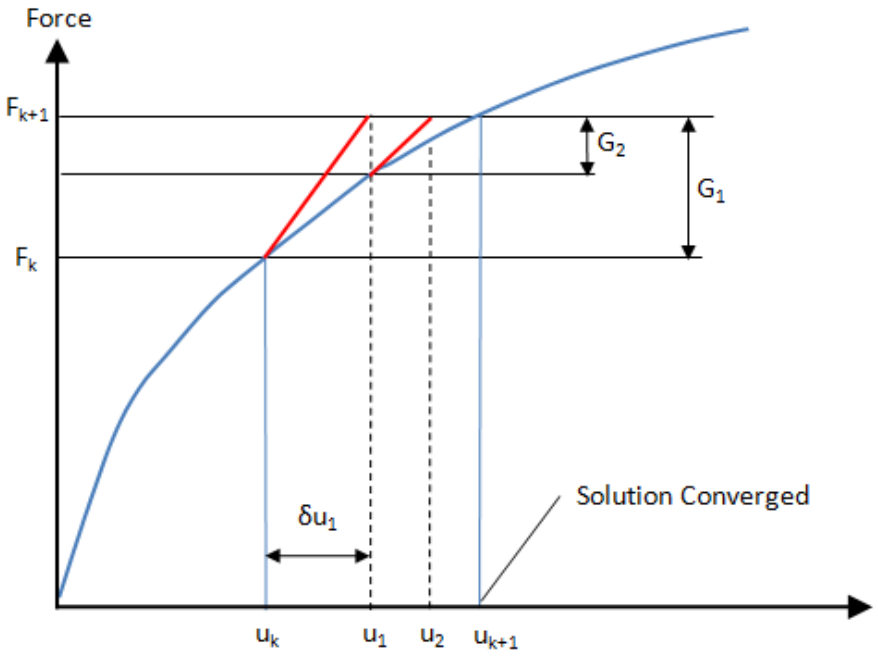

Figure 3-1: Newton-Raphson method

3.2.3 Arc-Length Method

For many post-buckling problems the Newton-Raphson method is not a suitable iteration technique. A typical example of this is *snap-through* buckling of a simply supported arching beam as illustrated in Figure 3-2. The post-buckling behavior of such a system is characterized by an instability region where the stiffness tangent is negative (see Figure 3-3). In a load controlled problem the Newton-Raphson method works by incrementing the load by a finite amount at each sub-step keeping the load fixed during the equilibrium iterations, and because of this it cannot converge if the tangent stiffness is negative. The same problem is applicable for a displacement controlled problem since the solution will tend to jump from positions 3 to 5 in Figure 3-3. The most established way of solving these types of problems is the arc-length method. With the arc-length method the time step is associated with a load-displacement arc rather than a fixed load or displacement (see Figure 3-4). The system allows for the load and the displacement to vary throughout the time step and can cope with negative stiffness tangents.

Although the failure process of honeycomb cores under in-plane loads is characterized by shear buckling of the cell walls there is no snap-through behavior (as can be seen in the experimental results presented in Chapter 2) and the problem can be handled using the Newton-Raphson method in displacement control.

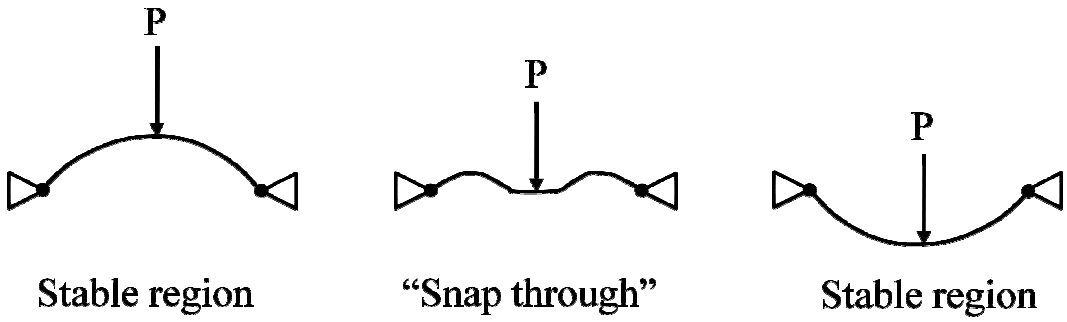

Figure 3-2: Snap-though buckling of a simply supported arch

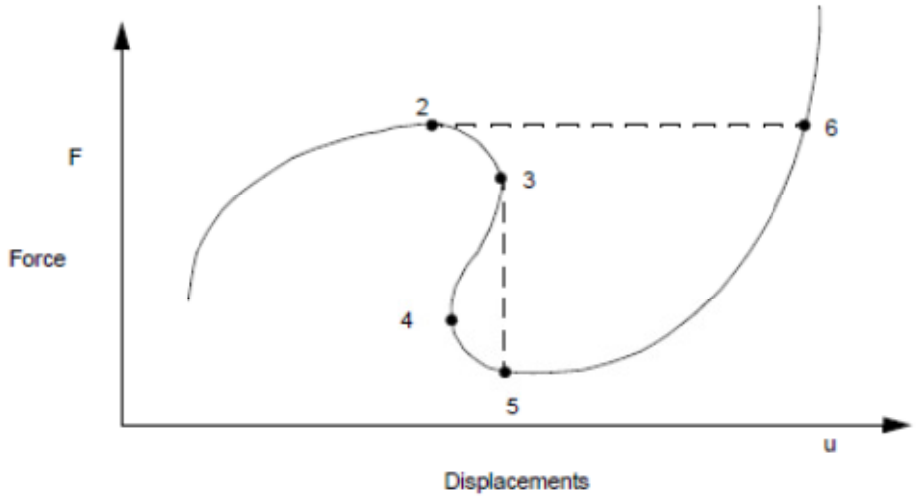

Figure 3-3: Snap-through behavior [52]

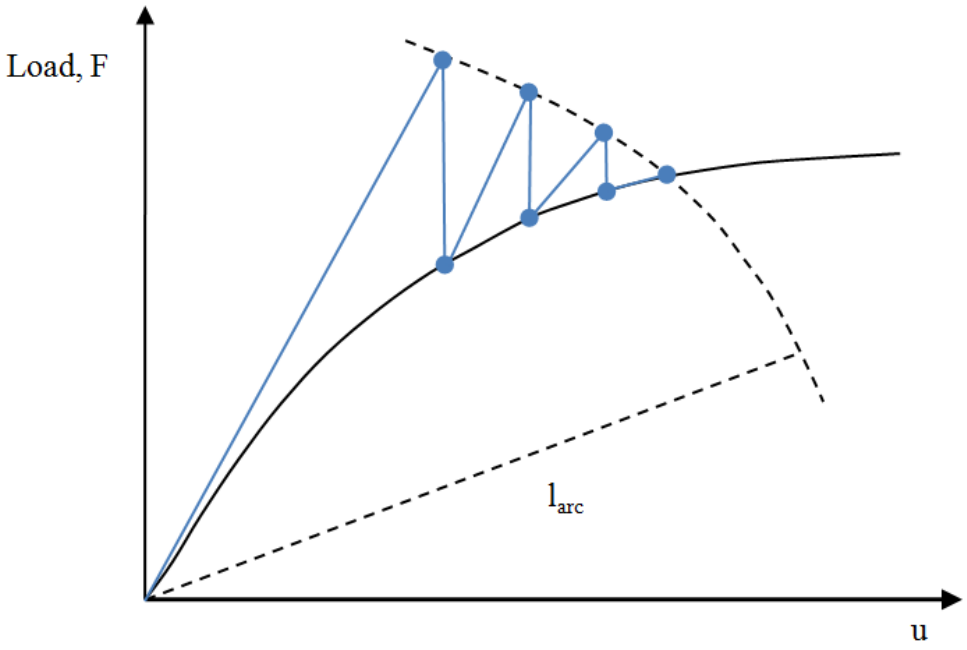

Figure 3-4: Arc-length method convergence behavior

3.3 Model Description

In order to reduce the requirement on computational resources instead of modeling the whole coupon, the approach taken here was just to consider a representative cell and apply appropriate boundary conditions. To simulate the buckling failure mechanism of the cell walls Nastran's Implicit Nonlinear solution (SOL 600) code was used to process the model. The cell models were meshed using 4-node quadrilateral shell elements and constructed based on the geometrical dimensions of the 8.1 and 5.3 core cells.

Various boundary conditions were investigated and the solution described in what follows was found to give the most realistic results. The cell model is constrained at the base in the x, y and z global coordinate directions and loaded by applying a fixed displacement at the top in the desired direction. The loading displacement is applied to a single node rigidly connected to the top edges of the cell walls via a multi point constraint (MPC). To avoid bending moments the cell is also constrained in the z global coordinate direction along its outer edges (see Figure

3-5). To ensure in-plane loading and to avoid twisting all rotations are constrained for the loading node at the centre of the MPC. To obtain a displacement perfectly aligned with the specified displacement direction a constraint should be applied normal to it (a cross-axis constraint). If a cross-axis constraint is not applied the cell is allowed to drift sideways with respect to the displacement direction. When the displacement is applied in the principal orientations there is no significant tendency for the sideways drift. However, due to structural imbalance, this is not the case for the in between orientations for which the application of a cross-axis constraint has a significant effect on the obtained shear modulus and shear strength. In reality, in most cases, what happens is somewhere between having a fixed cross-axis constraint and fully free cross-axis displacements. This "in-between" condition can be simulated by using a spring element aligned to the cross-axis direction. In a real application the stiffness of the spring would depend on how the honeycomb panel is constrained and connected to its surrounding structural components. For the experimental case considered here the loading fixture has a tendency to maintain its original alignment and resists cross-axis displacements to a certain extent.

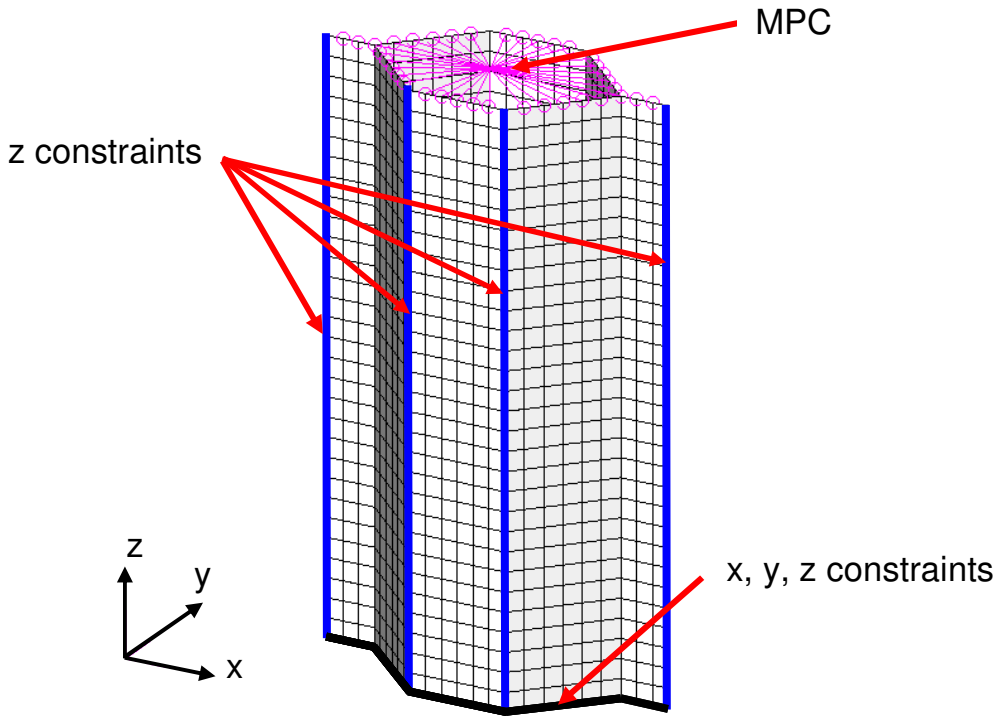

Figure 3-5: Unit cell model with global coordinate system and boundary conditions

3.4 Modeling of Imperfections

Buckling instability is a notoriously challenging phenomenon to model using the finite element method and generally yields non-conservative over-estimations of the mechanical properties. The main reason for this is that normally the inherent imperfections of a real structure are not modeled. These imperfections are particularly pronounced for the cellular structures considered here. The expansion process can only be controlled to a certain extent and a perfect hexagonal geometry is not achievable. Likely imperfections include [17]: uneven cell walls, irregular cell geometry, cell wall intersections with rounded rather than perfect angular corners, and non constant wall thickness. For certain buckling problems it is necessary to introduce imperfections or disturbances to trigger the failure mode in the first place. A typical example of such a problem is a straight column under compression loading. If the column is modeled perfectly straight and the load is

perfectly aligned a nonlinear analysis will not predict buckling failure. This is not the case when modeling a honeycomb core under in-plane loads since the load is never aligned with all the cell walls. Hence here the imperfections were just needed to lower the buckling failure predictions to more realistic levels. There are several ways to account for the effect of such imperfections in a finite element model.

One method is to introduce imperfections in the mesh. An effective way of doing this is via "mode shading", whereby the nodes' coordinates are modified based on the eigenvalues obtained by running an eigenvalue buckling analysis (Figure 3-6). The degree of imperfection can be scaled as a percentage of nominal wall thickness (typically between 5 and 30%).

Another way of accounting for imperfections is to vary the thickness properties of the shells across the mesh (whilst keeping the overall average equal to the nominal thickness). An example of this can be seen in Figure 3-7 where random thickness variation was applied to the cell walls. A further alternative is to reduce the overall cell properties (material properties and wall thickness) for the whole model. This is also justifiable since in reality the weakest or thinnest regions of the core are going to drive the failure strength of the core [51].

In order to appropriately account for imperfections the best approach is to apply more than one of the above techniques in conjunction. Here mode shading and thickness variation were used to obtain more realistic results. The magnitudes of the imperfections were applied based on manufacturing tolerance estimates and then adjusted to reduce the over-estimation in predicted failure load compared with the experimental data. However, a perfect correlation was not sought since the main aim of the study was to investigate the effect of loading orientation and see if the same trends observed from the experiments would be obtained. For each cell model the same imperfection parameters were used for all the load cases.

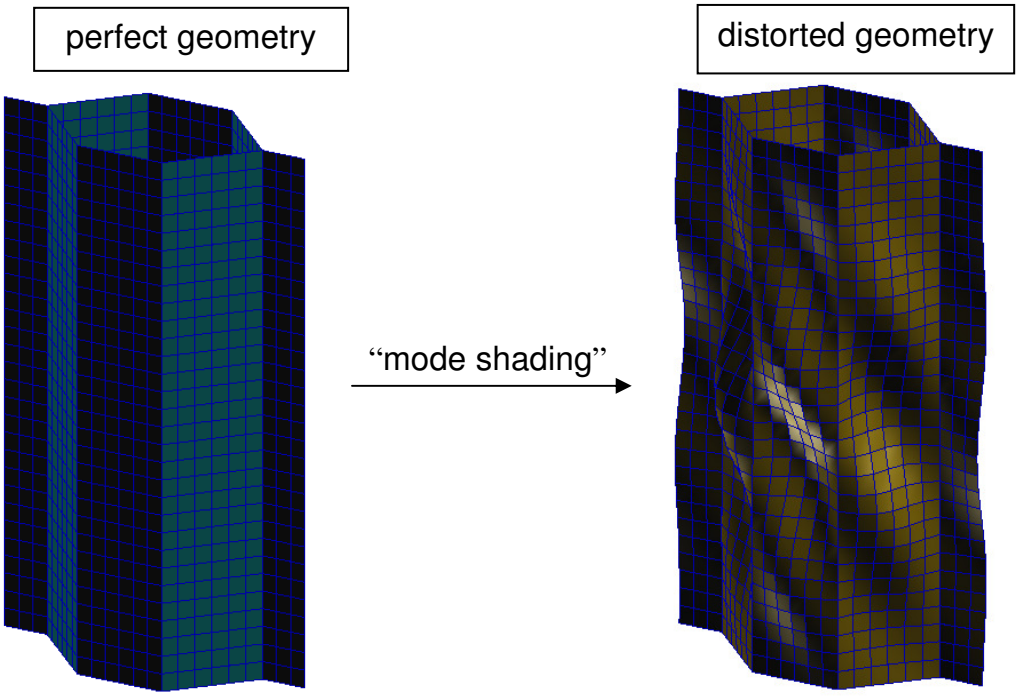

Figure 3-6: Introduction of geometrical imperfection via mode shading (distortion exaggerated for illustration)

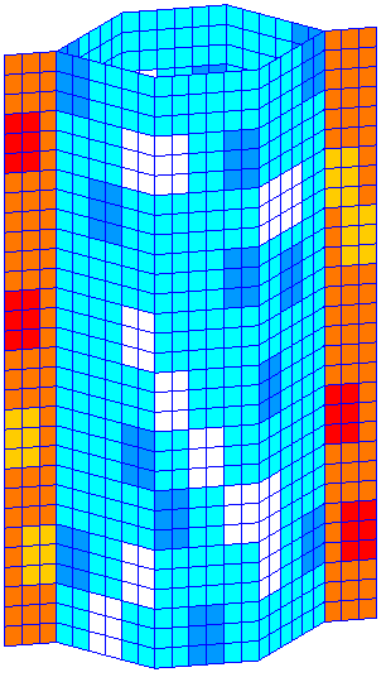

Figure 3-7: Imperfection modeling through cell wall thickness variation

3.5 Results from FE Analysis

Using an appropriate spring stiffness to account for the behavior of the loading fixture it was possible to obtain equivalent shear stress vs. relative displacement (between base and top of cell) curves as shown in Figure 3-8 and Figure 3-10 for the 5.3 core. Figure 3-8 only shows the directions which were also experimentally tested and the experimental curves are included for comparison. The deformed cell shapes obtained for these analysis runs are shown Figure 3-9. It is interesting to note that these modelled shapes compare very well with the deformed shapes actually observed on the tested coupons (see Figure 2-13), and that the areas that appear to be under tensile stress match to corresponding areas were fatigue cracks were observed in the fatigue tested coupons (see Figure 2-20 and Figure 2-21). This validates the accuracy of the model and offers further support to the conclusions given in Chapter 2. From the curves in Figure 3-8 it can be seen that the stiffness is matched very well for all the considered directions; however, the failure loads are over predicted. This is to be expected for the reasons described above. The over prediction tendency is slightly higher for the 0deg L direction were failure is dominated by buckling to a greater extent. Figure 3-10 shows the FEM curves from all the loading directions modeled. From these curves the predicted variation of shear strength with loading direction for the 5.3 core is plotted as shown in Figure 3-11 where it is also compared with the experimental values. An analogous graph was also obtained by modeling the 8.1 core (see Figure 3-12). Despite the over prediction it can be seen that for both core types the predicted variation trend is in agreement with the experimental results (seen for both core types) which suggest that the shear strength of the core only starts to increase significantly when the loading angle direction decreases below 45deg.

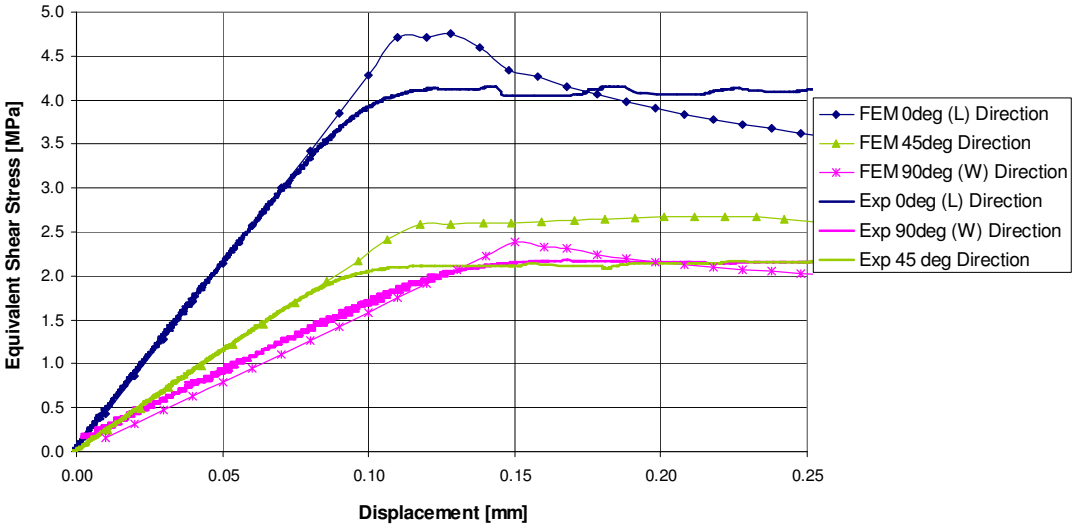

Figure 3-8: Comparison between experimental and finite element model (FEM) equivalent shear stress vs. displacement curves

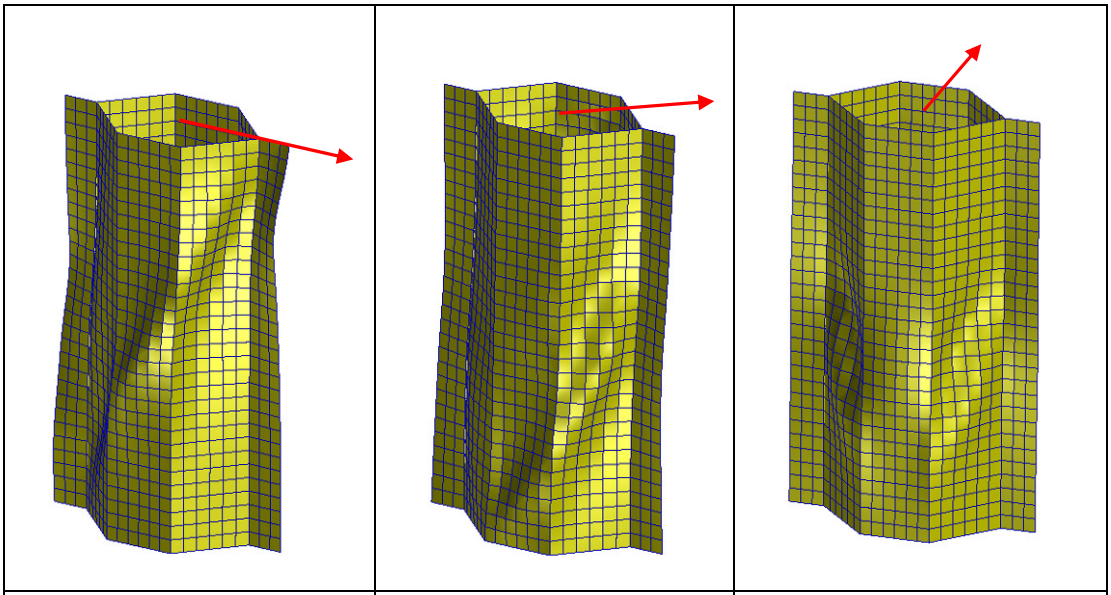

Figure 3-9: Cell deformations obtained from simulations runs loading the model in different directions (shear strain is ~2% for all cases)

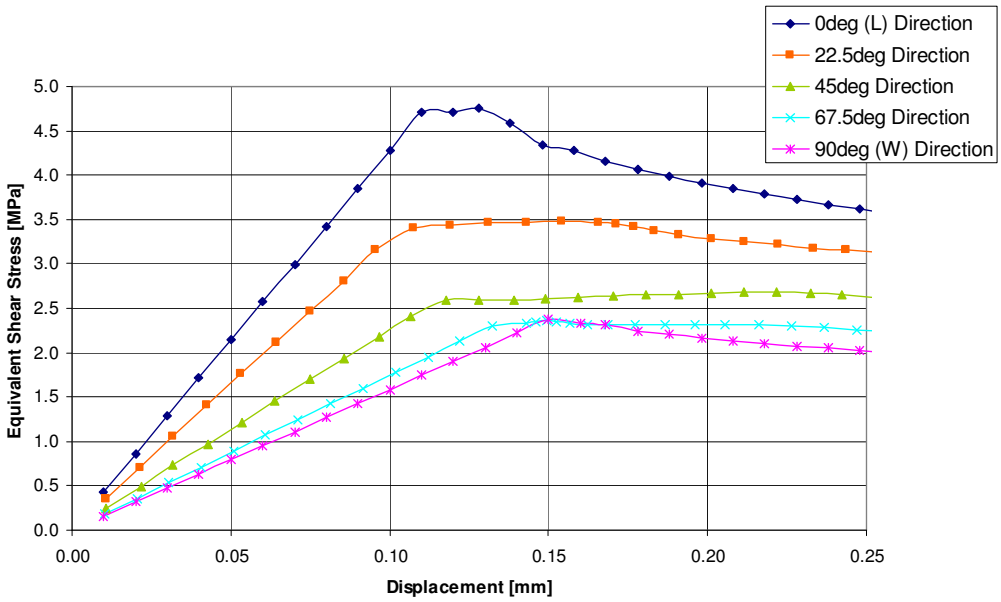

Figure 3-10: Finite element model (FEM) equivalent shear stress vs. displacement curves for all the directions considered

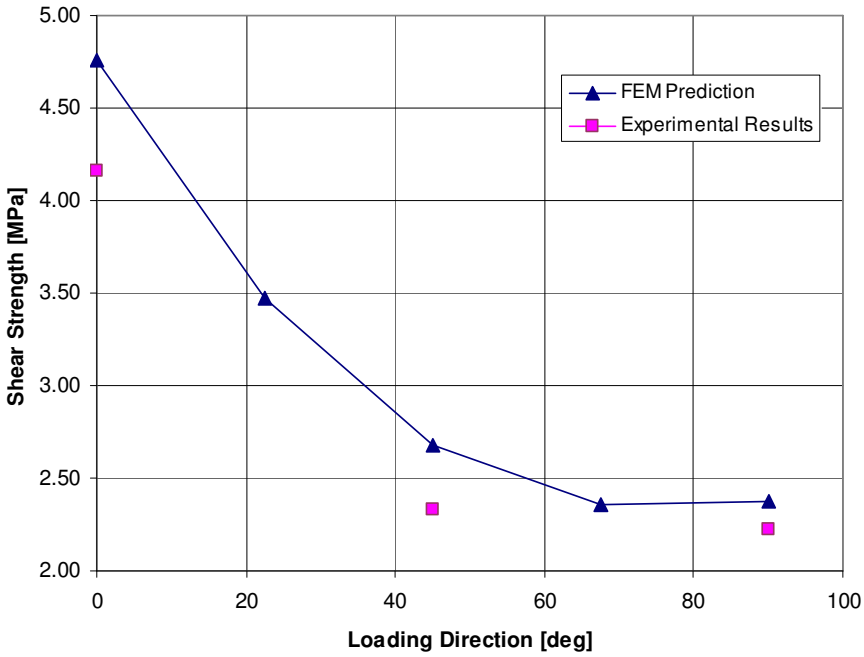

Figure 3-11: Variation of shear strength with loading direction for the 5.3 core

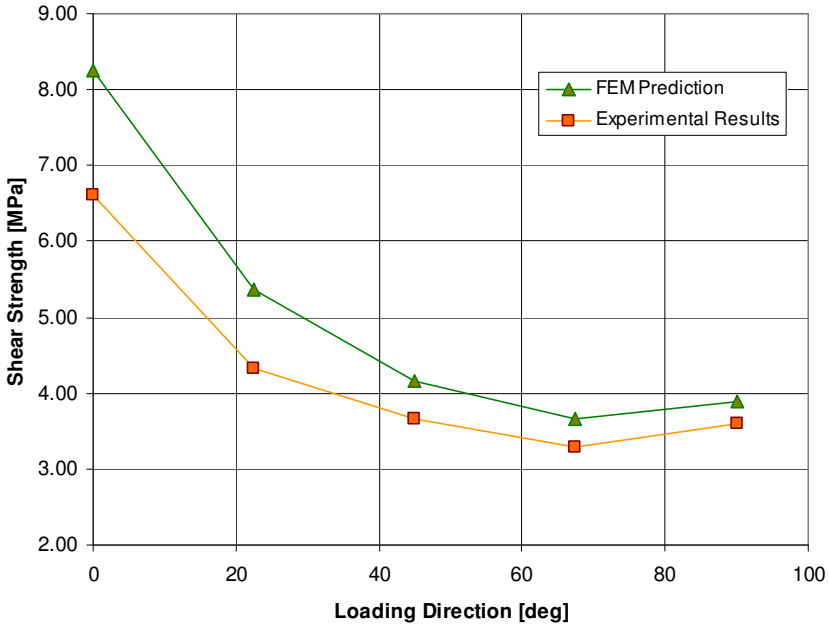

Figure 3-12: Variation of shear strength with loading direction for the 8.1 core

3.6 Conclusions

Using the finite element analysis it was determined that the non-linear relationship between shear strength and loading orientation observed in the experimental results presented in Chapter 2 is due to the tendency of the core to also displace cross-axis with respect to the loading orientation when the load is not aligned to one of the principal orientations. Constraining this cross-axis displacement has a significant effect on the relationship of both the shear modulus and the shear strength of the core with loading orientation. In real applications the level of cross-axis constraint will vary from case to case depending on how the panel is connected to surrounding structural components. Fully constraining the cross-axis displacement will give the highest core strength and core modulus values (for a given loading orientation) and a near linear relationship with loading orientation. On the other hand a free cross-axis constraint gives the lowest values of core strength and modulus with a minimum value of shear strength potentially sensibly lower than for the W orientation.

Chapter 4

4 Inserts in Honeycomb Panels

4.1 Introduction

Honeycomb panels are often used in spacecraft structures to provide mounting surfaces for the various components (e.g. electronic boxes, reaction wheels, batteries, etc.). Because of the weakness of the honeycomb core the transmission of loads between honeycomb panels and other structures or components is generally achieved via the introduction of hard points, often in the form of bobbin shaped metallic inserts (see Figure 4-1). Inserts can be split in two important categories depending on the method of integration into the honeycomb panel; hence a distinction is made between hot bonded inserts and cold bonded inserts (see Figure 4-2). Hot bonded inserts are integrated with foaming adhesive during sandwich panel production; whereas cold bonded inserts are potted with curing resin into an existing panel. For both insert designs the foaming adhesive and curing resin act as a filler material that distributes the loads from the insert to the surrounding sandwich structure. As can be seen in Figure 4-2, apart from the method of integration, hot bonded and cold bonded inserts also differ in terms of their arrangement within the sandwich structure.

A honeycomb panel incorporating hot bonded inserts is produced by laying down the inserts at the same stage as the honeycomb core, which has cut-outs at the locations where the inserts are to be placed. These are laid on top of the bottom facing sheet, which is covered in a layer of adhesive film. The sandwich is completed by laying down a second layer of adhesive film and the top facing sheet over the honeycomb core and inserts.

Hence in the hot bonded arrangement the insert is bonded to both the top and bottom face sheets and the insert height is equal to the core height. A hot bonded

inserts may thus be also regarded as a through-the-thickness type insert. For the cold bonded method of integration a hole has to be drilled in the sandwich panel to allow for insertion of the bobbin insert. The hole can be drilled as deep as necessary so the insert height does not have to be necessarily equal to the height of the honeycomb core. Hence a through-the-thickness arrangement can also be obtained by using the cold bonded method of integration but normally this is used to produce either fully potted or partially potted insert arrangements where the insert height is smaller than the core height. In the present work cold bonded inserts are treated as having either fully potted or partially potted arrangements.

Cold bonded inserts are the most used type of inserts in the space industry and the European Space Agency (ESA) has commissioned a number of studies to investigate their performance and has made the findings available in its Insert Design Handbook (IDH) [35], a comprehensive manual focused on the design, manufacture and testing of these inserts. On the contrary hot bonded inserts are not used as extensively in the space industry and have not been studied to the same extent. Although inserts have been widely used in the aerospace industry, little material has been published on this field. Furthermore, most of the published works only deal with cold bonded inserts and hence a study on both hot bonded and cold bonded inserts was conducted to assess their performance and effectively compare the two insert systems.

The experimental part of the investigation involved carrying out pullout tests on honeycomb panel coupons by loading them at a centrally located insert. A large number of hot bonded and cold bonded reference samples were tested in order to identify failure mechanisms and produce data samples for comparison. These data were also compared with the results obtained from an analytical model proposed in the IDH. A finite element model was also developed in order to evaluate the stresses generated by pull-out loads throughout the insert system and surrounding sandwich structure.

Figure 4-1: Alluminium Bobbin Insert

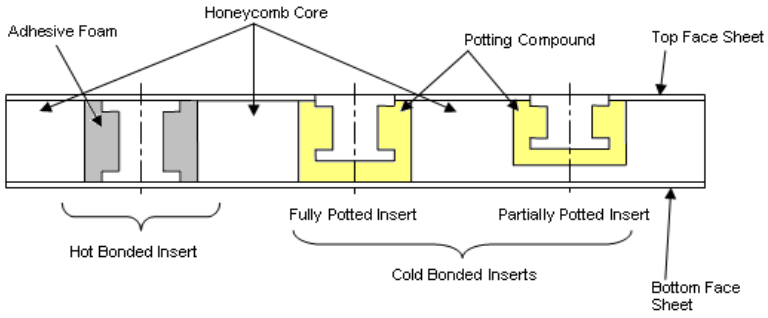

Figure 4-2: Illustration of insert types used in honeycomb panels

4.2 Literature Review

A brief review of some of the most noteworthy studies is presented in what follows. As mentioned in the previous section the fundamentals of insert design are covered in the ESA IDH [35]. The IDH mainly focuses on cold bonded inserts; however, many of the design principles are also valid for hot bonded inserts. In general most of the literature that can be found on inserts deals with their out-of-plane strength capability. Inserts has been investigated using mathematical models, numerical models and experimental investigations.

In Thomsen et al [53,54] a mathematical model which incorporates the transverse flexibility of the core is used to analyze the behavior of inserts subject to out-of-

plane loads. The model is used to investigate the differences in structural performance between through-the-thickness inserts and fully potted inserts. In Bozhevolnaya et al [55] and Bozhevolnaya and Lyckegaard [56] an analytical model initially developed to describe local effects across core junctions [57] is adapted to study plywood inserts in PVC core sandwich panels. The adapted model is used to show that stress concentrations due to material discontinuities can be significantly reduced by using patch core or structurally graded inserts to provide a more gradual transition from insert to core. The effect of insert/core boundary geometry was further investigated by Lyckegaard et al [58] using a finite element parametric study. Here a curved shape of the boundary was found to be most effective at reducing stress concentrations. Bunyawanichakul et al [59] carried out an experimental and numerical investigation on the performance of resin moulded inserts in aramid core sandwich panels relevant to aircraft structures and presented a numerical model which includes the nonlinear behavior of the core. In Raghu et al [60] the variability in pull-out strength of metallic inserts in aramid honeycomb sandwich panels is investigated and a higher variability is found for partially potted inserts. Kim and Lee [61] experimentally investigated the effect of insert shape on pull-out strength. Song et al [62] carried out an experimental study to investigate the effect of various design variables (e.g. core height and density, skin thickness, etc.) on metallic inserts in aramid core sandwich panels with CFRP skins.

4.3 Insert System Selection for Design

Besides the differences in structural performance between hot bonded and cold bonded insert there are other factors which must be considered when selecting which type to use for a particular application (e.g. cost and schedule). Before looking at their structural performance, this section briefly highlights the pros and cons associated with these two insert systems under various aspects. The use of hot bonded inserts presents the following advantages:

- Overall costs are lower because no machining or further work is required after the sandwich panel is manufactured.

- A very good bond is achieved with both face sheets resulting in a solid insert system construction. However, as will be seen later this does not necessarily mean that hot bonded inserts are always stronger than cold bonded inserts.

The use of hot bonded inserts poses the following disadvantages:

- It is more laborious to precisely position the inserts.
- When placing particularly tall and slender inserts there is a risk of toppling.

The use of cold bonded inserts presents the following advantages:

- Inserts are potted later on during the spacecraft manufacture, which means that layout changes can be easily implemented even at advanced project stages.
- Insert height does not need to be equal to core height, which can lead to mass savings if only mild loads need to be transmitted to a thick sandwich panel.

However, this insert system has the disadvantage that it is not possible to monitor the potting quality while injecting the potting compound through the bore holes of the top insert flange. An unsuccessful potting procedure, resulting in an incomplete filling or the presence of air inclusions in the potting, can significantly reduce the strength capability of the insert. The potting quality can only be checked after manufacture by means of X-Ray radiography.

Ultimately the insert selection depends on the end application but in general it can be said that cold bonded inserts are more suitable for large satellites were the panels used are likely to be thick and mass savings can be gained by using potted inserts. On the other hand hot bonded inserts are more suitable for small satellite programs which have shorter schedules (i.e. less chances of equipment layout changes from panel design/production) and where costs are big drivers.

4.4 Insert Capabilities

4.4.1 Load Types and Strength Capabilities

The insert system can be subjected to the following 5 basic types of loads: (a) Load normal to the plane of the sandwich away from the surface "tensile load"; (b) load normal to the plane towards the surface "compressive load"; (c) load parallel to the sandwich facing "shear load"; (d) bending load; (e) torsional load. These may act alone or in combination, but design should favor the first three load types since inserts are not suited to carrying bending and torsional loads. Torsional loads in particular should be just limited to screwing and locking torques only. This represents a potential area of improvement in insert design, however, excessive bending and torsional loads can be easily avoided by using insert groups to convert moments into simple forces which are either parallel or normal to the insert axis (e.g. bending loads can be avoided by using coupled inserts which convert the load to normal tension/compression).

Apart from shear the normal tensile and compressive load carrying capabilities are the most important strength parameters in defining the structural performance of inserts. In the IDH, strength data regarding the structural performance of cold bonded inserts is limited to normal tensile and compressive loads, and the literature available on the topic of inserts in general is predominantly concerned with these two load types. The work presented in this Chapter is focused on the static strength capability of inserts subject to normal tensile loads. In Chapter 7 the strength capability of hot bonded inserts is also considered.

4.4.2 Failure Modes under Normal Tensile Loads

In the Insert Design Handbook (IDH) [35] it is shown that, for a given potting height h_p, the decisive failure modes affecting the static strength capability P_{SS} of a cold bonded insert subject to a normal tensile load are primarily influenced by the core height, c. In the graph shown in Figure 4-3 it can be seen how the P_{SS} of a cold bonded insert varies with core height, c. Looking at the P_{SS} curve it is possible to

split the graph into three areas, each of which is associated with a failure mode. In the first part of the graph, starting from $h_p = c$, the P_{SS} increases quasi-linearly with core height. Here the insert system fails by shear rupture of the core surrounding the insert so the property limiting the P_{SS} is the shear strength of the core. The P_{SS} increases quasi-linearly with core height because of the corresponding increase in area over which the shear load is distributed. As the core height increases the insert becomes partially potted and the core underneath the potting is subjected to tensile stress. When $c - h_p$ reaches a critical value the tensile stress underneath the potting reaches the tensile strength of the core, and the second failure mode (coinciding with the second part of the graph) comes into effect. Now the insert fails by the combination of shear rupture of the core around the potting and tensile rupture of the core underneath the potting occurring together: the P_{SS} is then simultaneously limited by the core shear strength and the core tensile strength and, as illustrated in the second part of the graph, is almost independent of further increases in core height. This is because due to the rigidity of the potting only part of the full core shear strength is used (i.e. the critical shear strength of the core is not reached). The load part carried by shear stresses in the core around the potting decreases with the core shear stress as c increases.

The potting underneath the insert is also subjected to tensile stress which increases with core height. If this stress exceeds the tensile strength of the potting compound before the tensile strength of the core is reached the insert will fail by tensile rupture of the potting. This is likely to occur for strong cores when a certain core height is reached. As can be seen in the graph, for this third failure mode, further increases in core height results in a mild decrease in P_{SS}. This is because, with further increases in core height the panel area around the insert becomes more rigid and the proportion of load carried by normal stresses in the potting increases slightly. Owing to the higher stiffness of the potting no advantage can be gained from the shear strength of the core.

The outer diameter of the insert (i.e. the diameter of the flanges) has a major influence on the P_{SS} for all the failure modes discussed above. This is because it determines the potting radius and consequently the area over which shear loads are distributed over the walls of the surrounding core, and because it determines the area underneath the insert and the potting over which normal tensile loads are carried.

If this failure mode criteria proposed in the IDH is applied to hot bonded inserts as well it can be said that, because the insert height h_i is always equal to the core height h_c, shear rupture of the core around the insert should be the only relevant failure mode for this insert type and that static strength capability should always increase quasi-linearly with core height. It follows that, for equivalent insert outer diameter, equivalent core specification and equivalent core height, the static strength capability of a hot bonded insert should be very similar to that of a fully potted cold bonded insert. However, because the insert is bonded to both the face sheets, the through-the-thickness design of a hot bonded insert looks and is generally recognized as being stronger than the fully potted design. To actually determine the performance difference between the two designs, an experimental study was carried out involving pull-out tests on hot bonded coupons and fully potted cold bonded coupons.

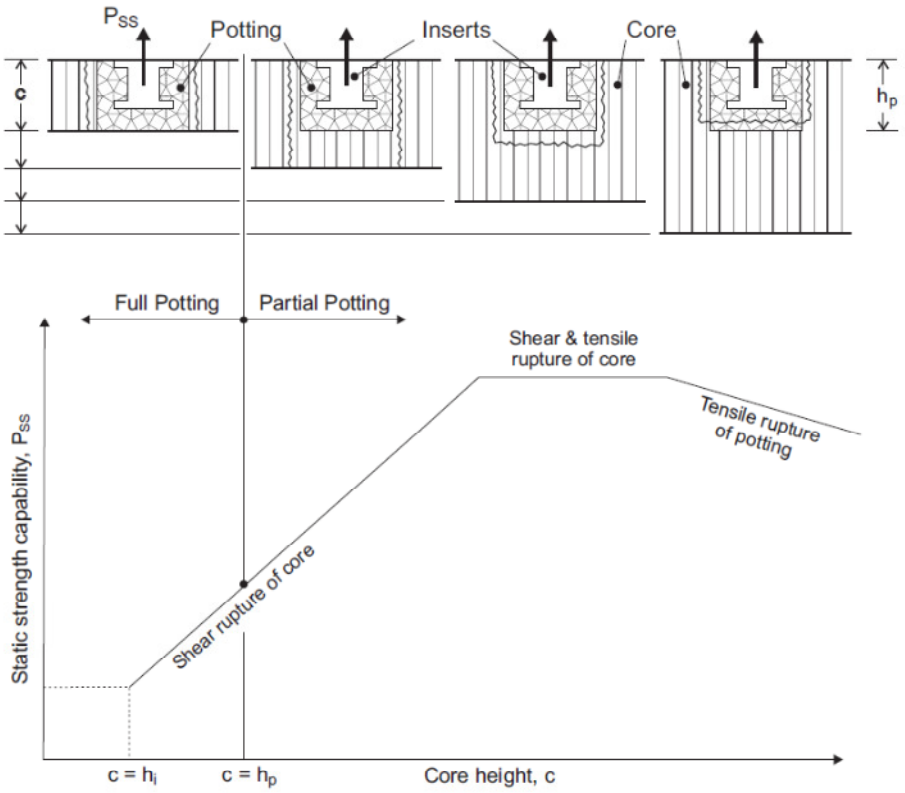

Figure 4-3: Influence of core height on failure modes

4.5 Material Specimens

Hot bonded insert coupons and fully potted cold bonded insert coupons were produced in order to conduct pull-out tests. To ensure a relevant comparison the same sandwich panel specifications were used for both of these coupon types. The sandwich structure consisted of two 2014 aluminum alloy face skins 0.5 mm in thickness, sandwiching a 19 mm thick aluminum core, designated as ¼" - 5056 - 0.0025" (which should be read as: cell size in inches – Al alloy – foil thickness in inches), 6.35 mm in cell size and 83 kg/m^3 in density. All reference samples had dimensions 80 × 80 × 20 mm. The face skins were bonded to the honeycomb core using Redux 319 adhesive film.

The hot bonded insert coupons (see Figure 4-6 (a)) incorporated a centrally located aluminum bobbin insert, 16 mm in outer diameter, 19 mm in height (i.e. same

height as the core). The coupons were obtained by cutting a larger panel which had multiple hot bonded inserts. The inserts were originally introduced in the sandwich structure during panel manufacture using Redux 219/2-NA foaming film adhesive as the filler material. This is an epoxy based foaming adhesive, initially presented as sheet film, which after application expands upon curing by a ratio in the range 1:1.9 to 1:1.4. The panel with the hot bonded inserts was produced using the standard procedure used to produce SSTL spacecraft panels. The process involves the following four layup steps. Firstly both the bottom and top face sheets are laid down and then a layer of Redux 319 film adhesive is laid on top of each one. The second step is to lay down the bobbin inserts at the desired locations on the bottom face sheet using location pins to keep them in place (an example of a panel at this stage of manufacture is shown on Figure 4-4). A few layers of foaming film adhesive are wrapped around the bobbin insert (see Figure 4-7 (a)) before laying it down. The third step is to also lay down the honeycomb core (on the lower face sheet) which has clearance holes (these are punched out using a special tool) in correspondence of the insert locations (an image of a panel at this stage of manufacture is shown in Figure 4-5). Figure 4-4 and Figure 4-5 also show edge inserts which are typically used to protect the edge of the panel and provide a localized edge reinforcement to allow for bolting to other panels. The fourth and final step is to lay down the top face sheet with its layer of film adhesive against the exposed core to close off the panel. The laid up panel is then placed in a vacuum bag to provide the necessary contact pressure between the bond areas. The panel in its vacuum bag is then placed in an oven at ~170ºC to cure the adhesive film and the foaming adhesive which expands to fill the cavity between the bobbin insert and the surrounding walls of the open core cells.

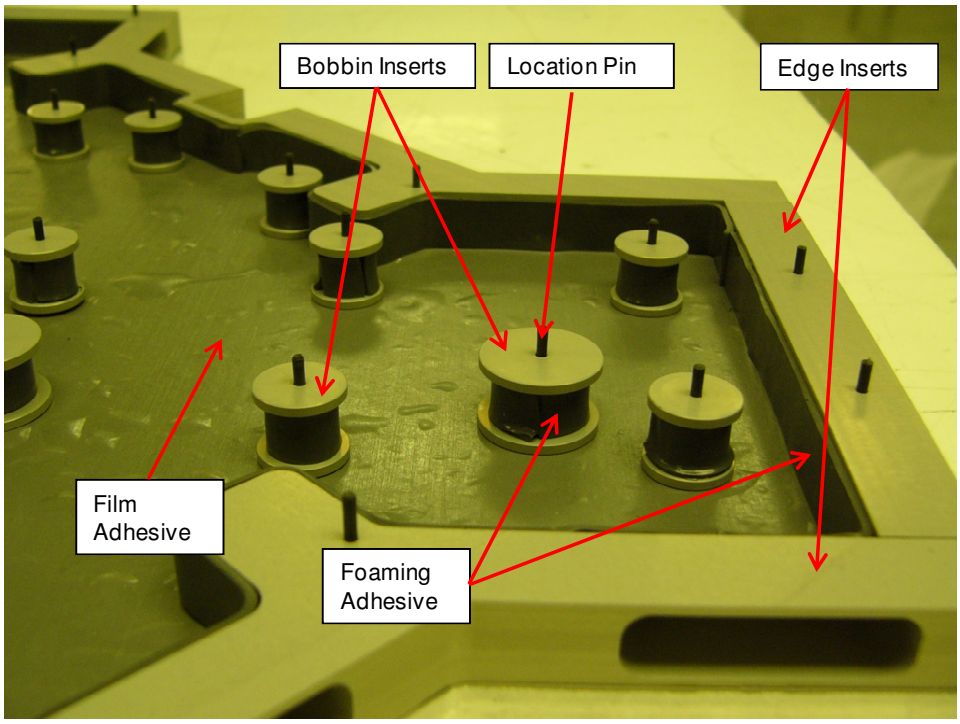

Figure 4-4: Example of an SSTL panel in an early stage of manufacture with the bobbin inserts laid down and held in place via location pins

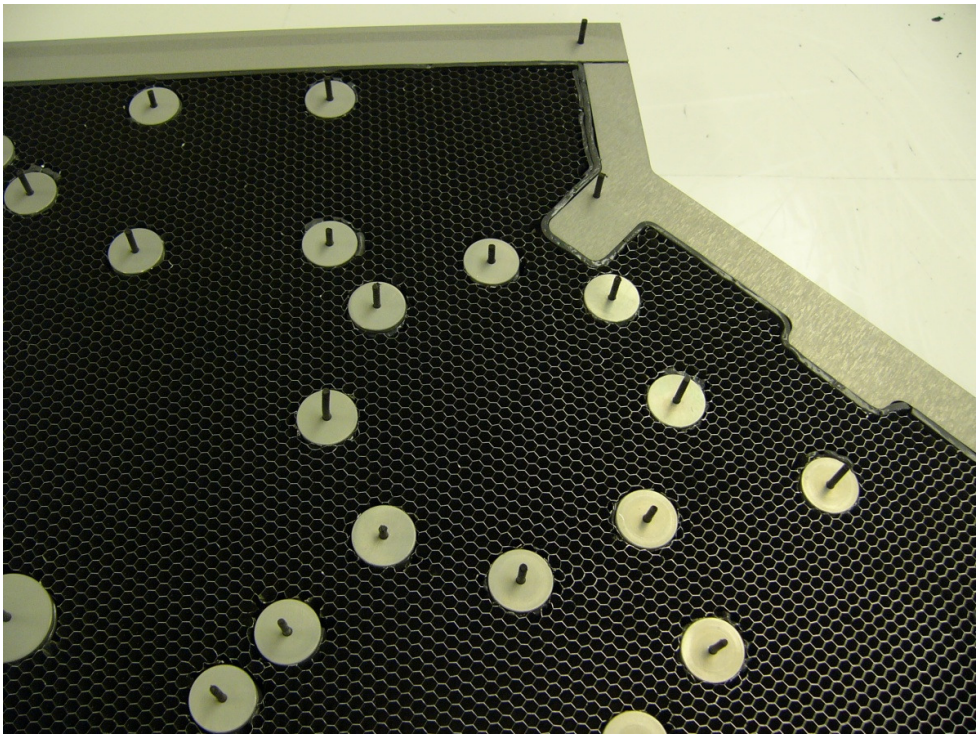

Figure 4-5: Example of an SSTL panel with the inserts and honeycomb core in place

For the cold bonded coupons (see Figure 4-6 (b)) aluminum bobbin inserts were potted at the center of sandwich panel squares cut to match the dimensions specified above. Here, the inserts were potted in the coupons using Stycast 1090 as the potting compound. This is an epoxy based encapsulant which is liquid when applied and then hardens upon curing without expanding (the product is actually quoted as having low cure shrinkage). In this installation procedure the bobbin is inserted in the machined hole and then, as its top flange is maintained flush with the top surface of the panel, the potting compound is squirted via one of the holes in the flange to fill the cavity (see Figure 4-7 (b)). A second hole is required to allow for venting. The outer diameter has a major influence on P_{SS} so in order to ensure a relevant comparison with the hot bonded reference samples the bobbin inserts used here were also 16 mm in outer diameter. Again to maintain a relevant comparison a fully potted arrangement was chosen since, according to the existing insert capabilities theories described earlier, the failure mode should be the same as for the hot bonded configuration. To obtain a fully potted arrangement bobbin inserts 16 mm in height were used for the cold bonded coupons.

For both coupon types the bobbin inserts were made in 6082 aluminum alloy and the mechanical connection could be achieved through an M5 threaded hole at the center of the bobbin.

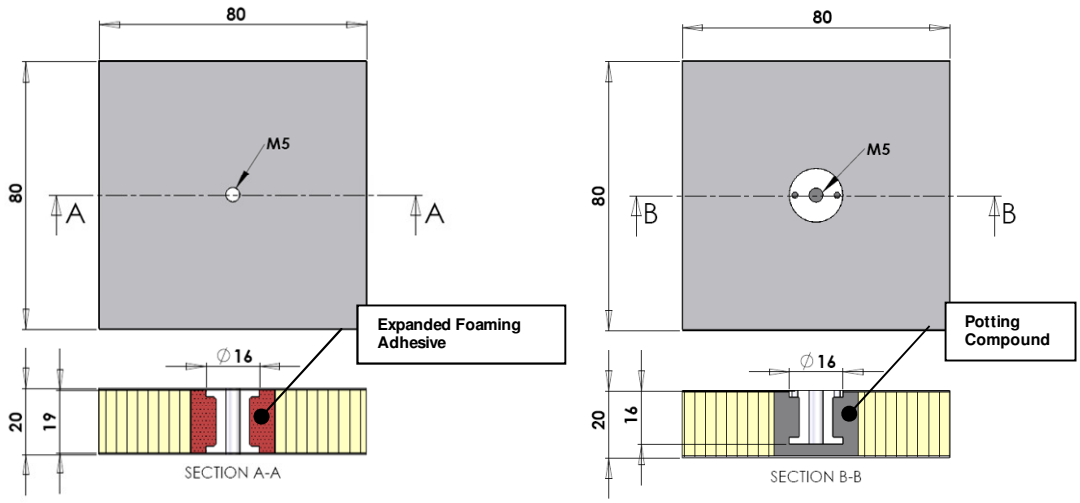

(a) Hot Bonded Coupon **(b) Cold Bonded Coupon**

Figure 4-6: Dimensioned drawings of coupons

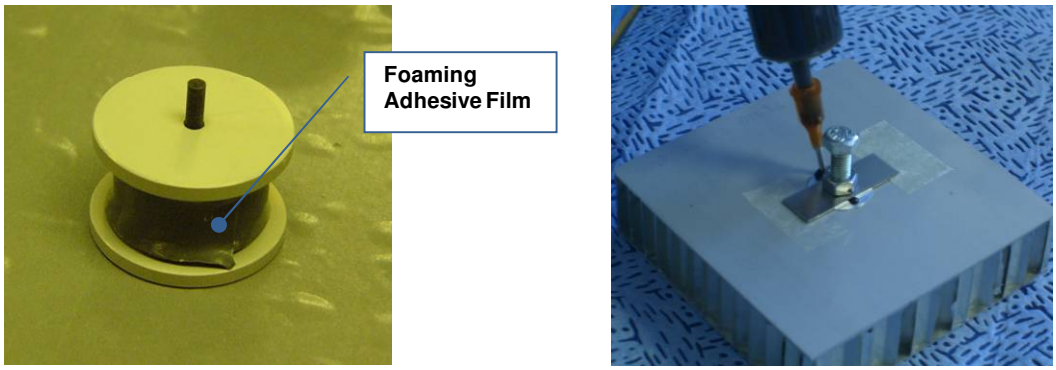

(a) Example of a Hot Bonded insert laid down with a film of foaming adhesive during sandwich panel manufacture

(b) Injection of potting compound during Cold Bonded insert installation

Figure 4-7: Installation procedures for Hot Bonded (a) and Cold Bonded (b) inserts

4.6 Experimental Procedure

All the coupons were subjected to pull-out tests using an Instron 8802 universal servo-hydraulic testing machine. The machine is equipped with a 100 kN load cell and an LVDT incorporated in the lower cross-head. The load and cross-head

signals were recorded through an external PC using the DasyLab data acquisition system. The testing was conducted at room temperature and in accordance with ESA guidelines outlined in the IDH. To comply with these guidelines a specifically designed test fixture (see Figure 4-8) was used to hold the samples and expose a free circular area 70 mm in diameter around the insert. The set-up, used for all the tests, was installed in the Instron machine as shown in Figure 4-9 and is described as follows: An M5 bolt is connected to the reference sample via the female threaded part of the insert. The shank of the bolt is contained within a rectangular steel block, which can be clamped into the hydraulic grips of the upper crosshead. The lower part of the test fixture has a hole in which a headed steel dowel pin is inserted. The cylindrical body of the pin can be clamped into the hydraulic v-grips of the lower crosshead. Once the described set-up was achieved, starting from an unloaded condition, the specimens were loaded at constant cross-head displacement rate of 1 mm/min until ultimate failure occurred. During the tests load data and crosshead displacement data were recorded at a sampling rate of 10 Hz.

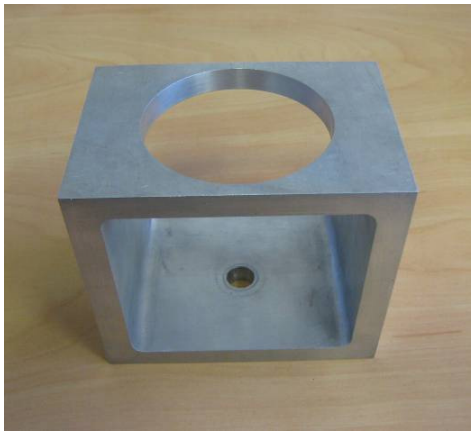

Figure 4-8: Al-alloy test fixture with 70 mm diameter circular cut-out

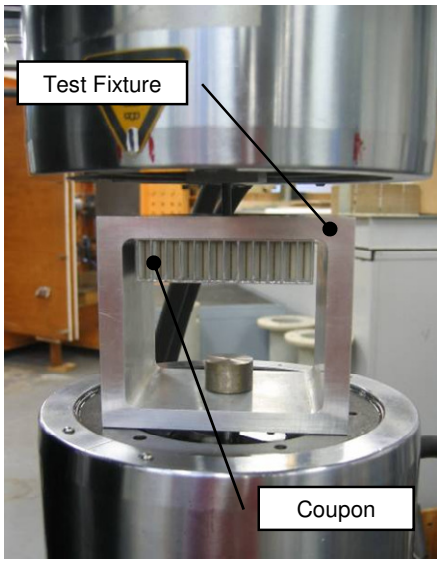

Figure 4-9: Arrangement of the coupon and test fixture installed between the crossheads of the universal testing machine

4.7 Experimental Results

A total of 23 hot bonded and 8 cold bonded coupons were tested as described above. Typical load versus crosshead displacement curves obtained for both tested insert types are shown in Figure 4-10. Based on the behavior of these load-displacement curves it is possible to split the plot into three regions. In the first part of the plot the curves are nonlinear, which is probably a result of the establishment of contact between the coupons and the test fixture. In the second part of the plot the curves show a nearly linear behavior indicating that near elastic deformation is taking place and that no significant damage is occurring. In the third part of the plot the curves are nonlinear due to the progressive damaging of the insert systems. Here, as damage takes place the slope of the curves progressively reduces until peak load is reached. Finally, the damage is so great that most of the strength is lost and the load-displacement curve drops sharply. From the linear part of the curves it can be seen that the slope is steeper for the cold bonded coupon. This was the case for all the tested coupons and is an indication that the overall insert system stiffness was higher for the cold bonded coupons.

From the plot it can be seen that the cold bonded insert coupons failed at a higher load than the hot bonded insert coupons. For all the tested coupons the insert static strength capability was taken as the peak load from the obtained load-displacement curves. The number of data samples obtained for both test types was large enough to justify statistical processing and generating minimum $P_{SS,A}$, A-basis[1] and, $P_{SS,B}$, B-basis[2] allowables. These were calculated using the following expression

$$\boldsymbol{P_{SS,A} = P_{SS,av} - s \times k_A} \qquad \textbf{(4-1)}$$

[1] A-basis: 95% confidence that 99% of the samples will exceed the allowable

[2] B-basis: 95% confidence that 90% of the samples will exceed the allowable

$$P_{SS,B} = P_{SS,av} - s \times k_B \quad \textbf{(4-2)}$$

where $P_{SS,av}$ is the average strength capability and k_A and k_B are one-sided tolerance-limit factors which vary with sample size. Values for these can be found in tabulated format in MIL-HDBK-5 [63]. The processed results are summarized in Table 4-1. From these results it can be seen that the tested cold bonded inserts achieved a higher failure load. Despite the lower number of tested samples the A-basis and B-basis results are also higher for the cold bonded insert results owing to their low standard deviation.

	Hot Bonded	Cold Bonded
$P_{SS,av}$ [kN]	5.60	6.18
No. of Samples	23	8
Standard Deviation	0.46	0.29
$P_{SS,A}$ [kN]	4.11	4.94
$P_{SS,B}$ [kN]	4.73	5.46

Table 4-1: Experimental results

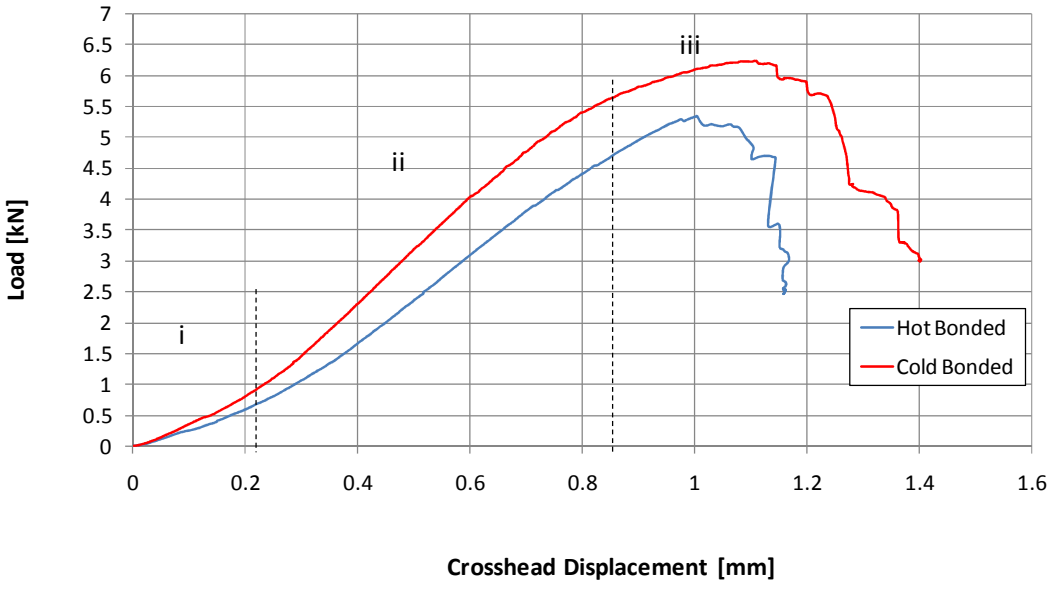

Figure 4-10: Typical load Vs. cross-head displacement curves for hot bonded and cold bonded coupons

After testing, some of the reference samples were sectioned across the center in order to check the manufacturing quality and identify failure modes (see Figure 4-11 and Figure 4-12).

By visual observation, it is evident that, for both the hot bonded and the cold bonded coupons, failure initiates in the core by shear buckling of the cell walls. However, this does not cause an immediate load drop since, initially, the diagonal cell buckling will produce a diagonal (Wagner) tension field which still retains load carrying capacity. This is confirmed later on by comparing these experimental results with those obtained in the numerical study and the shear buckling instability calculation presented in section 4.9. This post-buckling phase is likely to correspond to the relatively gradual drop in stiffness that can be observed in Figure 4-10 between regions ii and iii. Eventually, as the yield strength is reached the cell walls lose their structural integrity leading to the sudden load drop that can be seen in region iii. No manufacturing defects were detected in the sectioned coupons.

Figure 4-11: Image of a hot bonded reference sample sectioned after testing

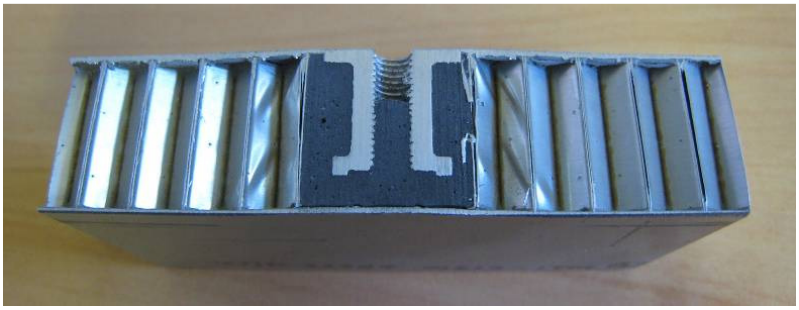

Figure 4-12: Image of a cold bonded reference sample sectioned after testing

4.8 Theoretical Study of Tested Insert Systems

The Insert Design Handbook (IDH) contains a vast range of data concerning the normal tensile and compressive strength capabilities of cold bonded inserts. These data are presented in the form of diagrams (see Figure 4-13) which, for a given core type and insert size; show how the minimum and average load carrying capability values vary with core height.

The honeycomb cores for which diagrams have been produced were 0.02 or 0.03 mm in foil thickness and 3.2 or 4.8 mm in cell size, however the honeycomb core used for the experimental work described here is heavier with 0.06 mm foil thickness and 6.35 mm cell size so these diagrams are not directly applicable.

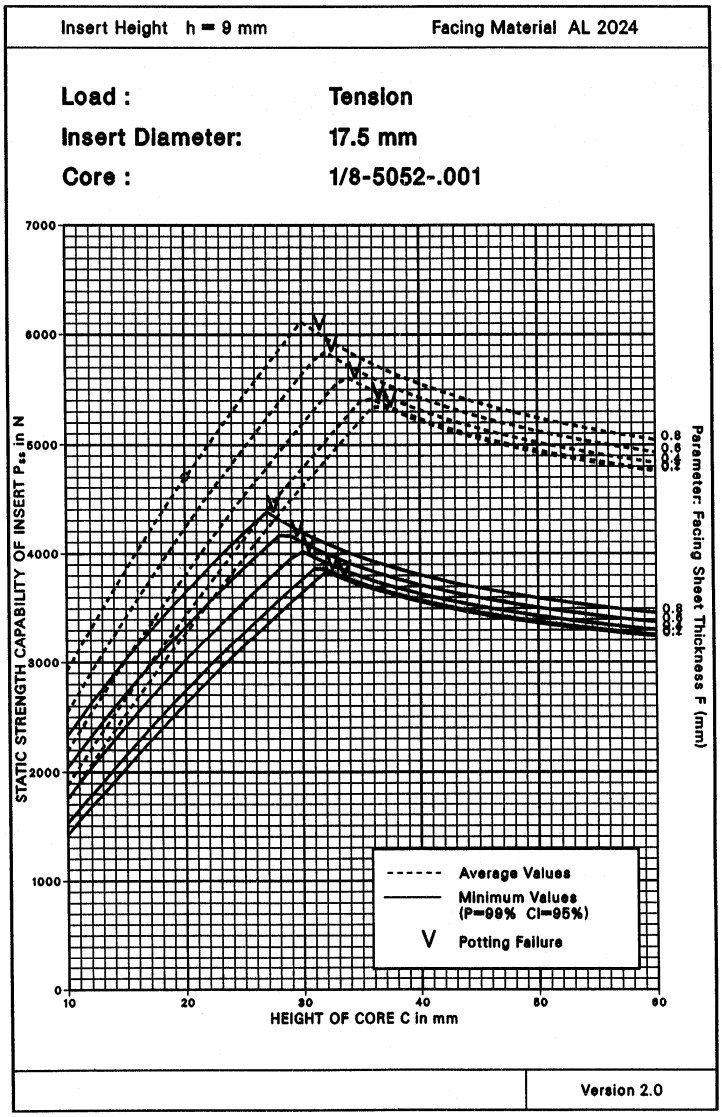

Figure 4-13: A typical diagram illustrating load carrying capabilities of cold bonded inserts [35]

The diagrams are not generated from direct experimental data but are actually produced using an analytical method which has been compared with test results to verify its validity and produce reliability coefficients. Hence, using this method it is possible to generate a diagram relevant to the core type used in the tested reference samples. The analytical approach is based on an analytical model proposed in Ericksen [64] which provides a means of determining the distribution of shear stress in a sandwich panel that is loaded normal to the facing plane. The model is

based on the following assumptions: (a) The effect of the bending of the core is negligible; (b) the transverse shear stress in the core is constant over the thickness of the core; (c) the transverse shear deformations in the facings are negligible; (d) the two facings have the same curvature.

The full formulation of the analytical approach used in the IDH is reproduced in Appendix B. This formulation, based on the further assumptions that the face skins have equal thickness and that the core height is large compared to face skin thickness, shows that the maximum shear stress in the core is given by

$$\tau_{\max} = \frac{P}{2\pi bc}\frac{\beta}{\beta+1}K_{\max} \quad \textbf{(4-3)}$$

where P is the applied load, b is the potting radius, c is the core height and β is the core height to face skin thickness ratio c/f (see Figure 4-14). K is a parameter which depends on the radial position from the center of load application. K is equal to $K_{\max}$ at the position of maximum core shear stress $r_{\tau,\max}$ (an expression for this is also shown in Appendix B).

If the failure mode is by shear rupture of the core then failure will occur when the load is such that $\tau_{\max}$ exceeds the circular shear strength of the core $\tau_{C,crit}$. For hexagonal honeycomb cores the number of single cell walls in the L direction is 72% greater than in the W direction [35], so the circular shear strength of the core is related to the shear strength of the core in the W direction by

$$\tau_{C,crit} = 1.36 \times \tau_{W,crit} \quad \textbf{(4-4)}$$

The above expression can be directly used to determine the insert capability by rearranging as follows

$$P_{crit} = \frac{2\pi bc\,\tau_{C,crit}}{C^{*}K_{\max}} \quad \textbf{(4-5)}$$

with $C^{*} = \beta/(\beta+1)$

This expression will normally apply to through-the-thickness, fully potted inserts and partially potted inserts with a small c-h_p value. However, as seen in section 4.4.2, for partially potted inserts with a large c-h_p value, failure is more likely to occur due to rupture of the core underneath the potting or rupture of the potting underneath the insert (for heavier cores). In these cases the insert capability cannot be described by Eq. (**4-5**) alone since other load contributions need to be considered. For a partially potted insert in aluminium core the load applied to the insert consists of 3 parts: (i) Load applied to the upper facing; (ii) load part carried by shear stresses in the core around the potting; (iii) load part carried by normal stresses in the core underneath the potting. Theoretically shear rupture of the core and tensile rupture of the core should not occur together. However, the IDH states that due to non-linearity effects $\tau_{C,crit}$ and $\sigma_{C,crit}$ are actually reached simultaneously. Hence by combining the load contributions it is possible to show (see Appendix B) that the capability of a partially potted insert is given by

$$P_{pcrit} = \frac{1}{2} P_{crit} + \pi r_{\tau\max} \left(2h_p - c\right) \tau_{C,crit} + \pi r_{\tau\max}^2 \sigma_{C,crit} \qquad \textbf{(4-6)}$$

where $\sigma_{C,crit}$ is the tensile or compressive circular strength of the core (depending on whether the load is tensile or compressive).

For a partially potted insert in a heavy aluminium core failure is more likely to occur in the potting and hence the relevant load contributions are different. These can still be divided in 3 parts: (i) Load applied to the upper facing; (ii) load part carried by shear stresses in the core around the potting over the insert height; (iii) load part carried by normal stresses in the resin underneath the insert. By combining these load contributions it is possible to show (see Appendix B) that the capability of a partially potted insert in heavy aluminium core is given by

$$P_{R,crit} = \frac{2P_{NR,crit}}{1 + \dfrac{\left(c - 2h_i\right) r_{\tau,\max}}{cb} C * K_{\max}} \qquad \textbf{(4-7)}$$

where $P_{NR,crit}$ is the critical load that can be carried by normal stresses in the resin underneath the insert and is given by

$$P_{NR,crit} = \pi b_R^2 \sigma_{R,crit} \quad \textbf{(4-8)}$$

where b_R corresponds to the real potting radius and $\sigma_{R,crit}$ is the critical tensile strength of the resin.

Equations 4-5 to 4-7 can be used to predict the capability and the failure mode of a given insert system. These equations should be used as follows: if the insert is through-the-thickness or fully potted then its capability will be described by P_{crit} – for a partially potted insert the decisive failure mode is not certain so P_{crit}, $P_{p,crit}$ and $P_{R,crit}$ should all be evaluated. The lowest out of the three values obtained will represent the actual insert capability P_{SS} and indicate the mode of failure. Minimum or average values of P_{SS} can be calculated using Eqs. 4-5 to 4-7 by prescribing minimum or average values of potting dimensions (b, b_R, h_p), core properties (τ_{Ccrit}, $\sigma_{C,crit}$) and potting material strength ($\sigma_{R,crit}$). The final P_{SS} value is determined by multiplying by reliability coefficients found in the IDH which have been determined by comparing the model with test results. The resulting minimum P_{SS} values are regarded as A- basis values meaning that 99% of specimens are expected to exceed this value with a confidence level of 95%.

Implementing this analytical approach it was possible to accurately reproduce the diagrams shown in the IDH. By using the appropriate parameters and material properties (see Table 4-2) it was thus possible to generate a diagram for the core specifications and insert dimensions used for the tested cold bonded insert reference samples (see Figure 4-15). From the diagram it is possible to see that for a core height of 19 mm the behavior of both curves is still quasi-linear indicating that the model predicts shear rupture of the core around the potting as the failure mode. The predicted average $P_{SS,av}$ value is 6.14 kN and the minimum $P_{SS,min}$ value is 4.38 kN.

The diagram in Figure 4-15 was produced for an insert height of 16 mm. However the IDH states that the diagram would also be applicable to other h_i values. The insert height only controls the break of the curves, where the quasi-linear behavior stops and the failure mode changes. For higher h_i values the curve break occurs at higher core height values and vice-versa. At a core height of 19 mm (i.e. the hot bonded insert configuration) the behavior of the curves would still be quasi-linear and indicate the same load carrying capability values $P_{SS,av}$ = 6.14 kN and $P_{SS,min}$ = 4.38 kN. This means that the analytical model does not distinguish between the hot bonded and cold bonded reference samples. The reason for this is that in the formulation proposed by Ericksen only the shear stress distribution through the sandwich core is considered and the normal load is assumed to be applied over a rigid circular disk which the IDH adaptation has a radius equal to the potting (filler material) radius. Hence for the core shear stress mode of failure the IDH model does not consider the insert system geometry or the stiffness of the filler material.

Both these analytical results and the average static strength capability results obtained from the experiments are summarized in Table 4-3. For average static strength capability values there is a very good correlation between the analytical result and the experimental result obtained for the cold bonded coupons, while for the hot bonded coupons the experimental average is about 10% lower. The reason for the latter discrepancy was found by conducting a numerical study and is explained in section 4.9.

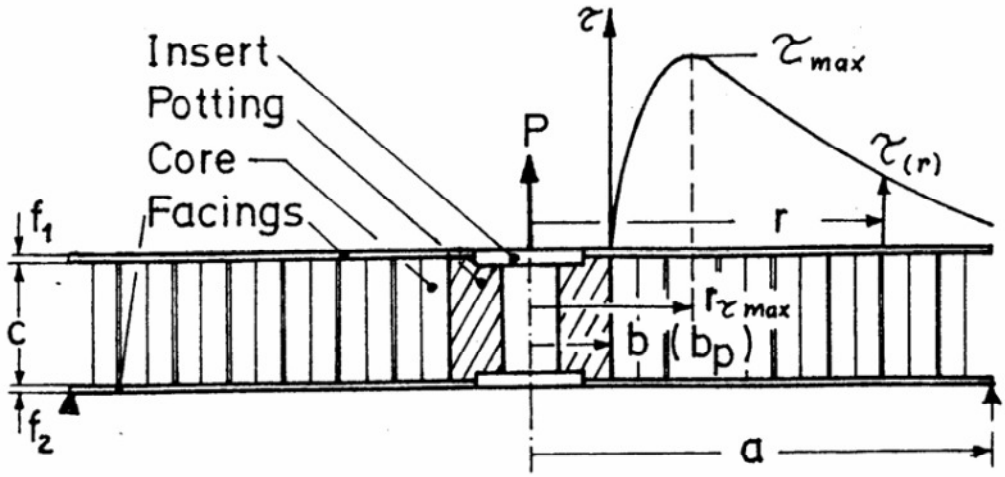

Figure 4-14: Shear stress distribution around fully potted insert [35]

	Honeycomb Core[3]		Filler/Potting Material[4]
	Circular Shear Strength [MPa]	Normal Tensile Strength [MPa]	Tensile Strength [MPa]
Min	2.30	9.34	14
Typical	2.81	10.38	18

Table 4-2: Minimum and typical critical values used for the honeycomb core and the potting material

[3] Honeycomb core property values sourced and derived from ESA Composite Design Handbook[9].

[4] Potting material values sourced from manufacturer quoted values for Stycast 1090.

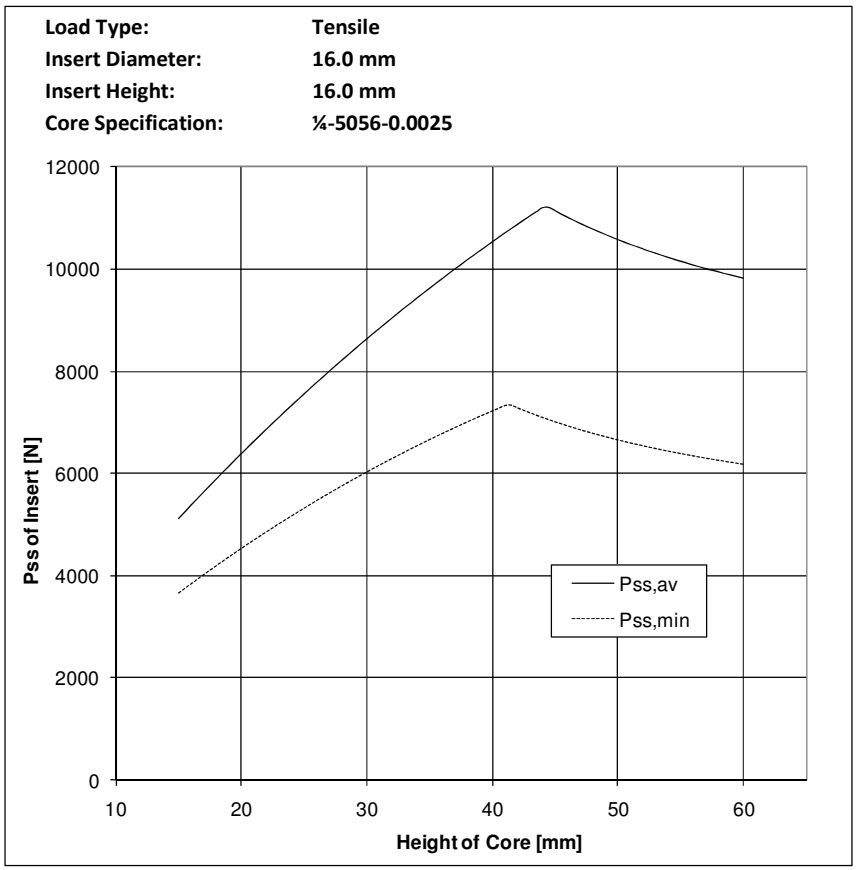

Figure 4-15: Load carrying capability plot produced using the analytical model with the parameters of tested cold bonded samples

Insert Configuration	Experimental Results	Analytical Results	
	$P_{SS,av}$ [kN]	$P_{SS,av}$ [kN]	$P_{SS,min}$ [kN]
Hot Bonded Geometry	5.60	6.14	4.38
Cold Bonded Geometry	6.18		

Table 4-3: Summary of experimental and analytical results

4.9 Finite Element Study

4.9.1 Description of the Finite Element Models

An investigation using the finite element method was conducted in order to determine why the fully potted cold bonded insert coupons outperformed the hot bonded insert coupons. Because failure initiates in the core the structural

performance of the two insert systems can be compared by looking at the behavior of the honeycomb cell walls. However, rather than going through the complexities of attempting to predict the exact buckling loads via a computationally expensive non-linear analysis, here the approach that was taken was to use a simpler and more reliable linear analysis to look at the magnitude of the stress fields generated in the honeycomb cell walls. Two models corresponding to the two coupon types were created in Patran and solved using Nastran (see Figure 4-16 (a) and (b)). Using symmetry constraints it was possible to model only one half of the coupons. The detailed three dimensional geometry of the honeycomb core was modeled using quadrilateral shell elements. The modeling of this part was based on the ¼"-5056-0.0025" core used for both coupons and included the double wall thickness along the ribbon direction. The face skins were also modeled using quadrilateral shell elements. The insert, adhesive foam and potting compound were all modeled using quadrilateral brick elements.

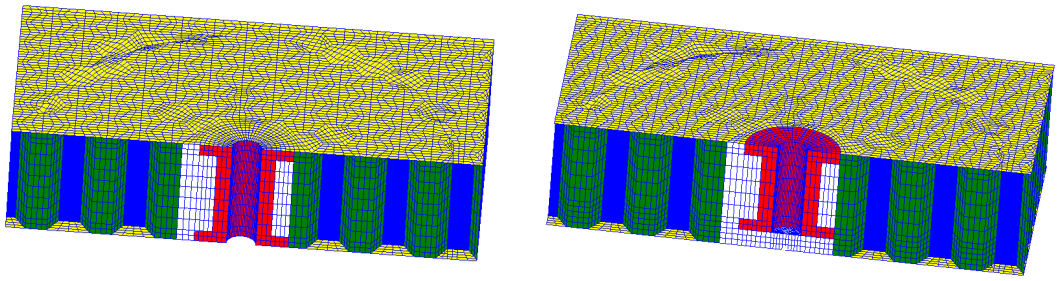

(a) Hot bonded coupon model (b) Cold bonded coupon model

Figure 4-16: Meshing of the finite element models

Looking at these models it can be seen that the core is not symmetric with respect to the centrally located insert. This was not intentional and is simply a result of the construction process used for the model, starting from the core and then (cutting out a cylindrical section to accommodate the insert system). Comparing with the pictures of the cross-sectioned coupons (see Figure 4-11 and Figure 4-12) it can be

seen that the position of the core in the model is very similar. However, this is a coincidence and the relative position of the core would have been different for other coupons. In practice no attention is paid to how the insert is placed with respect to the core cells. In theory this will also have an effect on the performance of the insert system, however, this was not investigated in this FE study.

Figure 4-17 shows the constraints that were applied to the model in order to simulate the pull-out test conditions. The nodes corresponding to a circular strip 35 mm in inner radius and 1 element wide were constrained in the out-of-plane direction to simulate the constraint provided by the test fixture. The out-of-plane load applied via the fastener was modeled using a multi-point constraint (MPC). In order to compare the two models with the experimental results a load of 5 kN close to the average static strength capability achieved for both insert coupons was applied in the simulations.

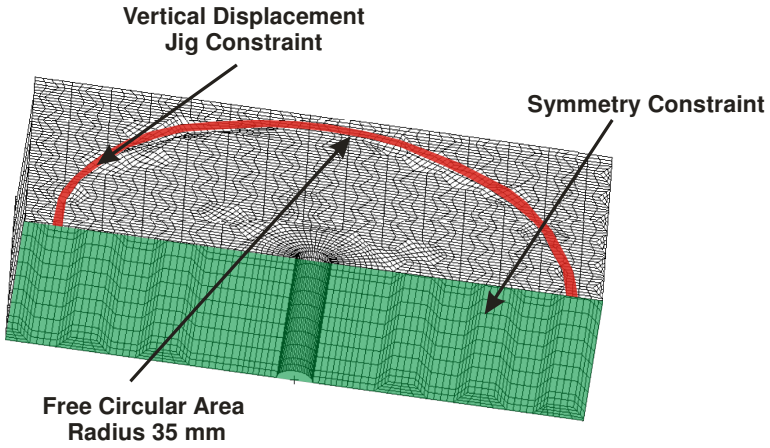

Figure 4-17: Boundary conditions

The material properties entered in the models for the aluminum parts of the coupons are shown in Table 4-4. For the potting compound (Stycast 1090) the manufacturer quotes the elastic modulus as being in the range 2400-2500 MPa.

An elastic modulus for the adhesive foam (Redux 219/2-NA) could not be obtained from the manufacturer so a compressive test on a cylindrical sample was conducted

to measure this property (see Figure 4-18). The test was conducted in displacement control using screw driven Instron 5559 testing machine. The deformation of the sample was accurately measured using an extensometer and an elastic modulus of 1034 MPa was obtained from the test. However, due to the variability of the expansion ratio of the adhesive foam (1:1.19 – 1:1.4), this should only be taken as an indication of the elastic modulus that that may be expected. Empirical data found in Ashby and Gibson [19] suggests that for a foam with a relatively low expansion ratio (< 1:1.6) the following relationship applies

$$\frac{E^*}{E_s} \approx \left(\frac{\rho^*}{\rho_s} \right)^2 \tag{4-9}$$

where E* and Es are the elastic moduli of the foam material in its expanded and solid (unexpanded) state respectively; and ρ*/ρs is the relative density of the foam cell which corresponds to the expansion ratio. The expansion ratio of the adhesive foam cannot be controlled and hence the elastic modulus is likely to vary considerably from case to case depending on how open cells of the honeycomb core are filled. According to Eq. (4-9) the ratio E*/Es can vary from 0.51 to 0.70 for the quoted expansion ratios.

Figure 4-18: Compressive test of Redux 219/2-NA adhesive foam

The elastic modulus of the filler material (potting compound or adhesive foam) plays an important role in determining how the external insert loads are transmitted

to the surrounding sandwich structure. For this reason, and to address the variability in expansion ratio of the adhesive foam, a filler material elastic modulus sensitivity study was conducted for both model geometries. The Stycast 1090 maximum elastic modulus of 2500 MPa was taken as the upper bound of the study and simulations were run in decreasing steps of 500 MPa down to 500 MPa. In both cases the potting compound and the adhesive foam were assumed isotropic with a Poisson's ratio of 0.3 and the shear modulus was obtained using the expression $G = E / 2(1+\upsilon)$.

	Material	Young's Modulus, *E* (MPa)	Poisson's Ratio, υ	Shear Modulus, *G* (MPa)
Face Skins	Al 2014	72400	0.33	27218
Honeycomb Cell Walls	Al 5056	70300	0.33	27038
Bobbin Insert	Al 6082	68300	0.33	25676

Table 4-4: Material properties used in the finite element models for Al-alloy parts

4.9.2 Finite Element Model Results

Since for both coupon types the decisive failure mode was in the honeycomb core the main focus of the sensitivity study was on how the elastic modulus of the filler material affected the stresses generated in the cell walls. Figure 4-19 shows a contour plot of the maximum principal stresses generated in the cell walls of the core obtained for the hot bonded model with an elastic modulus of 2500 MPa entered for the adhesive foam. Apart from the magnitude of the stresses the distribution of the stresses did not vary significantly between the two models or the filler material stiffness. As can be seen in Figure 4-20 the single thickness cell walls closest to the filler material (adhesive foam in this case) are subjected to the highest stress levels. Figure 4-21 (a) and (b) illustrate how the generated maximum principal stresses and shear stresses in the cell walls varied between the hot bonded and cold bonded model and how they were affected by the filler material stiffness.

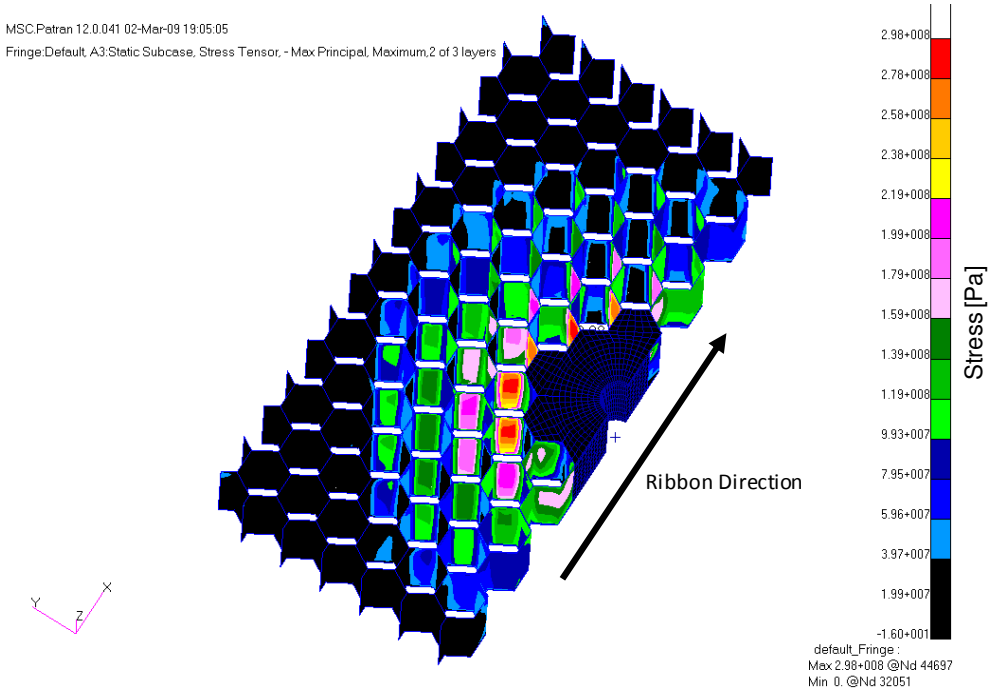

Figure 4-19: Contour plot of maximum principal stresses generated in the cell walls of the core (face skins are hidden)

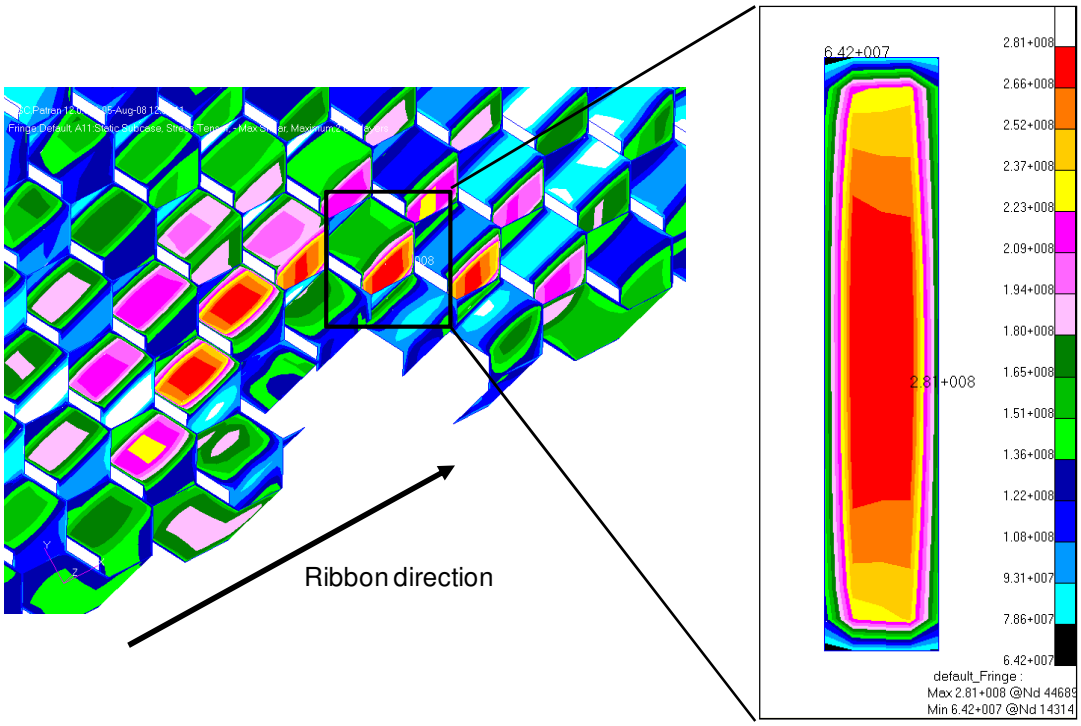

Figure 4-20: Stress distribution over inclined single thickness wall

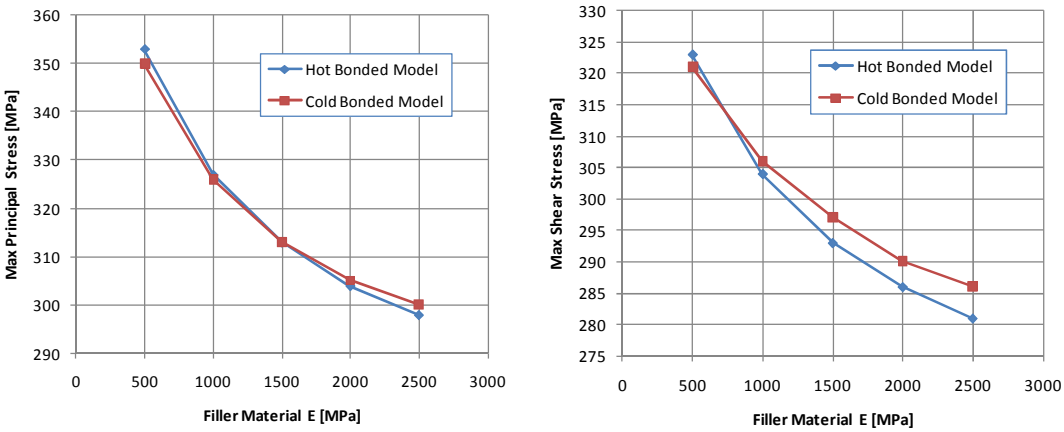

(a) Variation of max principal stress with filler material stiffness

(b) Variation of max shear stress with filler material stiffness

Figure 4-21: Plots showing variation of stresses in cell walls with filler material stiffness for an insert pull-out load of 5 kN

From Figure 4-21 (a) and (b) it can be seen that the variations in maximum principal and shear stress between the hot bonded model and the cold bonded model are small compared to the variations due to changes in filler material stiffness. For values of filler material stiffness above 1000 MPa the results show that for the hot bonded insert geometry the stresses are slightly lower than for the cold bonded insert geometry. However, the results show that the impact of the filler material stiffness is significantly greater with a substantial decrease in stress levels with icreasing stiffness. For both models an increase of almost 10% in maximum principal and maximum shear stresses is obtained when the filler material stiffness decreases from 2500 MPa to 1000 MPa. Assuming a relationship between the magnitude of these stresses and insert failure load then the increase in these stress levels is comparable to the difference in static load carrying capability obtained between the tested hot bonded and cold bonded coupons. The measured elastic modulus for the Redux 219/2-NA adhesive foam was close to 1000 MPa so the

difference in filler material stiffness (even accounting for expansion ratio variation) is probably the main cause of the lower average load carrying capability that was obtained in the experimental results for the hot bonded coupons. This also explains why the analytical model gives a less accurate prediction for the hot bonded inserts compared to the cold bonded inserts. The analytical model assumes that the insert system is a rigid disk which is more representative of a cold bonded insert system which uses a less compliant filler material.

4.9.3 Shear Buckling Instability Calculation

In order to further investigate the failure process in the honeycomb core a formula for the shear buckling strength of thin plates proposed by Roark and Young [65] was applied to the single thickness inclined wall of the core and the results compared with the maximum shear stresses plotted in Figure 4-21. The buckling strength of a single thickness cell wall under uniform shear on all edges (see Figure 4-22) can be expressed as

$$\tau^{cr} = K_{cr} \frac{E}{1-\upsilon}\left(\frac{t}{l}\right)^2 \qquad \textbf{(4-10)}$$

where K_{cr} is a factor that depends on the length to width ratio of the plate and how its constrained, t is the thickness of the cell wall, l is the length of the cell wall, and E and υ are the elastic modulus and the Poisson's ratio. For the dimensions of the cell wall K_{cr} = 4.4 for a simply supported constraint and K_{cr} = 7.38 for a fully clamped constraint. In actual fact the cell wall is neither simply supported nor fully clamped but somewhere in between the two conditions, and hence it is appropriate to calculate the critical shear stress τ^{cr} for both cases. It can be found that for the simply supported case τ^{cr} = 67.9 MPa while for the fully clamped case τ^{cr} = 113.8 MPa. Both of these values are significantly lower than the maximum shear stress values plotted in Figure 4-21 (b). Considering that the finite element shear stress values were calculated for a pull-out insert load close but below the maximum achieved in the experiments, it follows that the single thickness cell walls operate in a post-buckling regime when the insert system is subjected to high loads.

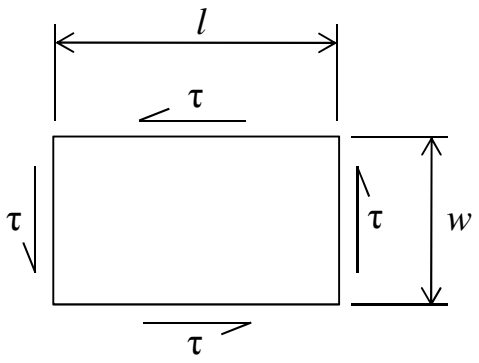

Figure 4-22: Rectangular plate under uniform shear on all edges

4.10 Conclusions

A study on hot bonded inserts has been conducted to assess their performance and compare them with cold bonded inserts. Contrary to what was expected the experimental results showed that the cold bonded fully potted inserts outperformed the hot bonded inserts in terms of static strength capability. However, as expected, in both cases failure initiates in the honeycomb core by shear buckling of the cell walls. The results from the finite element study showed that the unexpectedly lower performance of the hot bonded inserts can be attributed to the stiffness of the filler material. The adhesive foam used as the filler material for the hot bonded inserts has a sensibly lower stiffness than the potting compound used in the cold bonded inserts and hence is less effective at transmitting external insert loads to the surrounding honeycomb core in an even manner. For equal filler material stiffness the finite element results showed that the hot bonded insert design performs slightly better than the cold bonded fully potted design.

The comparison of results from buckling theory on thin plates subject to uniform shear loads with the results obtained from the finite element model shows that when the insert is subject to high loads the inclined single thickness cell walls operate in a post-buckling regime from which recovery is still possible once the load is removed.

An analytical model proposed in the IDH was also applied to the tested insert systems and a good correlation was found with the experimental cold bonded insert results. However, due to its simplifying assumptions the model cannot distinguish between the hot bonded and the fully potted cold bonded design.

Chapter 5

5 Bolted Joints between Honeycomb Panels

5.1 Introduction

Bolted joints are the preferred choice when connecting honeycomb panels to form spacecraft assemblies. At SSTL bolted joints are extensively used to connect the panels of the spacecraft they produce. A recent example of this can be seen in Figure 5-1 which shows the structural qualification model (SQM) of NigeriaSat-2 which consists of an assembly of honeycomb panels joined by numerous bolted joints. Bolted joints exhibit many advantages e.g. ease of assembly, reassemblage, repairing of damaged structural parts, and can contribute to structural damping. Because of the weakness of the core, honeycomb sandwich structures are not suited to carrying point or line loads. A local reinforcement of the core, usually in the form of one or more metallic inserts, is thus required at the panel edge where the joint is to be established. This feature adds a degree of complexity to these type of bolted joints compared to conventional ones. One of the disadvantages in using bolted joints and mechanical fastenings in general is that they add more mass than other attachment methods such as welds or adhesive bonds [2]. In a spacecraft where the primary structure consists of an assembly of honeycomb panels, bolted joints can represent a significant proportion of the mass of the structural subsystem. Considerable mass savings can thus be gained by increasing the efficiency of bolted connections in terms of load carrying capability per unit mass.

The topic of bolted joint optimization is not new and has been covered in several other works. However in most cases (e.g. [66-68]) the focus is always on a specific joint problem and a numerical approach (e.g. the genetic algorithm) is normally used to find an optimum solution. In this work the scope was wider and rather than providing an optimization tool for a particular joint problem the aim is to provide

logical procedures, and numerical and experimental data which can be used to find efficient and effective joint solutions to a variety of honeycomb panel joint problems.

The development of efficient and reliable bolted joints between honeycomb panels involves the following challenges: (i) choice of optimum joint configuration in terms of number, size and distribution of bolts (ii) prediction of the stresses generated in the various joint components by the combined action of externally applied loads and the clamping pressure from bolt preload (iii) estimation of the friction coefficient between the faying surfaces of the joint.

Many works have been published on the topic of bolted joints and the European Space Agency (ESA) has also produced a manual [69] which specifically covers bolted connections for spacecraft applications, however, there are no works which specifically focus on bolted joint connections between honeycomb panels.

The aim of this work is to explore and address the main issues that arise when designing such joints, particularly when considering spacecraft applications.

The bolted joints that hold the spacecraft structure together are subjected to high loads during the launch phase of the mission. The joints should provide sufficient strength and stiffness under such loads. Predicting bolt loads and joint strength is rarely straightforward and often, to compensate for this, very conservative assumptions are made when designing the structure. In a spacecraft where the primary structure consists of an assembly of honeycomb panels this can lead to an over-designed and unnecessarily heavy structure. This means that there is significant room for improvement in terms of structural mass efficiency. Gaining greater confidence during design is also another important motivation for studying these bolted joints.

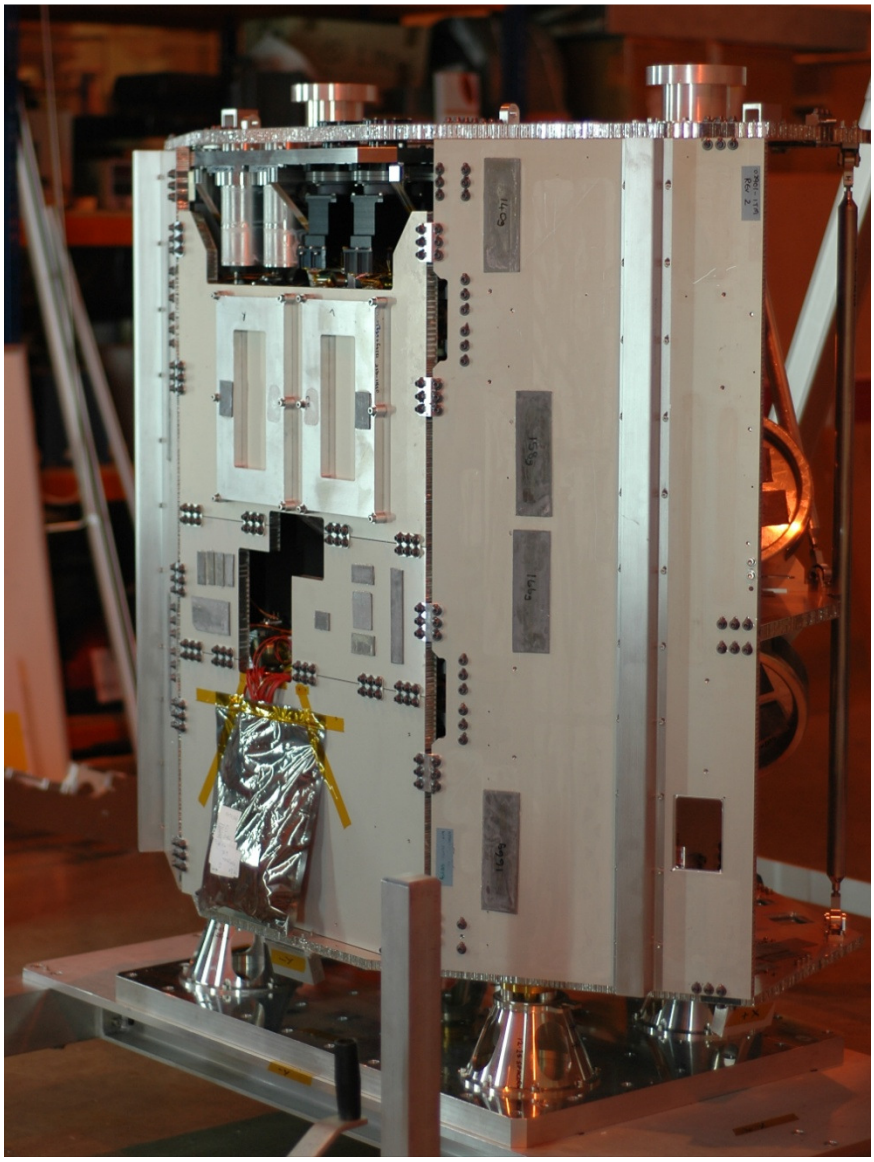

Figure 5-1: SQM of NigeriaSat-2

5.1.1 Types of Joints

The three main configurations in which honeycomb panels are normally connected are: in-plane joints, 'T' joints and corner joints (see Figure 5-2 - Figure 5-4). In-plane joints predominantly operate as shear joints, where the loads are transmitted in the transverse direction to the longitudinal axis of the bolts. However, shear joint operation also plays a very significant role in all the other joint configurations. In the "T" joint illustrated in Figure 5-4 it can be seen that bobbin inserts are used to

resist out-of-plane loads in a similar manner to equipment inserts. Hence, research work that is being carried out on equipment inserts is also useful for "T" joint applications. Bending loads will also be present but these will mostly concern the connection plates rather than the relationship between bolt load and joint strength.

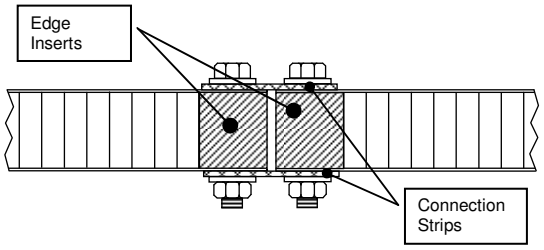

Figure 5-2: In-plane Joint

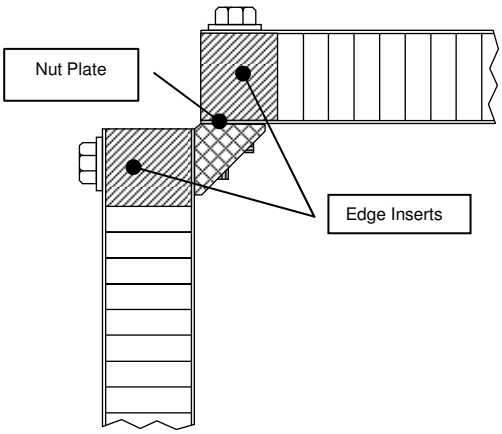

Figure 5-3: Corner Joint

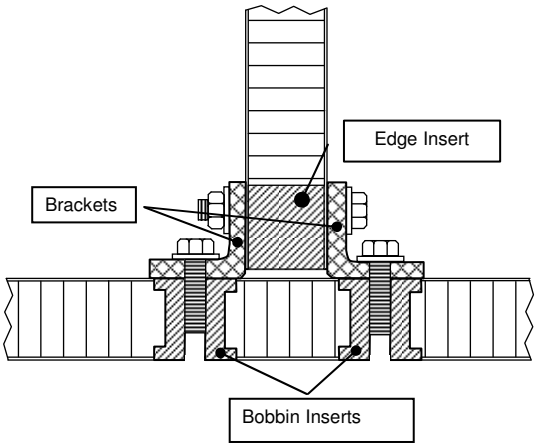

Figure 5-4: "T" Joint

5.1.2 Shear Joints

The term shear joint is used to describe joints in which the loads are transmitted in the transverse direction to the longitudinal axis of the bolt (see Figure 5-5). Such joints can be designed according to two fundamentally different philosophies:

a) Friction grip or slip resistant design

b) Bearing type or slipped joint design

A friction grip joint design relies on a sufficiently high clamping force to prevent slippage of the clamped joint parts due to external (transverse) loading, F_Q. In many industries the friction grip option is taken for the following reasons. Provided that slip does not occur the bolt only feels tensile load due to preload. Furthermore the high bolt preload required to produce the necessary clamping force means that the bolt only feels a small portion of externally applied tensile loads, which can greatly increase fatigue resistance. Another advantage is that large clearance holes can be used which facilitates assembly and interchangability. For these reasons the bolted joints considered in this work are designed according to the friction grip philosophy.

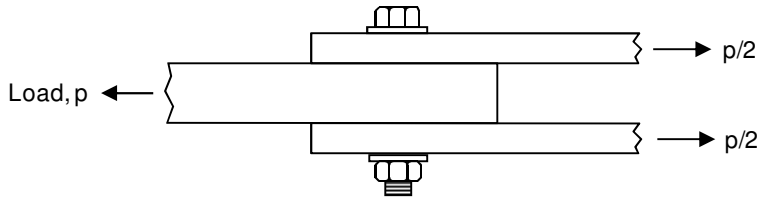

Figure 5-5: Example of a double shear joint

A bearing joint is one in which the clamped parts have slipped until the bolts "bear" the clearance holes. Bolts in this type of joint configuration are subjected to a combination of axial and shear stresses. Because the factors of safety used in the space industry are not as high as the ones used in other industries the uncertainty of friction as a load path poses greater risks [69]. Although, for the reasons described above, bolts should be preloaded to achieve friction grip conditions it is also important to ensure that the joint also has enough strength to work in bearing mode in case of slip. This is why bearing performance was also investigated for the joints considered in this work (this is covered in chapter 8).

5.1.3 Slip Resistance and Bolt Preload

In order to obtain a friction grip joint the slip resistance, S_r, must be higher than the externally applied shear load, F_Q. Slip resistance depends on the friction force between the faying surfaces of the joined parts. A relationship between slip resistance and bolt preload can be easily derived by Amontons' first friction law [8] which states that the friction force between a pair of sliding surfaces is proportional to normal load by the coefficient of friction, μ. Hence, provided that all the bolts are equally loaded, the Slip resistance can be defined by the expression

$$S_r = \mu_S \times m \times F_M \times n \quad \textbf{(5-1)}$$

where μ_S is the friction coefficient between the faying surfaces known as the "slip coefficient", m is the number of bolts, F_M is the preload in each bolt and n is the number of faying surfaces. It is interesting to note that, as stated in Amontons' second friction law, the friction force does not depend on the apparent contact area between the surfaces. This is because faying surfaces have atomically close contacts only over an extremely small fraction of their overall surface area, and this contact area is proportional to load.

It follows from Equation 5-1 that the minimum value of required preload $F_M = F_{Kreq}$ is given by

$$F_{Kreq} = \frac{S_r}{\mu_S \times m \times n} \quad \textbf{(5-2)}$$

where $S_r = F_Q$ the total shear load.

Friction is subject to high variability so it is important to use conservative values for μ_S to ensure safety in design calculations. Finding F_{Kreq} through Equation 5-2 represents the first step in selecting a bolt for a friction grip joint.

5.1.4 Torque-tension Relationship

Maintaining the correct bolt preload is critical in ensuring the integrity of a bolted joint. It has been shown that optimum joint design depends on obtaining the maximum possible preload. The most common causes of failure in bolted joints are incorrect preload and loss of preload due to self-loosening. Therefore, there is a need to accurately control the level of preload to a specified value. However, measuring preload in a bolt is not easy. A variety of methods exist for controlling and achieving preload during assembly. Amongst these the main ones are the following: torque controlled tightening, yield load controlled tightening [69], and angle of rotation controlled tightening [69,70]. The torque tightening method uses the relationship between torque and induced preload in the bolt. Yield controlled tightening are based on the notion that that when yield is reached, the tightening torque ceases to increase linearly with the angle of rotation. Angle of rotation controlled tightening relies on using the nut (or bolt) angle of rotation as an indirect way of measuring elongation. Out of these the most widely used method is torque tightening. Although this is not a very accurate method of achieving preload it is convenient and relatively inexpensive. A more accurate way of achieving preload is by directly measuring elongation with a strain gage [71]. This is not a very practical solution final use assemblies, however, the technique can be very useful for experimental applications. In Wang [7] the strain gage technique was used to accurately measure preload in bolted joints which were subjected to static and cyclic testing.

The torque-tension relationship has been extensively investigated. The tribological properties of the bolt, nut and joint bearing surface play a key role in the torque-tension relationship. Most of the torque required to tighten a bolt is used to overcome two frictional torque components. The first frictional torque component is caused by the friction between the bearing surfaces and the turning fastener head or nut. The second frictional torque component is caused by the thread friction.

Only the remaining torque produces the bolt preload which provides the joint clamping force.

A commonly used expression for the torque-tension relationship is

$$T = \left(\frac{p}{2\pi} + \frac{\mu_t r_t}{\cos\alpha} + \mu_b r_b \right) F_M \qquad \textbf{(5-3)}$$

where T is the input torque applied, F_M is the applied tension (i.e. bolt preload), p is the thread pitch, μ_t is the thread friction coefficient, μ_b is the friction coefficient between the bearing surfaces and the head or nut, r_t is the effective contact radius between threads, r_b is the effective bearing radius of the bearing contact area under the head or nut, and α is half angle of the thread profile angle which is 30° for standard UN and ISO threads. Equation 5-3 may be expressed as

$$T = T_p + T_t + T_b \qquad \textbf{(5-4)}$$

where T_p is the pitch torque component that directly contributes to the bolt preload F_M. The pitch torque component is given by

$$T_p = \frac{p}{2\pi} F_M \qquad \textbf{(5-5)}$$

Tt is the torque component required to overcome thread friction and is given by

$$T_t = \frac{\mu_t r_t}{\cos\alpha} F_M \qquad \textbf{(5-6)}$$

and T_b is the bearing friction torque component that is necessary to overcome the friction between the turning fastener head and the clamped joint surfaces, and is given by

$$T_b = \mu_b r_b F_M \qquad \textbf{(5-7)}$$

A more compact way of expressing the torque-tension relationship is

$$T = K_T D F_M \tag{5-8}$$

where D is the nominal diameter of the bolt and K_T is the torque coefficient.

Experimental studies on the torque-tension relationship have been presented in several works (e.g. [72,73]). In these papers special experimental set-ups are used to measure μ_t, μ_b and K_T. Figure 5-6 and Figure 5-7 have been taken from the work presented in Jiang et al [72]. Figure 5-6 shows that that the torque-tension relationship is non-linear. This non-linearity is mainly due to the non-linear behavior of the frictional torque component associated with μ_b (i.e. the last part of Equation 5-3). Figure 5-7 shows that that K_T varies after repeated tightening/loosening cycles and is influenced by the material of the bearing surfaces (i.e. washer material). For steel the K_T value is almost constant whereas for aluminium there is a marked increase after a certain number of cycles. Furthermore it was noted that the scatter in friction data generally overshadows the influence of size, speed, and contact positions.

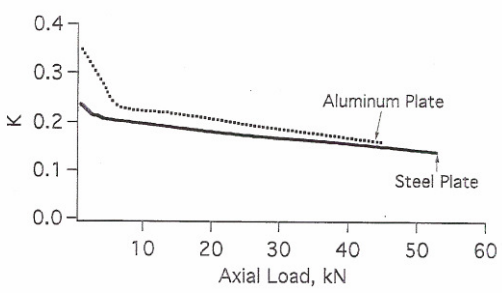

Figure 5-6: The variation of K with axial load [72]

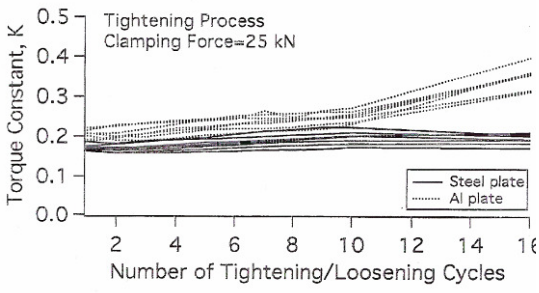

Figure 5-7: Variation of K with tightening cycles [72]

When using Equation 5-3 the effective bearing radius r_b is often assumed to be equal to the geometric mean r_m of contact ring between the bolt head and the bearing surface. However, in Nassar et al [73] it is shown that this assumption can lead to a significant error in the estimation of the bearing friction torque

component. The error becomes more noticeable in applications where the ratio of the maximum to minimum radii of the underhead contact areas is large (e.g. a flanged head fastener).

5.1.5 Measurement of Friction

From sections 5.1.3 and 5.1.4 it is evident that friction plays an important role in the design calculations of friction grip joints. Despite the best efforts of tribology experts, currently, there is no foolproof method of establishing friction coefficient values between two surfaces from the knowledge of their individual material properties and their local surface topographies. Hence, the designer has to rely on experimental data. However, the friction coefficient between two surfaces is highly sensitive to slight variations in surface conditions. Because of this, great care must be taken when using other people's experimental results, since even a marginal difference in the experimental conditions can yield very different results. The following example [74] illustrates the problem very well. A brass block sliding on a steel plate in ordinary atmospheric conditions without any particular care taken to clean the faying surfaces will produce a μ value of around 0.5. If the experiment is repeated with very clean surfaces (which may happen, for example, in a high vacuum or space environment) the friction coefficient will be much greater, possibly reaching 10 or even more. In many cases the only way of truly achieving peace of mind is to conduct tests on the actual materials intended to be used under the same conditions that are going to be encountered in practice. Because the fiction coefficients μ_S, μ_b and μ_t have such an impact on the bolt preload calculations it will probably be necessary to conduct friction measurements during this project. The experimental techniques designed to do this are thus reviewed.

Test set-ups designed to measure frictional interactions are characterized by a means of applying a known normal load between the two test surfaces which simultaneously carry a measurable tangential force; it must be possible to increase this force until relative motion occurs. Many techniques have been developed to measure friction. The simplest method is the inclined plane test (see Figure 5-8) in

which one material is in the form of a flat plate on which rests a block of the second. The static friction coefficient is then given by

$$\mu = \tan f \tag{5-9}$$

where f is the angle of inclination with respect to the horizontal at which slip starts.

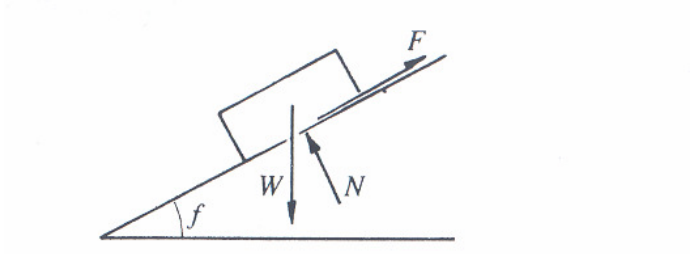

Figure 5-8: Inclined plate friction test [74]

One of the most common techniques for measuring friction is based on the pin-on-disc arrangement (see Figure 5-9 (a)). A pin is held stationary over a rotating disc, so that any point on the resulting wear track comes into contact with the pin over and over again. The test is thus conducted under multiple-pass conditions. A more complicated set-up is required to produce single-pass conditions. To do so the pin may be arranged to move radially so that it continuously comes in contact with fresh surface; however the drive speed of the disc must also be varied if a steady sliding speed is to be maintained. Variations on this standard arrangement are the pin-on-cylinder and crossed-cylinders arrangements illustrated in Figure 5-9 (a) and (b).

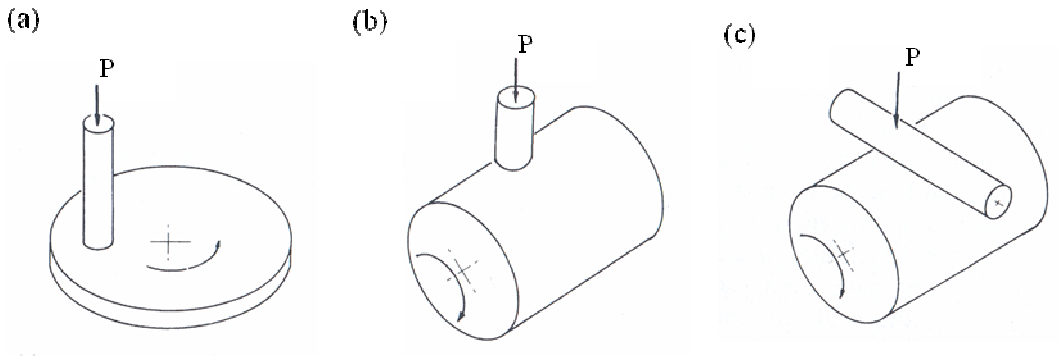

Figure 5-9: Friction measurement solutions [18]

The above techniques are not applicable for measuring the bolt friction coefficients μ_b and μ_t. In Jiang et al [72,75] a tension-torsion servohydraulic testing machine is used to measure the thread friction coefficient. Using a special test fixture (see Figure 5-10) the head of the bolt is turned while a linearly increasing axial force is applied; to ensure that $\mu_b = 0$ the head is not in contact with any other surfaces. The twist angle increases linearly with the linear load so that the action between the threads is identical to the conditions of tightening a bolted joint. The measured torque is equal to the torque required to overcome thread friction, T_t, and the pitch torque, T_p. Since $\mu_b = 0$ there is no bearing torque component (i.e. $T_b = 0$) and by knowing the applied axial force F the thread friction coefficient μ_t is be easily found by combining Equations 5-5 and 5-6. A very similar technique is used in Nassar et al [73].

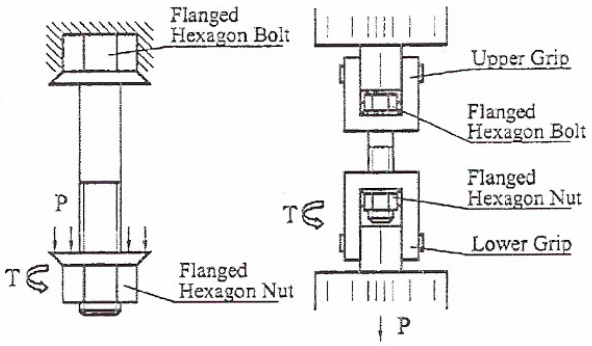

Figure 5-10: Experimental set-up used to determine thread friction [72]

In Jiang et al [72,75] the bearing friction coefficient μ_b is found by turning a bolt head against a plate surface while a known axial compressive force F_M is applied. With no threads engaged the measured reaction torque is equal to T_b. The corresponding friction coefficient is easily determined through Equation 5-7. In Nassar et al [73] the bearing friction coefficient μ_b determined via the inclined plane test (see Figure 5-11).

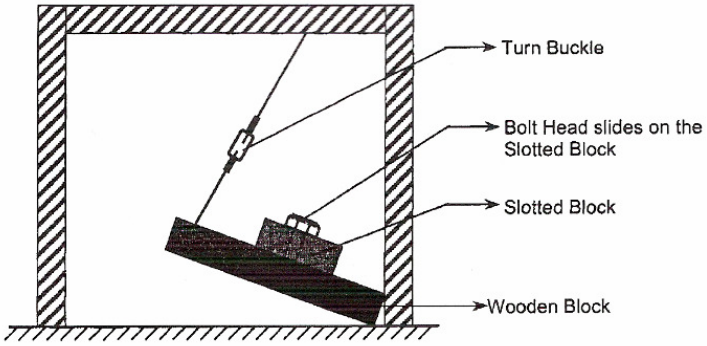

Figure 5-11: Inclined plane test applied to a bolt head [73]

In Wang [7] the slip coefficient μ_S between the clamped surfaces of a double (friction grip) shear joint was determined by conducting a tensile test of the joint. By recording the load at which slip occurred and with an accurate knowledge of the applied bolt preloads the slip coefficient was determined via Equation 5-2.

5.2 Friction Theory Literature Review

5.2.1 Friction Theory Relevant to Bolted Joints

The surface phenomena at the basis of frictional behaviour between two surfaces are so numerous that gross assumptions leading to different tribological theories have been made to describe frictional traction in the past. Currently, the friction of two flat metals in relative tangent motion appears to be dominated by shearing of asperities, adhesion of asperities, ploughing by asperities, and ploughing by wear particles.

Much experimental work has been carried out since the beginning of the 1930's and numerous theories have been proposed in an effort to explain friction mechanism. Although, most of this work was done by considering geometries and pressure distributions which have little resemblance to bolted joints some of the conclusions obtained are still applicable and of interest when looking at the frictional behaviour of bolted joints. The friction between two rigid bodies is related to contact mechanics an area in which many notable works have been published a selection of which is given here in [76-82]. In Groper [83] the more relevant conclusions to describe the frictional behaviour of bolted joints are summarized as follows.

The friction coefficient changes significantly during sliding. At the onset of slip the friction coefficient starts from a low value and then increases with relative slip until a maximum value is reached. This maximum remains approximately constant when the two sliding parts are made of the same material and have similar surface topography. The increase in friction coefficient after slip onset is due to the contribution of plowing by particles generated by asperities shearing and by wear. Adhesion also contributes to the increase in friction coefficient after the onset of slip. Adhesion of asperities occurs after the initiation of slip when the contaminated/oxidized contacts are sheared off and previously unexposed material comes into contact with the mating surface. The coefficient of friction reaches a

maximum value when the adhesion contribution levels off, and the number of wear particles stabilizes.

Contrary to the classical Coulomb's laws of friction the coefficient of friction usually decreases with an increasing contact pressure. One of the first observations of this behaviour was made by Paslay and Plunkett [84] with their experimental work on shrink-fits. This trend appears to be more pronounced for rough surfaces. In Nolle and Richardson [85] it is suggested that this reduction in friction is caused by the fact that the material asperities plastically fail under compression.

Due to the complexity of friction phenomena the theoretical analysis methods currently available yield friction coefficient results which are not always in good agreement with experimental predictions. Finding the friction coefficient for bolted joints is even more challenging since additional factors must also be taken into account: variation of clamping pressure with distance away from the bolt hole, loss of bolt preload with time, regions of micro-slip and non-slip, variation of friction coefficient with pressure distribution, etc. Because of this, friction data obtained from bolted joint experiments is not always in good agreement with the data from experiments conducted with the same material specimens tested in more conventional configurations under different contact pressure distribution.

If some of the above mentioned additional factors are taken into account, a more accurate expression can be derived to calculate the slip load or friction load. In Groper [83] the slip load is defined as the tangential load which produces micro-slip in an annulus region between x and x_0.

$$F(x) = mn\int_A \mu_x p_x dA = 2\pi mn\int_x^{x_0} x\mu_x p_x dx \qquad \textbf{(5-10)}$$

According to many authors [86-89] p_x decreases linearly with radial distance. However, due to the reasons stated above the determination of μ_x is more complicated. As mentioned above the friction coefficient decreases with increasing contact pressure so μ_x will have a maximum value at the boundary between the no-slip and partial slip regions. For simplicity a linear decrease with radial distance can be assumed for μ_x. A more realistic approach is to use experimental data for the surfaces of interest from which a numerical solution can be obtained.

5.2.2 Friction Coefficient in Bolted Joints

Despite their widespread use not many works have been published on the frictional properties of bolted joints. Moreover, many of these works [90,90-92] are more focused on the damping contribution from the frictional behaviour of the joint. Another large portion of these works [85,93-96] are in the field of civil engineering and are concerned with large scale steel structures (eg. bridges, transmission towers, etc.). The paper by Baylis [97] presents the most relevant work. The paper reports on an experimental programme that was carried out to generate slip coefficient data, representative of spacecraft structures, for inclusion in the ESA Guideline on threaded fasteners [69]. The main details and findings from this experimental campaign are presented in what follows. The variables investigated were material and loading type (static and dynamic). Materials tested were: Ti, Al, Glass Reinforced Plastic (GRP), and Carbon Fibre Reinforced Plastic (CFRP). For Al both Alochromed and Anodised coatings were tested. The results obtained from the campaign are summarized in Figure 5-12 and Figure 5-13. The results include the mean value, $\pm 3\ \sigma_{n-1}$ for the samples tested and the coefficient of variation. The type of loading did not have a significant effect on the slip coefficient, with the exception of alochromed surfaces, which showed a marked increase in friction coefficient when dynamically loaded. However, out of all the tests carried out the friction coefficient was always higher for samples which were subject to a combination of dynamic and static loads indicating that using static data is conservative and more appropriate for design purposes. Preload also did not have a

significant effect on the slip coefficient. Reuse of slipped joints was found to reduce the friction coefficient. Out of the materials/surface coatings used anodised Al on anodised Al gave the lowest values of slip coefficient. Ti on Ti and Ti on anodised Al were also relatively low. Ti on alochromed Al and Ti on untreated Al gave higher values of friction coefficient. The highest value was obtained for alochromed Al on anodised Al (~0.75 average).

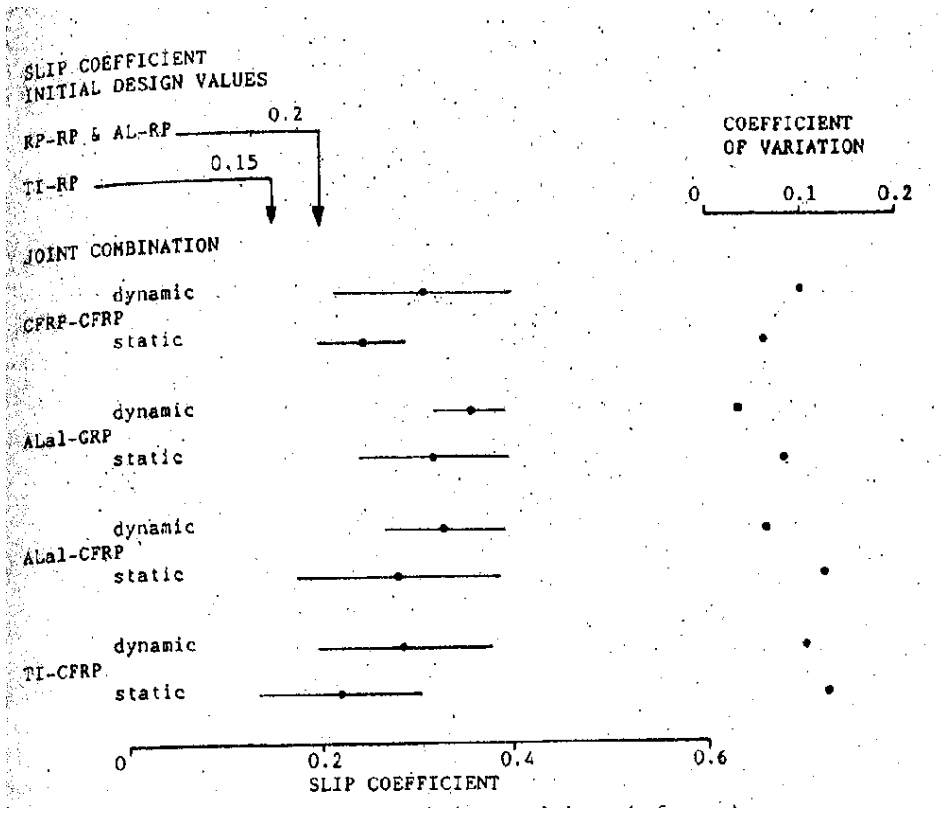

Figure 5-12: Composite surfaces friction coefficient results from Baylis [97]

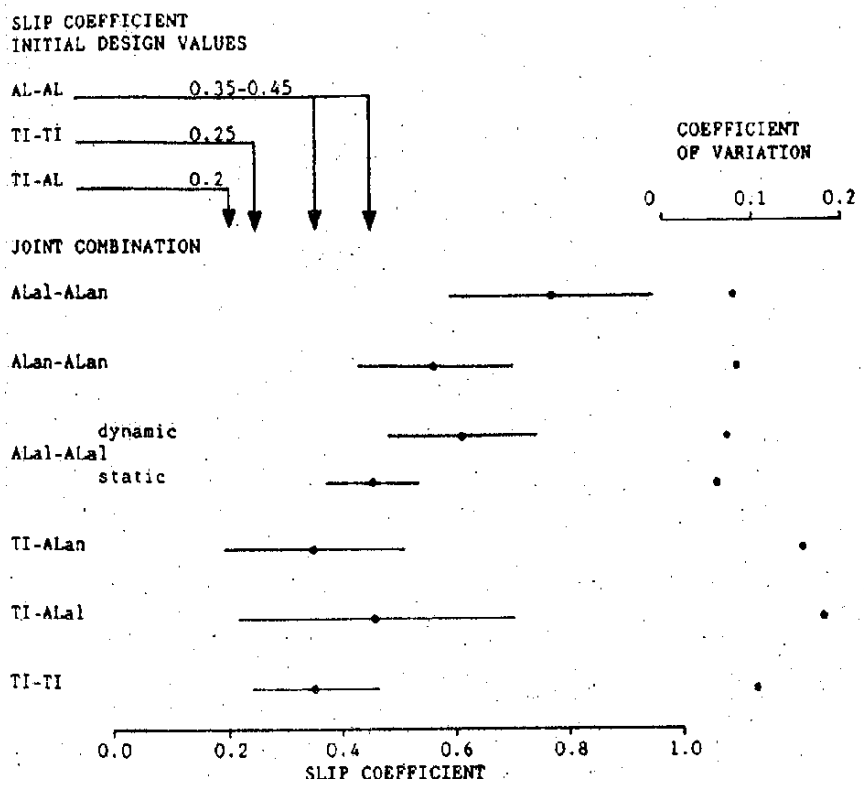

Figure 5-13: Metal surfaces friction coefficient results from Baylis [97]

5.2.3 Methods of Improving the Performance of Friction Grip Joints

It is clear from section 5.1.3 that one of the main ways of improving the performance of friction grip joints is to increase the friction coefficient. An alternative solution is to use interlocking geometries (see Figure 5-14). This is a very effective solution however it has the disadvantage of making assemblage more complex since tight tolerances are required.

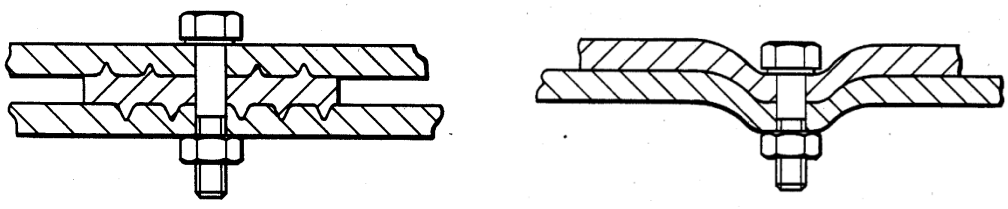

(a) Toothed washer joint (b) Joggle joint

Figure 5-14: Slip resistant joints [69]

Surface abrasion is probably the most effective way of increasing the friction coefficient between two surfaces but has the disadvantage of greater fastener preload loss due to embedding [69]. Although there are numerous works on the effect of surface abrasion on friction coefficient between rigid bodies in contact [98-105] no literature could be found on specific studies carried out for friction grip joints. Many of these works are theoretical [98,100-105] and propose various models to describe the friction behavior of rough surfaces in contact. Most of these models are based on modeling the contact behavior of a single spherical asperity, which is then incorporated in a statistical model to simulate multiple asperity contact. This approach was first proposed by Greenwood and Williamson [101] and their elastic contact model (GW model) remains one of the most important theoretical frameworks for understanding fundamental contact mechanics. The model was experimentally verified by Handzel *et al.* [102] and has been progressively improved by incorporating new concepts and assumptions to develop more general and robust contact models [98,100,103,104]. Chang *et al.* [98,100] expanded on the GW model by incorporating elastic-plastic contact in their CEB model. In turn the CEB model was further improved by Kogut and Etsion [104] with their KE model by accounting for the resistance to sliding of plastically deformed asperities. Various experimental works have been carried out to verify these models and overall their predictions have been found to be good, however, research efforts are still ongoing to generalize them further and extend their range of applicability.

5.2.3.1 Key Parameters affecting the Friction Coefficient

One of the main conclusions that emerges from the above contact models is that the main surface parameters affecting the friction coefficient are:

- plasticity index Ψ
- adhesion parameter η

The plasticity index Ψ is a dimensionless parameter first suggested by Greenwood and Williamson [101] an is expressed by

$$\Psi = \frac{2E}{\pi KH}\left(\frac{\sigma_s}{R}\right)^{1/2} \quad \textbf{(5-11)}$$

where σ_s is the standard deviation of asperity heights, *K* is the hardness coefficient, *H* is the surface hardness, and *R* is the asperity radius of curvature. *E* is the Hertz elastic modulus defined as

$$\frac{1}{E} = \frac{1-\upsilon_1^2}{E_1} + \frac{1-\upsilon_2^2}{E_2} \quad \textbf{(5-12)}$$

where $E_{1,2}$ are the elastic moduli and $\upsilon_{1,2}$ are the Poisson's ratios of the contacting surfaces. The plasticity index Ψ is a measure of the intensity of plastic deformation of the contact between the mating surfaces. Rough surfaces and soft materials have high Ψ values and the contact is mostly plastic. The contact is largely elastic if $\Psi << 1$, and a significant number of asperity contacts are plastic when $\Psi \sim 1$. From the above cited models it is found that contact pairs with high plasticity index give low values of friction coefficient. This result implies that unless the surface hardness is very high increasing surface roughness can result in a substantial decrease in friction coefficient.

The adhesion parameter is the second important parameter which was first suggested by Fuller and Tabor [106] as

$$\eta = \frac{E\sigma_S}{\Delta\gamma}\left(\frac{\sigma_S}{R}\right)^{1/2} \quad \textbf{(5-13)}$$

where $\Delta\gamma$ is the change in surface energy defined as

$$\Delta\gamma = \gamma_1 + \gamma_2 - \gamma_{12} \quad \textbf{(5-14)}$$

γ_1 and γ_2 are the surface energies of adhesion of the two surfaces before contact, and γ_{12} is the surface energy of the interface between them after contact. For a given external force the friction coefficient increases as surface energy increases. However, in Kogut and Etsion [104] it was found that the effect of the adhesion parameter was negligible for high plasticity index values. At plasticity index values below 1 the effect of the adhesion parameter can be significant if $\eta > 0.001$ and if the external force is not too large. Figure 5-15 shows the effect of plasticity index and adhesion parameter on the friction coefficient.

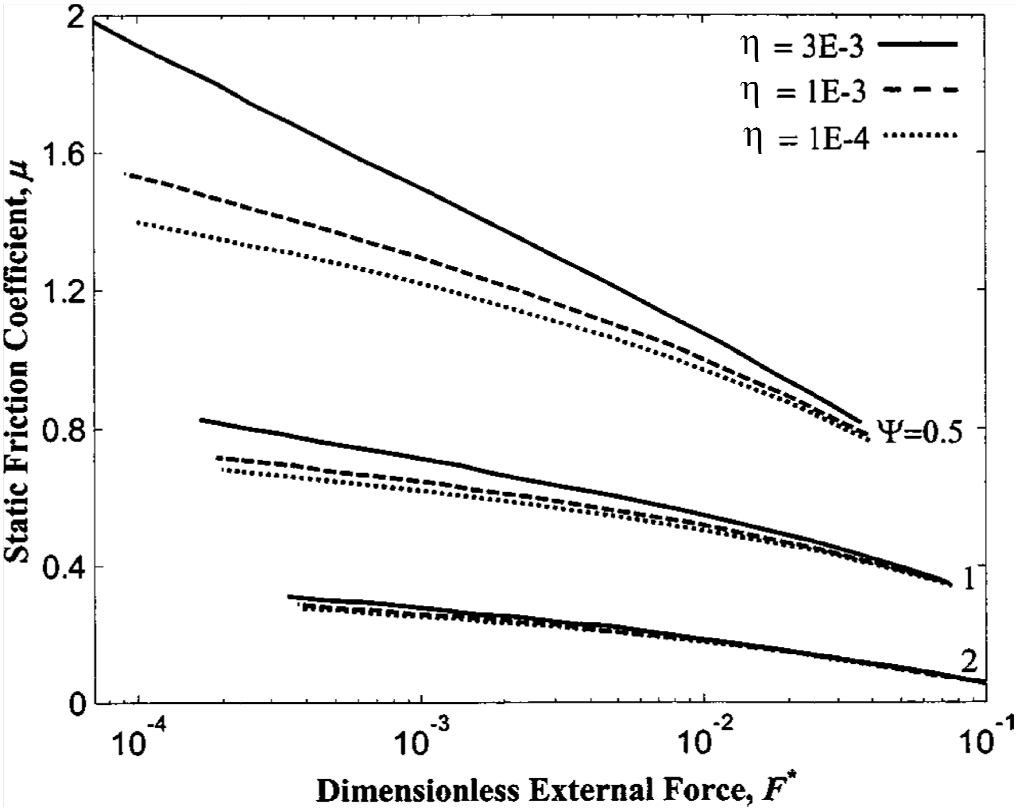

Figure 5-15: Friction coefficient versus dimensionless external force for various values of plasticity index and adhesion parameter [104]

Another conclusion that emerges from these models is that the friction coefficient is not independent from normal load. As can be seen in Figure 5-15 in [104] the friction coefficient reduces significantly with increasing external force.

In Blau [77] it is suggested that for dry friction the initial surface texture of two contacting materials can only influence the friction if: (i) the contact pressure is small enough to avoid loss of original geometry, (ii) the surface microgeometry has characteristics that enable it to trap loose particles that would otherwise affect friction. Point (i) is in agreement what has been found in the theoretical works described above and also with what Nolle and Richardson [85] suggest regarding the reduction of friction coefficient with increasing contact pressure (see Section 5.2).

5.2.3.2 Surface Texture

A key factor to keep into consideration, when considering surface roughness to increase friction, is surface texture. Surfaces with nominally similar surface roughness characteristics can have significantly different surface textures and hence frictional properties. From the literature there are many roughness parameters available [107]. However, these are normally just single roughness property parameters such as the commonly used R_a which describes average roughness. Such single parameters are not sufficient to accurately describe the details of a 3D surface texture [108]. In Menezes *et. al.* [109] a test campaign was carried out to show how roughness and surface texture affected friction. Tribological pairs consisting of high purity aluminium pin against steel plate were used in the tests. From these tests it was found that the friction coefficient was controlled by surface texture and was largely independent of average surface roughness (R_a). The various roughness parameters listed in [107] where correlated with the obtained data and the parameter describing the mean slope of the profile was found have the highest correlation. A series of hybrid parameters with even higher correlation were also proposed.

5.2.3.3 Alternative methods for increasing the friction coefficient

Another way of increasing the friction coefficient is to use optimum combinations of materials or surface coatings. From Baylis [97] it appears that materials with

harder surfaces combined with materials with moderately softer surfaces give higher values of friction coefficient (e.g. anodised Al on alochromed Al, or Ti on alochromed Al). This also seems to be in agreement with the suggestions given by Blau [77].

A further method of increasing the friction coefficient is to use specifically tailored surface coatings. In Koike [93] an inorganic Zinc-rich paint was developed to increase the slip factor in high strength friction grip (HSFG) joints between steel members for bridge applications. An increase in friction coefficient from ~0.4 to ~0.7 was achieved using this method. The effect of surface coatings on slip coefficients is also experimentally investigated in Frank [110]. Here it was found that many variables influence the performance of the coating and that to determine the resulting friction coefficient tests need to be carried out for each particular type of coating. The testing method used is presented in Yura and Frank [111].

In Luscher [112] a method is proposed to increase the friction coefficient in bolted joints were anaerobic sealants are used in the abutment region. A typical example of this arrangement can be found in the bolted joints between the flanges of large vehicle axles. Here the method proposed was to add grit into the anaerobic sealant to provide a locking effect between the two surfaces and increase the friction by ploughing of the hard grit particles (see Figure 5-16).

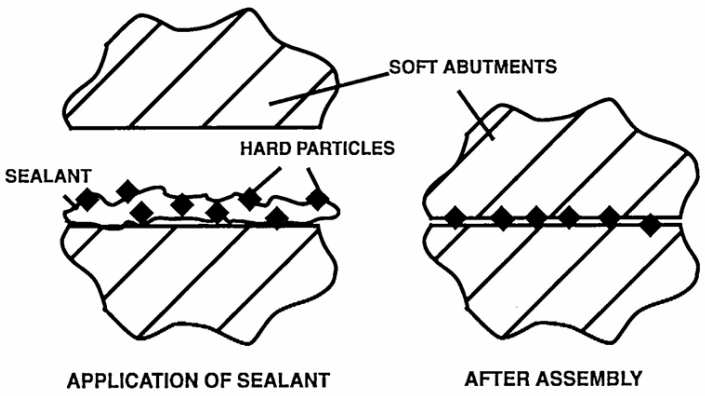

Figure 5-16: Particle enhanced sealant concept [112]

5.2.4 Friction Literature Summary

The joint friction work that was carried out for this thesis was mainly experimental and no analytical models were used to predict frictional behaviors. However, the literature covered above provides useful background for the experimental work presented in Chapter 6. Moreover, the material reviewed was used to help in deciding the joint configurations tested and interpret the results obtained. The following are some of the key points that can be taken from the review presented above:

- The coefficient of friction decreases with increasing contact pressure.
- Clamping pressure varies with distance away from the bolt.
  - The friction coefficient also varies with distance away from the bolt.
- Static friction coefficient values are usually lower than dynamic friction coefficient values for equivalent surfaces.
  - Static tests provide conservative data.
- There are two key parameters which affect the friction coefficient
  1. Plasticity index Ψ
  2. Adhesion parameter η
- Surfaces with low plasticity index and high adhesion parameter values give high values of friction coefficient
- Increasing surface roughness can be an effective way of increasing friction coefficient by ploughing and shearing of asperities. However, increasing the surface roughness also increases the plasticity index.
- Single roughness parameters such as R_a are not sufficient to describe surface texture. Multiple roughness parameters need to be measured to accurately describe the tribological properties of a surface.

5.3 Joint Distribution

Generally, rather than a continuous joint line, the joint design will consist of discrete joint units distributed along the joint line (see Figure 5-17). As well as

transmitting loads the joint system must also provide an adequate level of stiffness. This can be largely controlled by the number and distribution of joint units. The joint design process may thus be approached by first defining the number and distribution of joint units on the basis of stiffness requirements and then optimizing the single joint units on the basis of the predicted maximum loads.

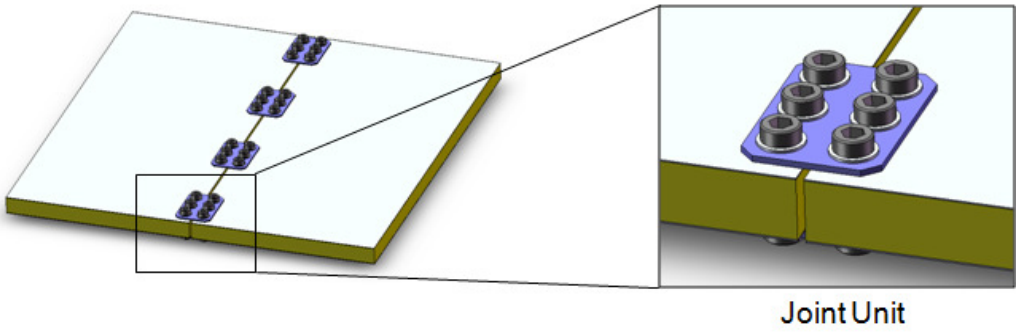

Figure 5-17: Joint line consisting of several joint units

5.4 Efficiency of an In-plane Symmetrical Joint Unit

Because bolts come in discrete sizes (e.g. M4, M5, M6, etc. for metric bolts) there is only one optimum combination of bolt size and bolt number which will maximize the efficiency of a joint under a given load. This can be illustrated by considering the particular case of in-plane joints, subject to purely in-plane loads, designed to operate in friction grip. As was seen in section 5.1.3, for a friction grip joint, the load carrying capability can be calculated by knowledge of the clamping force and the friction coefficient between the relevant faying surfaces of the joint via equation (5-1). This equation is the basis of a bolt selection procedure outlined in the ESA manual on threaded fasteners [69]. This procedure was implemented in a system of spreadsheets to show how friction grip joints with different bolt number and bolt size combinations perform under different ranges of externally applied loads. From a given bolt number and bolt material the bolt selection procedure is used to select the minimum required bolt sizes for a range of external

loads. The bolt sizes are selected from a bolt database which contains information regarding preload capabilities and mass of all the listed bolts. The inserts used in friction grip joints are primarily subjected to a compressive force due to bolt preload and can thus be sized according to the type of bolt that is used in the joint. The bolt database includes the size and mass of the optimized inserts corresponding to all the listed bolts. Hence, when a bolt is selected from the bolt database it is also possible to determine the mass of the resulting joint. Dividing the external load by this value gives the efficiency of the joint in terms of load carrying capability per unit mass.

Using the data generated in the spreadsheets it is possible to generate plots which show how joint efficiency for different bolt number joint configurations varies with external load. An example of such a plot is shown in Figure 5-18. This plot was generated using stainless steel A2/70 bolt properties and is relevant to in-plane joint configurations between two 20 mm thick honeycomb panels.

The behaviour of the curves shown in the above plot can be explained as follows: While the bolt size remains unaltered the overall joint mass stays constant and consequently the efficiency increases linearly with external load. However, after a certain limit in external load is reached a step increase in bolt size is required to provide the necessary clamping force. The selection of a larger bolt size causes a sharp increase in joint mass which in turn results in a sharp decrease in joint efficiency. The process repeats again and again and is graphically represented by the sawtooth shaped curves. This is shown more clearly in Figure 5-19 where only one curve for the 2 bolt joint configuration is shown.

The plot in Figure 5-18 shows that the optimum number of bolts required to maximize joint efficiency is dependent on external load; however, there is no trend towards fewer or greater bolt numbers at lower or higher values of external load. The curves start from a low efficiency due to the fact that no bolts smaller than M5 size were made available in the bolt selection database.

For each curve it can be seen that the efficiency is at its highest when the bolts are operating at a preload level close to their maximum allowable. The sawtooth curves representing the different bolt numbers are staggered meaning that the optimum number of bolts alternates over different external load ranges. So, for example, if the maximum applied load was 12 kN from Figure 5-17 it can be seen that using 5 M5 bolts would give the most efficient joint configuration.

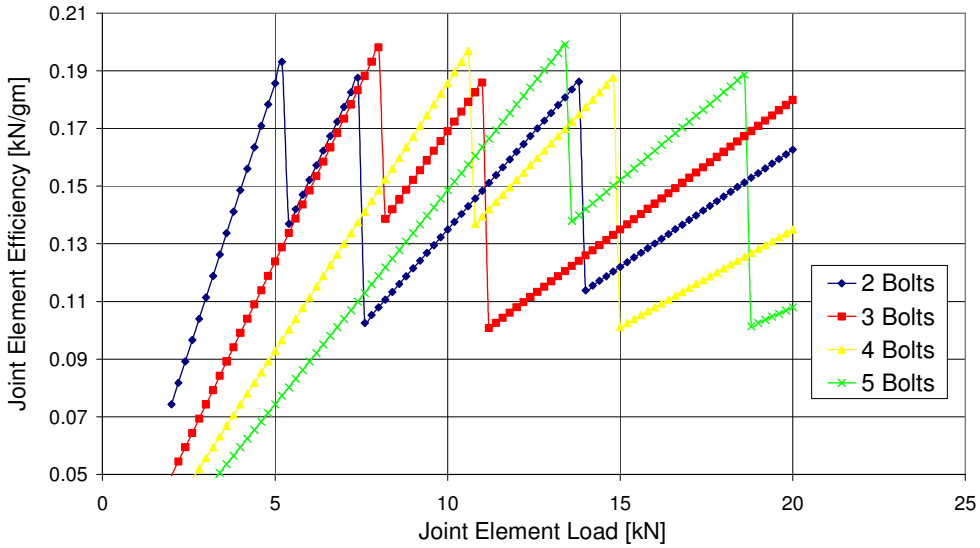

Figure 5-18: Joint efficiency plotted against external joint load

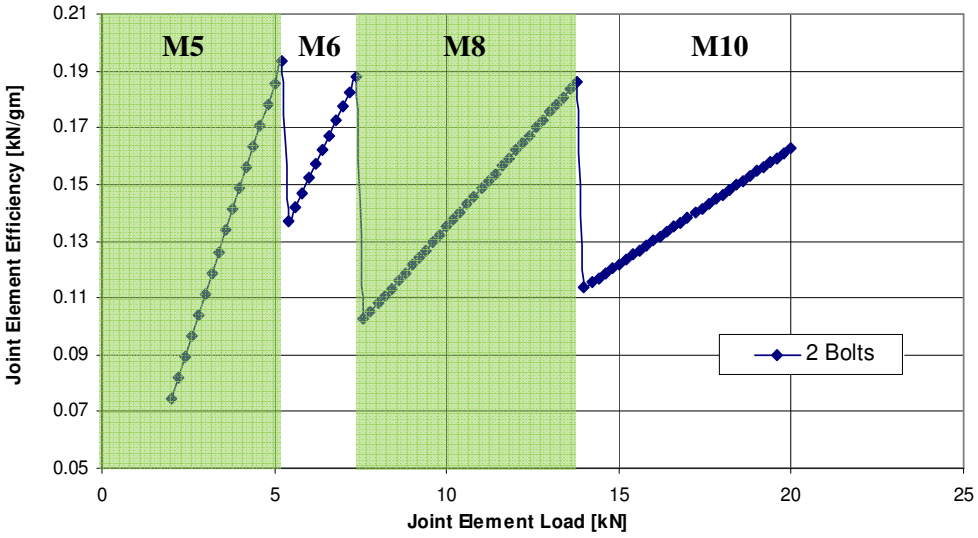

Figure 5-19: Joint efficiency against external load showing bolt selection shifts for 2 bolt configuration

5.5 Finite Element Analysis of Bolted Joints

Apart from generating enough clamping force to ensure friction grip conditions, it is also essential to ensure that the stresses generated from the combined action of the external joint loads and the clamping loads from the bolts do not exceed any of the stress allowables of the joint materials/components. A finite element analysis study was thus conducted to investigate the stresses experienced by different joint unit configurations under various loading conditions. This was also done to take into account loading conditions other than the purely in-plane loading under which a shear joint ideally operates, since in real applications out-of-plane loads of significant magnitude are also likely to be present.

5.5.1 Finite Element Modeling

Various configurations of in-plane bolted joints were modeled in order to assess the effect of the following parameters: number of bolts, separation between bobbins, and bolt material/specification. Geometric models of the joints were created in SolidEdge and were then exported to Ansys Workbench for postprocessing and analysis. Various joint configurations were modeled (see Table 5-1) in order to investigate the effect of the following parameters: no. of bolts, bolt material, and bobbin/bolt separation. For each model five sets of results were generated by considering five fundamental loading conditions: in-plane tension, in-plane compression, in-plane shear, out of plane shear, and out-of-plane bending. These are illustrated in Table 5-2. In-plane bending was not considered since the models focused on single joint units intended to operate amongst multiple joint units along a panel to panel joint line. In such an arrangement any in-plane bending moments applied along the joint line act as in-plane tension or compression loads on the single joint units.

Configuration No.	Bolt Material	No. of Bolts	Bobbins Separation [mm]	Configuration Name
1	SS A2-70	2	1	Joint_s70_no2_sep1
2	SS A2-70	5	1	Joint_s70_no5_sep1
3	SS A2-70	2	6	Joint_s70_no2_sep6
4	SS A2-70	5	6	Joint_s70_no5_sep6
5	Titanium	2	1	Joint_Ti_no2_sep1
6	Titanium	5	1	Joint_Ti_no2_sep6
7	Titanium	2	6	Joint_Ti_no5_sep1
8	Titanium	5	6	Joint_Ti_no5_sep6

Table 5-1: Joint configurations modeled and analyzed

in-plane tension	in-plane compression	in-plane shear
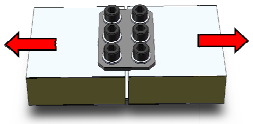	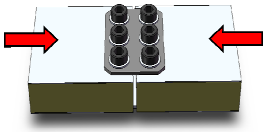	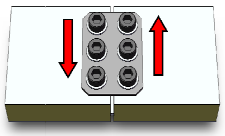
out-of-plane shear	out of plane bending	
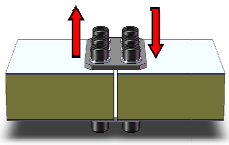	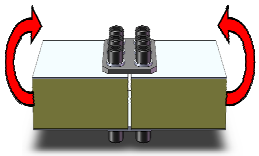	

Table 5-2: Loading conditions considered for the FE analyses of the bolted joint models

The various model configurations were all based on the in-plane shear joint design used for the friction coefficient tests presented in Chapter 6. Two examples of the joint configurations modeled are shown in Figure 5-20 (a) and (b). To improve computational efficiency the sandwich panel was only modeled on one side of the joint while for the other side, the reinforced substrate of the panel was approximated by modeling a solid aluminium block. The material properties used for the models are detailed in Table 5-3 and Table 5-4. For the modeled honeycomb panel the same sandwich properties of the type of panel used in the friction tests were used. The same overall sandwich thickness of 20 mm was used

while the other two planar dimensions were set high enough as to avoid panel edge influences. The bobbin inserts used to reinforce the sandwich substrate at the bolt hole locations were also modeled. The modeled bobbins were sized on the basis of the bolt specification and preload capability. The honeycomb core was modeled as isotropic (see Table 5-4). The shear modulus of the equivalent isotropic core, G, was set equal to the circular shear modulus of the core, G_C, and the Young's modulus was in turn set according to $E = G2(1+\nu)$, where the Poisson's ratio, ν, was taken as 0.3.

Element	Aluminium Alloy	E [GPa]	Tensile Yield Stress [MPa]	Ultimate Tensile Stress [MPa]
Connecting Strip	7075	72	391	447
Aluminium Skin	2014	73	370	426
Bobbin Inserts	6082	72	398	475

Table 5-3: Material properties used for the metallic elements of the joint models

Core Type	G [MPa]	v	E [MPa]	L Direction Shear Strength [MPa]	W Direction Shear Strength [MPa]
¼"-5056-0.0025"**	64.3	0.3	171.0	3.44	2.07

Table 5-4: Honeycomb core properties (assumed isotropic)**

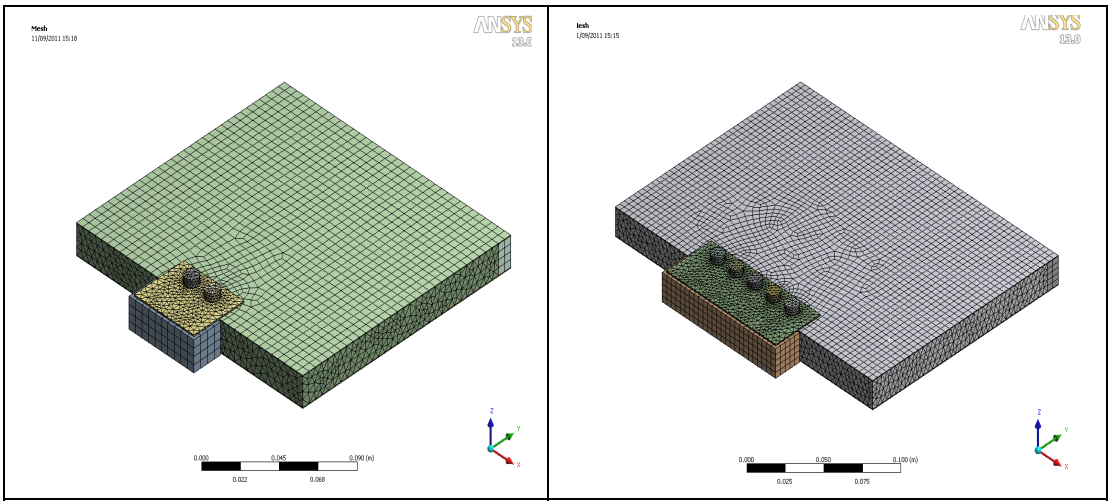

(a) Two bolt configuration (b) Five bolt configuration

Figure 5-20: Finite element models of two joint configurations

For the in-plane load cases the load magnitude applied to the models was defined on the basis of the maximum clamping force achievable by the particular joint configuration. Hence this was dependant on the bolt specification and the number of bolts. The external load was then set equal to the slip load resulting from the given clamping force and an assumed (conservatively high) friction coefficient of 0.35. The relevant bolt preload levels, dependant on the bolt specification, were also included in the models. To avoid the requirement for a non-linear solution and reduce computational cost the contact condition between the connection strips and the sandwich panel were modeled as bonded contacts (rather than frictional) in the vicinity of the bolt holes by defining annular area of contact corresponding to the projected bolt loading frustum. A slip limit criteria was also applied for the out-of-plane bending loads analysis by multiplying the in-plane slip load of the particular joint configuration by a moment arm proportional to the panel dimensions. The obtained bending moment was then directly applied in the models.

The out-of-plane shear loading criteria was based on the shear strength of the modeled honeycomb core. For each model the out-of-plane load was obtained by multiplying the shear strength of the core by a cross-sectional panel area proportional to the joint unit perimeter affecting the panel.

Due to the large preload scatter associated with bolt tightening methods each of the above loading conditions were applied twice for a maximum and a minimum level of preload. Ten sets of results were thus obtained from each model. The contour plots from each model solution were carefully analyzed and the maximum stresses experienced by the joint and sandwich panel components were recorded in a global table of results for comparison. These tables are all presented in Appendix C.

5.5.2 Discussion of Finite Element Results

Examples of the stress and deformation plots for one of the joint configurations under the 5 loading conditions considered are shown in Figure 5-21. From the finite element results it was possible to make a number of observations. Firstly, as

expected, the connection strips are almost always the most highly stressed components, and the stresses to which they are subjected are particularly high for out-of-plane loads. The finite element results also showed that, for equivalent external joint load/joint clamping force ratios and connection strip dimensions proportional to number of bolts, the connection strips are subject to higher stresses in joint units with greater number of bolts than joint units with fewer bolts. This is due to the fact that the stress is not evenly distributed along the joint line. For joint configurations with more than two bolts the stresses are higher around the outer bolts (see Figure 5-22). In this respect joint units with more bolts seem to be less effective at carrying loads than joint units with fewer bolts. This clearly has implications on joint configuration selection and could be used to expand on the joint selection procedure presented in section 5.4. Quantifying the effect would require modeling more configurations than the ones which were considered here. This was not done within the scope of this work due to time limitations.

From the results it was also observed that the high clamping loads necessary to ensure friction grip conditions in optimized joints induce very high stresses on the connection strips. This is especially the case when highly specified fasteners such as titanium bolts are used. In such cases bolt preload alone is likely to take the stresses in the connection strips close to the maximum stress allowable of the material. This has highlighted a need to find better ways of distributing the high clamping forces generated by bolt preload. An obvious way of achieving this is by using thick washers.

Bobbin insert separation or bolt hole separation did not appear to have a significant effect on the stresses generated in the various joint parts. In view of this choosing closer bobbin separation is advisable since the resulting joint groups will be more compact and lighter.

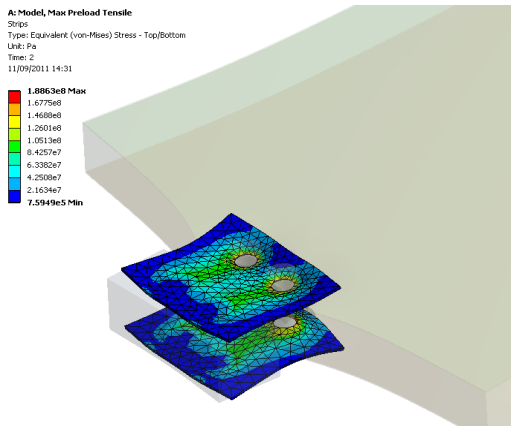

In-plane tension

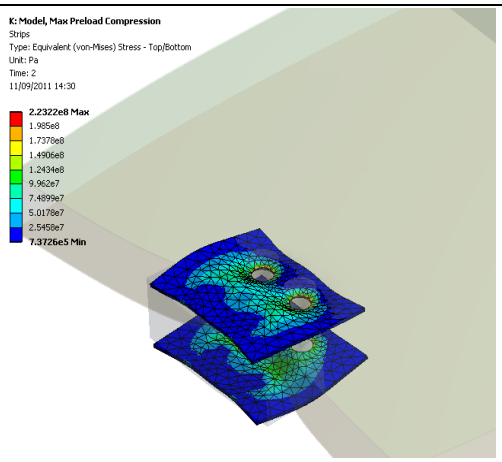

In-plane compression

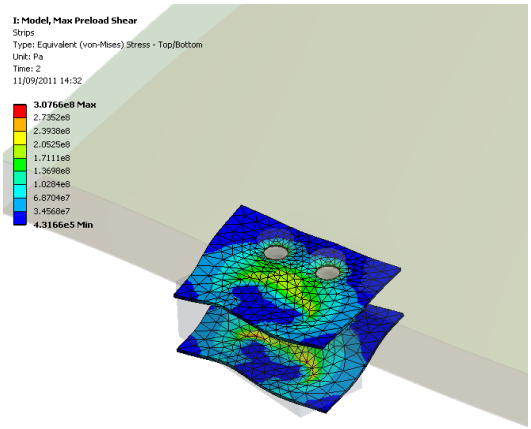

In-plane shear

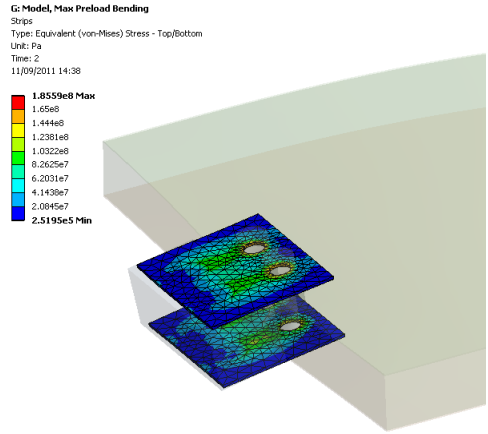

Out-of-plane bending

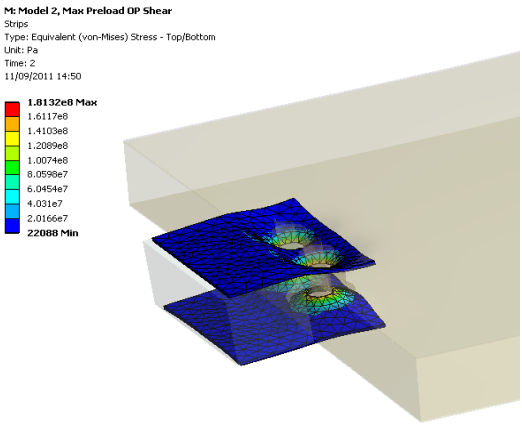

Out-of-plane shear

Figure 5-21: Cleat plate deformation for configuration no. 1 under the 5 loading conditions considered

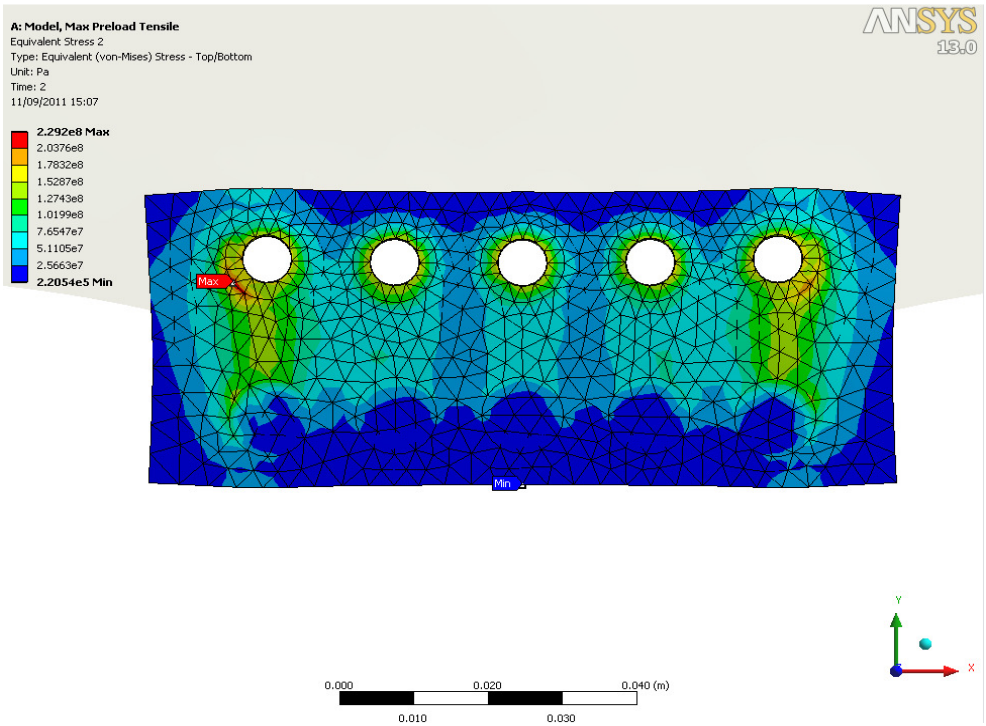

Figure 5-22: Stress distribution on one of the connection strips for joint configuration no. 4 under tensile load

5.6 Conclusions

Since the first pioneering works of Leonardo da Vinci, Amontons, and Coulomb (to cite a few) countless works have been published to better understand friction phenomena. However, from the literature survey it is evident that there are relatively few works which specifically focus on the problem of friction as applied to bolted joints and friction grip bolted joints in particular. Furthermore, apart from very relevant work from Baylis [97] most studies on the friction coefficient of bolted joints are in the field of civil engineering and deal with large scale steel structures which are substantially different from spacecraft structures.

Surface texture is a key property in defining tribological behaviour. Many works have been published on the effect of surface roughness on the frictional properties contacting surfaces. A large portion of these works are theoretical, proposing various models to describe and understand the frictional behaviour of rough surfaces. Furthermore, many of the experimental studies that have been carried out

are aimed at verifying these theoretical models and hence the results obtained are usually only relevant to ideal contact pair set-ups that can only be achieved in laboratory conditions. However, from these experimental works it emerges that the results obtained from several of these theoretical works correlate well and are qualitatively accurate. The works all agree on the fact that the key parameters in defining the frictional parameters of rough surfaces are plasticity index and surface adhesion. The plasticity index is inversely proportional to surface hardness and directly proportional to surface roughness. It is interesting to note that friction coefficient decreases with increasing plasticity index. Hence unless the surface hardness is very high increasing surface roughness can result in a substantial decrease in friction coefficient. It is not surprising that higher adhesion parameter values result in higher friction coefficient values. However, this parameter may be considered less important for the applications considered here since contacting surfaces are likely to be covered in oxide layers which inhibit metal to metal adhesive bonding. Hence friction is more likely to be dominated by ploughing of asperities.

When considering the use of surface roughness to increase friction coefficient it is also important to consider the resulting surface texture which ultimately determines the frictional behaviour. Different abrasion techniques can be used to obtain surfaces with nominally equivalent values of surface roughness (as defined by single parameters such as the commonly used average roughness R_a); however, the resulting surface textures may be substantially different in terms of their topography.

The work here presented highlights and takes steps in addressing the main issues associated with the design of optimized bolted joints between honeycomb panels. Firstly the efficiency (in terms of load carrying capability per unit mass) of shear joint units operating under friction grip conditions was investigated by purely considering their performance on the basis of clamping force capabilities. Using

this approach it was shown how the optimum combination of bolt number and bolt size for a particular joint configuration varied with externally applied load.

A finite element analysis campaign was also carried out to investigate the influence of bolt number, bolt material and bolt distribution on the stresses experienced in the joint components (especially the cleat plates) under different loading conditions. As expected it was found that in most cases the cleat plates are subjected to the highest stresses and that the stresses to which they are subjected are particularly high for out-of-plane loads. However, it was found that bolt preload alone generates very high stresses in the cleat plates and that distributing these high clamping loads is one of the main challenges in achieving optimized joints. The finite element results also showed that joint configurations with higher number of bolts appear to be less effective carrying external loads due to the uneven stress distribution along the joint. Quantifying this effect could be a good starting point for any future work that is carried out in this area.

Chapter 6

6 In-plane Testing of Bolted Joints

The determination of the clamping force necessary to ensure friction grip conditions requires accurate knowledge of the friction coefficients. The friction coefficient between two faying surfaces is highly sensitive to the surface conditions and hence can only be accurately determined through tests. In view of this a series of test campaigns were conducted in order generate friction coefficient values relevant to joint materials/components of interest, which are typically used in spacecraft structures. As discussed in section 5.2.3 achieving a high friction coefficient is desirable since it reduces the clamping requirement and hence the mass of the joint. Several configurations were considered and initially a scattergun approach was used to hone in on the most interesting joint solution. Two test campaigns were thus carried out: Test Campaign 1 & 2. The first one coincided with the first part of the investigation where as many different configurations as possible were tested to see which parameters influenced the friction coefficient the most. The second test campaign focused on investigating the effect of surface abrasion which from the first test campaign emerged as being the most promising way of influencing the friction coefficient. The two test campaigns are discussed in detail in the following subsections.

6.1 Testing Procedure

The test procedure was common to both of the test campaigns. Static tensile tests were conducted on bolted joints with known bolt preload values. The joints tested were composed of two 100 × 60 × 20 mm honeycomb panel blocks (see Figure 6-1 (a)) clamped between two 50 × 35 × 2 mm cleat plates (see Figure 6-1 (b)) at either side. The panel blocks structure consisted of 0.5 mm thick aluminium facing sheets

sandwiching an aluminium honeycomb core designated as ¼" - 5056 - 0.0025" (which should be read as: cell size in inches – Al alloy – foil thickness in inches), 6.35 mm in cell size and 83 kg/m^3 in density. In order to maximize the friction coefficient data that could be obtained from the experiments the panel blocks could be connected in multiple configurations. In all tests two M6 bolts were used to join the assembly together. The panel blocks had three 10 mm clearance holes, so for each panel block a total of three friction tests relevant to virgin surface conditions could be carried out. The core of the panel blocks was locally reinforced with three aluminium bobbin inserts at the bolt hole locations.

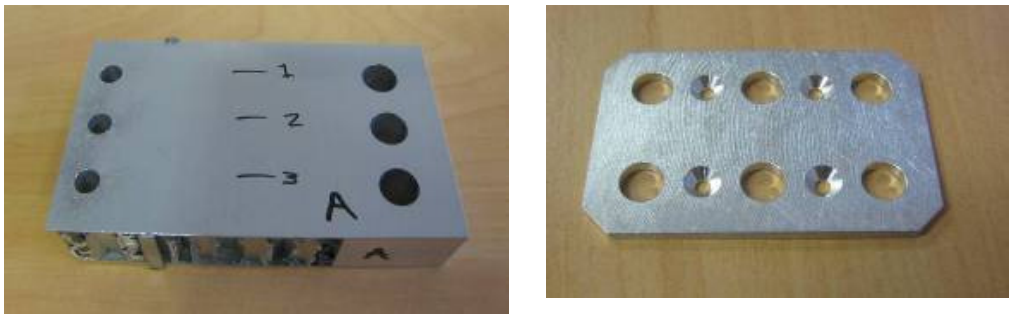

(a) Honeycomb panel block (b) Cleat Plate

Figure 6-1: Joint elements used in the tests

All tests were conducted using an Instron 5559 screw driven universal testing machine equipped with a 50 kN load cell. The panel blocks could be connected to the Instron machine via two clevises which fitted into the top and bottom wedge grips of the machine. The test joints were installed in the test machine as shown in Figure 6-2. When assembling and installing the test joints great care was taken not to contaminate the surfaces of the test articles. These were kept in clean bags and whenever handled latex gloves were worn.

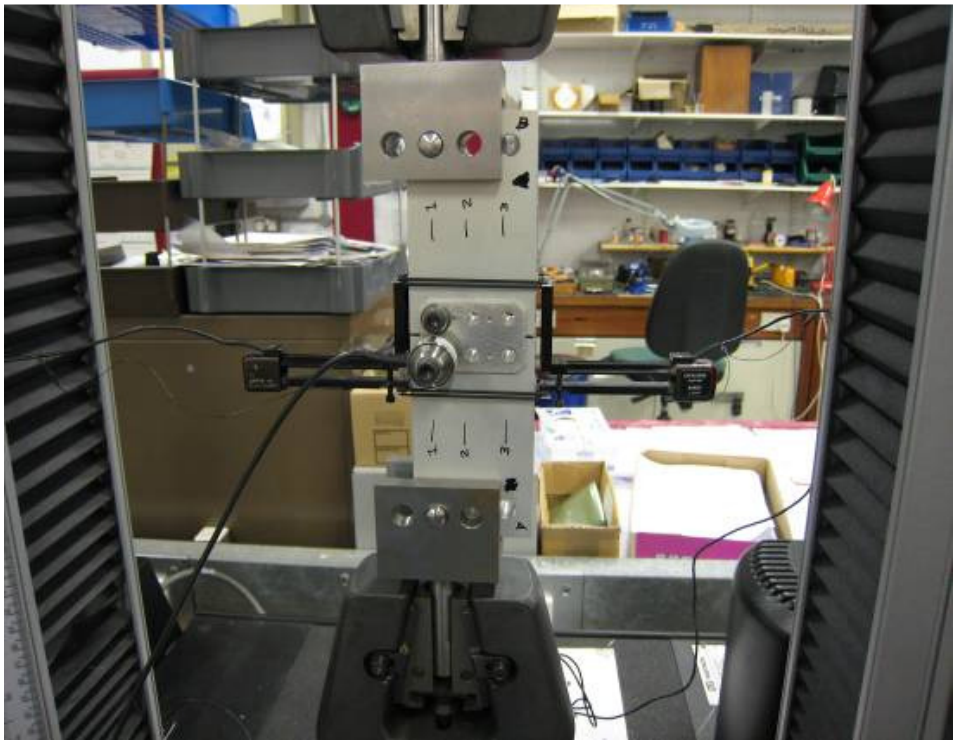

Figure 6-2: Test-joint set up in the testing machine with extensometers and load cell

A Novatech F207 20 kN washer type load cell (see Figure 6-3) was used to accurately measure the bolt preload on one side of the joint, and a torque wrench was used to tighten the bolts. Two strain gage extensometers were used to measure the increase in joint separation and possible rotations due to misalignment (see Figure 6-4). Even though care was taken in maintaining a straight alignment of the test joints by assembling them using a jig slight misalignments could not be avoided.

The test joints were loaded in tension at a rate of 0.05 mm/min until slip occurred. This was made to occur on the 20 kN load cell side by applying a significantly higher level of torque to the bolt on the other side of the joint. As each test ran, data from the Instron machine load cell, crosshead displacement, and relative displacement from the extensometers were acquired and plotted in real time.

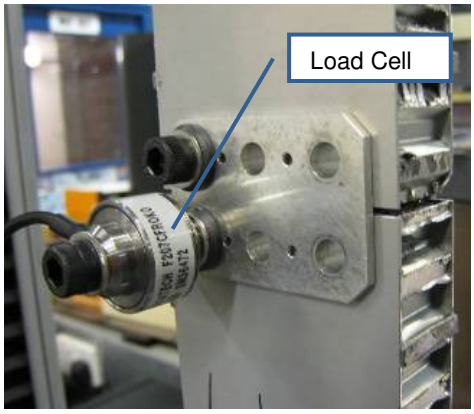

Figure 6-3: Load cell installed in load path of bolt

Figure 6-4: Extensometer applied to test joint

6.2 Test Campaign 1

The first test campaign was carried out with the aim of testing as many joint configurations as possible to determine which parameters had the strongest influences on the resulting friction coefficient.

6.2.1 Test Campaign 1 Joint Configurations

Five test types were carried out in order to investigate the effect of different cleat plate materials and surface finish conditions on the resulting joint friction coefficient. A test matrix summarizing the joint configurations tested is detailed in Table 6-1. Three test types were conducted for three cleat plate materials: Al7075, titanium, and Al7075 cleat plates clad in Al2014. The 7075 aluminium alloy is an aerospace grade alloy conventionally used for these applications, while titanium is only used in the most demanding structural applications. Due to its more modest properties the 2014 aluminium alloy is less recognised in the high end space sector but potentially attractive due to its lower cost and hence of interest to this investigation. The skins of the panel blocks were prepared according to the following criteria: *'NO VISUALLY RAISED DEFECTS, DEFORMITIES OR DEPRESSED AREAS EXCEEDING 50mm^2 AND 40 microns IN DEPTH. NO BURRS PERMITTED ANYWHERE INCLUDING DRILLED HOLES. NO*

SCRATCHES EXCEEDING 10 microns IN DEPTH. FREE FROM ABRASIONS, INCLUSIONS AND CONTAMINATION'. The cleats were finished to N6 standard ($R_a \leq 0.8$ μm).

A further two test types were conducted for the Al7075 cleats and the titanium cleat materials to investigate the effect of surface abrasion. For these two test types both the cleat plates and the panel block surfaces were abraded to a roughness of Ra~2.5 by bead blasting using recycled media.

Designation	Panel Block Skin		Cleat Plate	
	Material	Abraded	Material	Abraded
Al-Al	Al	No	Al7075	No
Al-Ti	Al	No	Titanium	No
Al-Clad	Al	No	Al2014	No
Alabr-Alabr	Al	Yes	Al7075	Yes
Alabr-Tiabr	Al	Yes	Titanium	Yes

Table 6-1: Test configurations

6.2.2 Test Campaign 1 Results

For each joint configuration three tests were carried out for virgin surface conditions. Each test was repeated twice (reuse 1 and 2) for the first three non-abraded configurations and once for the other two abraded configurations to investigate the effect of surface reuse. All tests were conducted by applying a nominal bolt preload of 7.5 kN on the slip side of the joint where the washer type load cell was installed.

An example of the load-extensometer displacement plots obtained from the experiments is shown in Figure 6-5. The differences between the two extensometer curves are mainly due to rotations caused by misalignment. A curve corresponding to the mean between the two extensometer signals is also included in the plots. As can be seen in Figure 6-5 the load-extensometer curves can be split into 4 regions. In the first region the curves are initially linear with a steep gradient which indicates that friction grip conditions are maintained. In the second region the

curves slowly deviate from the initial linear trend as the gradient slowly reduces, which is an indication that micro-slip is occurring. In the third region an elbow in the curve is reached in which the gradient decreases fairly rapidly indicating a transition from micro-slip to macro-slip. Finally in the forth region the curve becomes almost horizontal indicating that the joint has slipped. The curves will remain almost horizontal until the relative movement between the clamped parts is so great that the shanks of the bolts come into contact with the bolt holes and bearing mode is reached at which point the load will steeply increase.

The curve deviation of region 2 and the "elbow" of region 3 can be more or less pronounced depending on the joint configuration, however, in many cases the transition from friction grip conditions to slipped conditions is not immediate, meaning that extracting a slip load value from each test is not straightforward. To minimise the chances of misinterpretation the criteria for defining friction coefficient comprised the extraction of two values of slip load and corresponding friction coefficient from each test: an initial friction coefficient and a nominal friction coefficient. The initial slip load was defined as the load at which the load-extensometer curves deviate from the initial linear trend of region 1. The nominal slip load was defined as the load at which the initial linear trend of region 1 intersects the final near-horizontal trend of region 4. The intersection of these two trend lines can be seen in Figure 6-6.

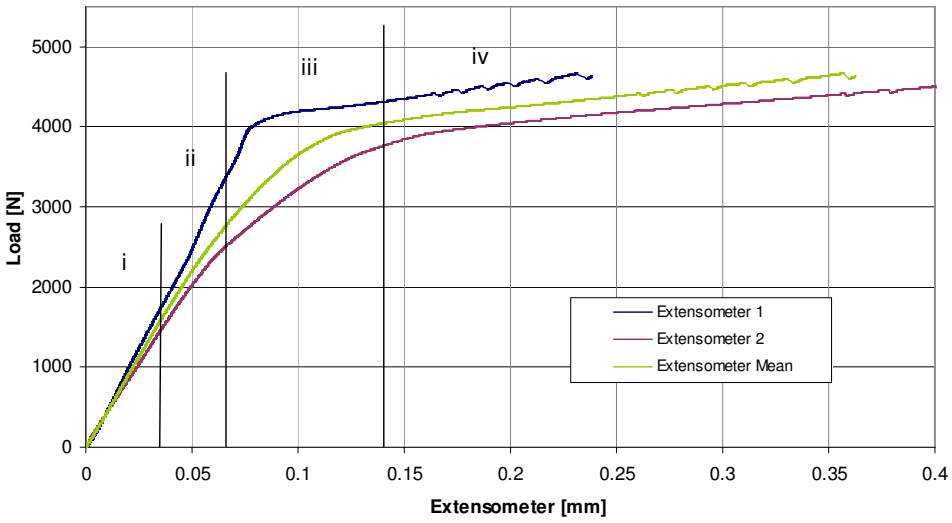

Figure 6-5: Load-extensometer curves for a test joint with 7075 aluminium cleat plates

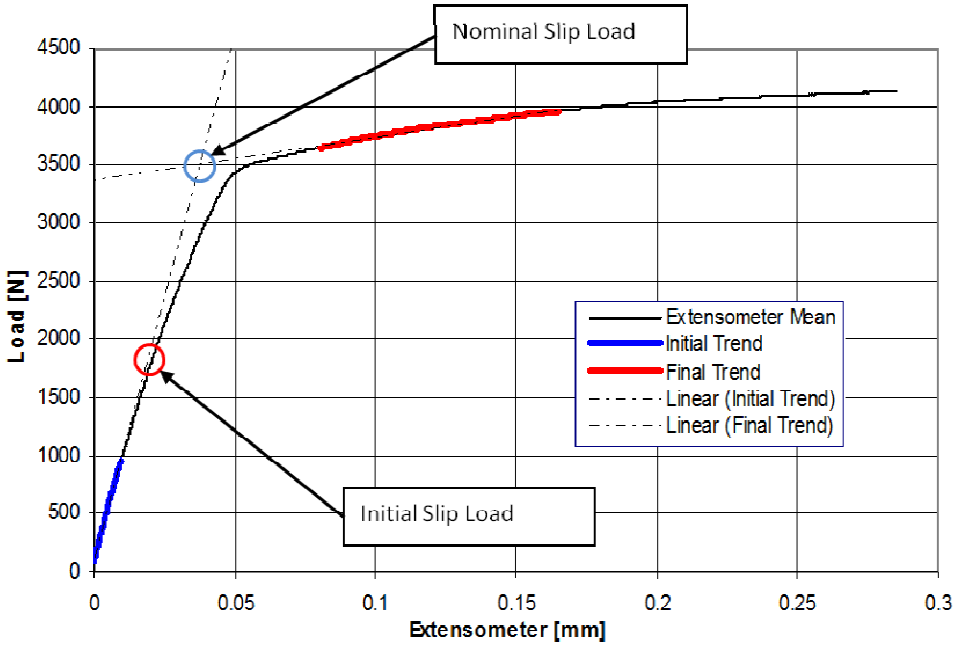

Figure 6-6: Load-extensometer curve with trend lines added for the determination of friction coefficient values

The averaged results for the friction tests relevant to non-abraded surfaces are summarized in Tables 6-2 to 6-4. Each averaged value was obtained from three test runs (see D for the full tables of results). From these results it can be seen that the values of friction coefficient do not vary significantly between the cleat plate

materials considered. For virgin surfaces the Al-Al joint configuration appears to offer the highest friction coefficient values but these are only marginally higher than those obtained for the Al-Clad configuration. Still considering virgin surface conditions the Al-Ti configuration generated the lowest values of friction coefficient with an averaged initial and nominal friction coefficient values respectively ~25% and ~5% lower compared with the Al-Al configuration. Surface reuse also does not appear to have a very significant effect on the friction coefficient. However, from the results it can be noted that generally the friction coefficient increases with surface reuse and repeated reuse. This trend is more pronounced for the Al-Clad configuration which generated the highest values of nominal friction coefficient for reuses 1 and 2.

	Friction Results (Al-Al)			
	Initial Friction Coeff.		Nominal Friction Coeff.	
	Average Value	Standard Dev.	Average Value	Standard Dev.
Virgin	0.166	0.052	0.259	0.020
Reuse 1	0.138	0.005	0.275	0.020
Reuse 2	0.138	0.015	0.267	0.020

Table 6-2: Friction results for test configuration Al-Al

	Friction Results (Al-Ti)			
	Initial Friction Coeff.		Nominal Friction Coeff.	
	Average Value	Standard Dev.	Average Value	Standard Dev.
Virgin	0.130	0.007	0.246	0.011
Reuse 1	0.149	0.034	0.260	0.012
Reuse 2	0.112	0.015	0.262	0.012

Table 6-3: Friction results for test configuration Al-Ti

	Friction Results (Al-Clad)			
	Initial Friction Coeff.		Nominal Friction Coeff.	
	Average Value	Standard Dev.	Average Value	Standard Dev.
Virgin	0.155	0.011	0.255	0.008
Reuse 1	0.131	0.024	0.280	0.029
Reuse 2	0.149	0.052	0.306	0.013

Table 6-4: Friction results for test configuration Al-Clad

The averaged results for the abraded tests are summarized in Tables 6-5 to 6-6. Each averaged value was obtained from three test runs (see Appendix D for the full tables of results). From these results it can be seen that surface abrasion can significantly increase the friction coefficient. Compared with the corresponding non-abraded configurations, for the Alabr-Alabr configuration the nominal friction coefficient is almost doubled while for the Alabr-Tiabr configuration the nominal friction coefficient is more than doubled. Because of this greater increase, for these abraded tests the effect of material influence is reversed with the titanium cleat plates generating a higher friction coefficient compared to the aluminium ones. This is probably due to the fact that the physical mechanism behind the manifestation of friction is different for abraded surfaces. For abraded surfaces friction is probably dominated by ploughing by asperities. Because titanium has a higher strength than aluminium the asperities generated by the abrasion process are less likely to be worn down by shearing loads when the joint is loaded thus resulting in a higher friction coefficient.

The effect of surface reuse also appears to be reversed for the abraded test results. This may also be explained by the dominating role played by surface asperities which with reuse are worn down causing a reduction in friction coefficient.

	Friction Results (Alabr-Alabr)			
	Initial Friction Coeff.		Nominal Friction Coeff.	
	Average Value	Standard Dev.	Average Value	Standard Dev.
Virgin	0.209	0.006	0.518	0.017
Reuse	0.189	0.003	0.458	0.014

Table 6-5: Friction results for test configurations Alabr-Alabr

	Friction Results (Alabr-Tiabr)			
	Initial Friction Coeff.		Nominal Friction Coeff.	
	Average Value	Standard Dev.	Average Value	Standard Dev.
Virgin	0.267	0.006	0.587	0.010
Reuse	0.209	0.006	0.482	0.041

Table 6-6: Friction results for test configurations Alabr-Tiabr

6.3 Test Campaign 2 – Effect of Surface Abrasion

From test campaign 1 surface abrasion clearly emerged as the most promising method for increasing the friction coefficient between the faying parts of a bolted joint. The aim of this test campaign was to further investigate the effect of surface abrasion and obtain statistically significant data samples for the considered configurations and surface treatments.

6.3.1 Surface Abrasion

As for the previous test campaign surface abrasion was applied via the bead blasting process whereby abrasion is achieved by firing the part with a fine powder of glass beads with a known back pressure. This allows for the surface to be roughened in a controlled manner by tailoring back pressure and glass bead size. The process can be carried out using recycled or non-recycled media for the powder. In the previous test campaign were surface abrasion was first investigated recycled media was used. However, for this test campaign all the coupons were abraded using non-recycled media to achieve a more controlled and repeatable process. Efforts were made to obtain a similar surface topology to the abraded coupons used in the previous investigation (~Ra 2.5). Two candidate abrasion parameter combinations emerged from the various trials (see Figure 6-7) as being of most interest and hence were applied to the coupons tested here. The two surface abrasion specifications used are detailed in the table below

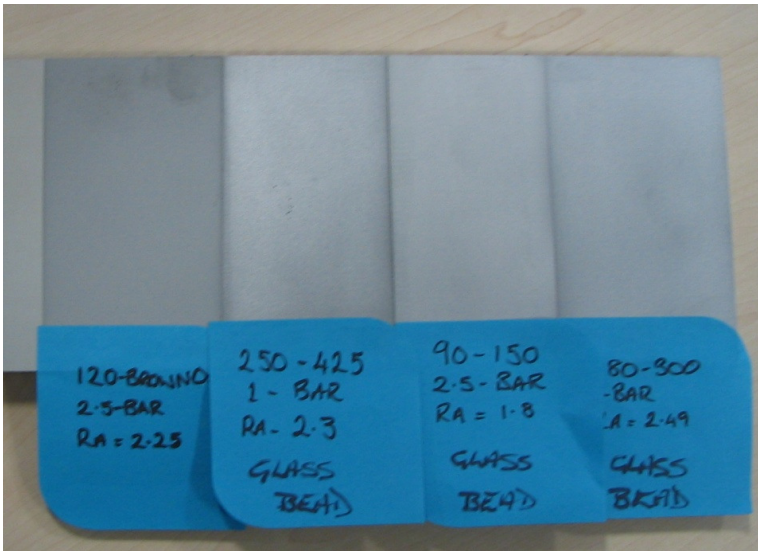

Figure 6-7: Surface finishes obtained from different bead blasting trials

Type	Abraded Method
1	250-425 µm 1 Bar Ra 2.30 Glass bead
2	180-300 µm 1 Bar Ra 2.49 Glass bead

Table 6-7: Bead blast parameters used to abrade the surfaces

Two sets of test coupons associated with the two abrasion types were tested. For each test type both the panel blocks and the cleat plates were treated with the same level of surface abrasion. Nine tests were carried out for each test type as detailed in Table 6-8.

Test Type	Panel Block Abrasion	Cleat Plate Abrasion	No. of tests
Alabr-Aabrl-1	Type 1	Type 1	9
Alabr-Alabr-2	Type 2	Type 2	9

Table 6-8: Test matrix

6.3.2 Test Campaign 2 Results

The results for all the carried out test runs are summarized in Tables 6-9 and 6-10. Since the number of data samples was large enough it was possible to statistically analyze the data to generate meaningful A-Basis and B-Basis allowables. The results obtained are very similar to the ones obtained for the abraded tests from the first test campaign and confirm that abraded surface treatments can be used as a reliable way of achieving high values of friction coefficient. There is not a significant difference between the results from test type 1 and 2 indicating that greater variation in the abrasion parameters would be required to see a more significant impact on the friction coefficient. The values obtained for test type 1 are slightly higher compared to the ones obtained for test type 2. For type 2 the surface roughness was higher so the reduction in friction coefficient could be attributed to an increased plasticity index, which would be in agreement with the theoretical findings from the literature presented in section 5.2.3. The asperities are also likely to provide less shearing resistance since although they are more pronounced they are also weaker. Considering the variability typically associated with friction data the standard deviations of the results obtained here are small and indicate good repeatability.

Test ID	Initial Slip Load [N]	Nominal Slip Load [N]	Initial Friction Coefficient	Nominal Friction Coefficient
T1_B1_1	4252	8762	0.283	0.584
T1_B1_2	4234	9177	0.282	0.612
T1_B1_3	4225	9390	0.282	0.626
T1_B2_1	4014	9233	0.268	0.616
T1_B2_2	4247	8996	0.283	0.600
T1_B2_3	4107	8557	0.274	0.570
T1_B3_1	4124	8388	0.275	0.559
T1_B3_2	4232	8800	0.282	0.587
T1_B3_3	4120	8254	0.275	0.550
	Average		**0.278**	**0.589**
	Standard Deviation		**0.006**	**0.026**
	A-basis		**0.251**	**0.481**
	B-basis		**0.262**	**0.525**

Table 6-9: Alabr-Alabr-1 (type 1) abrasion test results

Test ID	Initial Slip Load [N]	Nominal Slip Load [N]	Initial Friction Coefficient	Nominal Friction Coefficient
T2_B1_1	4256	9233	0.284	0.616
T2_B1_2	4308	8800	0.287	0.587
T2_B1_3	4223	7817	0.282	0.521
T2_B2_1	4245	8061	0.283	0.537
T2_B2_2	4290	8431	0.286	0.562
T2_B2_3	4106	7498	0.274	0.500
T2_B3_1	3980	8432	0.265	0.562
T2_B3_2	4030	7791	0.269	0.519
T2_B3_3	4083	8323	0.272	0.555
	Average		**0.278**	**0.551**
	Standard Deviation		**0.008**	**0.036**
	A-basis		**0.245**	**0.402**
	B-basis		**0.258**	**0.463**

Table 6-10: Alabr-Alabr-2 (type 2) abrasion test results

6.4 Conclusions

Two test campaigns were carried out in order to gather friction coefficient data relevant to the type of materials typically used in shear joints between honeycomb panels used in space applications. For the first test campaign relatively small variations in friction coefficient were found between the three tested cleat plate materials. For virgin and non-abraded surfaces the average nominal friction coefficient values were all in the region of 0.25-0.26. Surface reuse also did not appear to have a large impact on the friction coefficient between non-abraded parts, with only moderate increases noted for the two reuses. This may be attributed to the gradual roughening and removal of the oxide layer on the face sheets of the panel blocks. Surface abrasion had significant effect on friction coefficient. Here the tests relevant to virgin surfaces gave an average nominal friction coefficient value of 0.5 for the Al cleat plates and almost 0.6 for the Ti cleat plates. The effect of surface reuse was again mild but contrary to what was observed for the non abraded tests, it appeared to slightly reduce the friction coefficient. This may be explained by the dominating role played by surface asperities for abraded parts which with reuse are worn down causing a reduction in friction coefficient.

The effect of surface abrasion was further investigated in a second test campaign which focused on only two contact pairs with different levels of surface abrasion. For each of these larger data samples were obtained compared to the previous test campaign. The results obtained were very similar to the ones obtained for the abraded tests conducted in the first test campaign confirming that surface abrasion is an effective way of increasing the friction coefficient. From the statistical analysis of the result the obtained standard deviations were relatively low. Although these results were obtained under controlled laboratory conditions this suggests that surface abrasion is also a reliable way of guaranteeing high values of friction coefficient.

Chapter 7

7 In-Plane Joint Bearing Tests: Insert Shear Out

7.1 Introduction

As explained in Chapter 5 the bolted joints considered in this work are designed according to the friction grip philosophy. However, in spacecraft design the typically applied structural margins are not large, which combined with the uncertainty of friction as a load path means the risk of joint slip is high [2]. It is thus important to ensure that the joint has sufficient strength without friction. This is to safeguard against the unlikely case where the right fastener preload is not applied during installation, or where vibration or shock cause a significant loss of preload. To this end a series of bearing joint tests were conducted on the same type of joints that were tested for friction in the previous Chapter. Various joint configurations were tested to see if any of the parameters would have an effect on the strength or the failure mode.

The tests were also done to assess the shear out strength of the hot bonded inserts incorporated in the panel blocks of the test joints since insert shear out was the expected failure mode. As mentioned in section 4.1 little literature has been published on the topic of inserts and most of it focuses on pull out strength. Heimbs and Pein [34] is the only work that could be found which considers the shear strength of inserts. In this work an experimental and numerical investigation was carried out on the shear strength of partially potted bobbin inserts in Nomex honeycomb core sandwich structures.

7.2 Test Procedure

The adopted test procedure was very similar to the procedure described in section 6.1 used for the friction test. The test joints used here consisted of the panel blocks and connecting cleat plates previously used for the friction tests described in

chapter 6. The main difference in the set-up of these tests was that no external instrumentation (i.e. no extensometers and no fastener load cell) was used due to the risk of damaging it. Figure 7-1 shows the test set-up. All the test were carried out using an Instron 8032 universal testing machine equipped with a 100 kN load cell. As for the friction tests the bolted joints tested here were loaded in displacement control but at higher loading rate of 1.5 mm/min, due to the significantly greater displacements associated with this test. During the tests cross-head displacement and load cell data were acquired at 10 Hz. For each test the joints were loaded to take out the tolerances until the fasteners were bearing the fastener holes of the fittings. All the tests were destructive and were only stopped after failure of the test joint was observed.

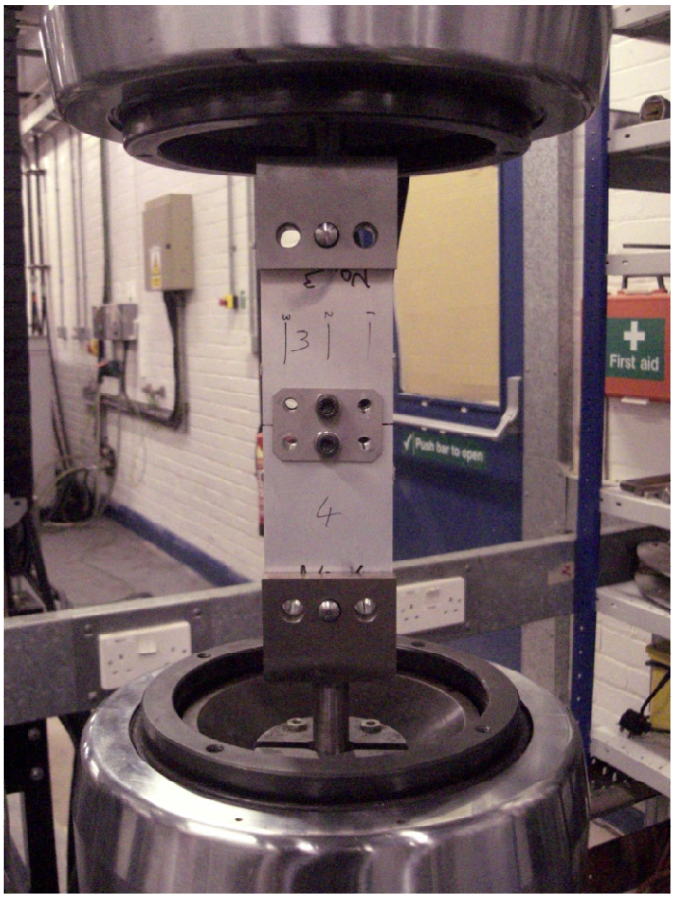

Figure 7-1: Test set-up

7.3 Test Configurations

Four joint configurations were tested using the procedure described above. Table 7-1 provides a summary of the configurations tested. Different preloads were applied to the upper and lower fasteners. Two levels of preload were specified: labelled as T_{High} and T_{Low}. The high preload level, Thigh, corresponds to a nominal preload of 7.5 kN which would be normally specified to ensure friction grip conditions for this type of joint. Since the load cell could not be used for this test the preload was applied by torque controlled tightening. A torque of 8.5 Nm was used based on the torque-preload relationship obtained for the fastener used. For the low level preload, T_{Low}, a torque of 0.5 Nm was used to just lightly clamp the joint parts together. In this condition no load is carried via friction and the clamped parts are allowed to slide over each other with little resistance. As can be seen from Table 7-1 different cleat plate materials and cleat plate surface treatments were used in the different configurations.

Test No	Upper M6 Torque	Lower M6 Torque	Panel Blocks	Cleat Plates
1	T_{HIGH}	T_{HIGH}	Non-Abraded	Abraded Ti Plate
2	T_{HIGH}	T_{LOW}	Non-Abraded	Non-abraded Al Plate
3	T_{HIGH}	T_{LOW}	Non-Abraded	Non-abraded Ti Plate
4	T_{LOW}	T_{LOW}	Non-Abraded	Non-abraded Ti Plate

Table 7-1: Test matrix

7.4 Test Results

The results from the four test runs are summarized in Table 7-2 and the load-displacement curves are shown in Figure 7-2. As can be seen from the table all the failures occurred by shear out of the bobbin insert. The various configurations did not appear to have a significant influence on the maximum loads achieved by the joints; however, as can be seen from Figure 7-2 they did have an effect on the load-displacement profiles. For configuration 1 it can be seen that up to about 4.5 kN the load-displacement curve is steep indicating that the load is being carried by friction. At about 5 kN the joint slips and the load-displacement curve becomes

near horizontal. As the joint goes into bearing the load increases again until ultimate failure occurs.

The curves for configuration 1 and 2 are very similar. They both start with a near horizontal region corresponding to the lower part of the joint slipping from the start due to the low preload. As the lower part of the joint goes into bearing the slope of the curves increases until the upper part of the joint slips and the curves become horizontal again. Finally, as the upper part of the joint goes into bearing as well the load increases rapidly until the maximum load is reached.

For configuration 4 the preload was low on both sides and the load-displacement curve is near horizontal until both sides of the joint are in bearing.

An image of one of the failed coupons is shown in Figure 7-3 where it can be clearly seen that the central bobbin sheers out together with the surrounding adhesive foam. It can also be seen that a section of the face sheet is torn out as a result of the bearing load.

Test No	Failure Mode	Location	Max Load
1	Insert Shear Out	Lower Coupon	14.65
2	Insert Shear Out	Lower Coupon, TLOW	14.14
3	Insert Shear Out	Lower Coupon, TLOW	12.93
4	Insert Shear Out	Lower Coupon, TLOW	12.92

Table 7-2: Test results

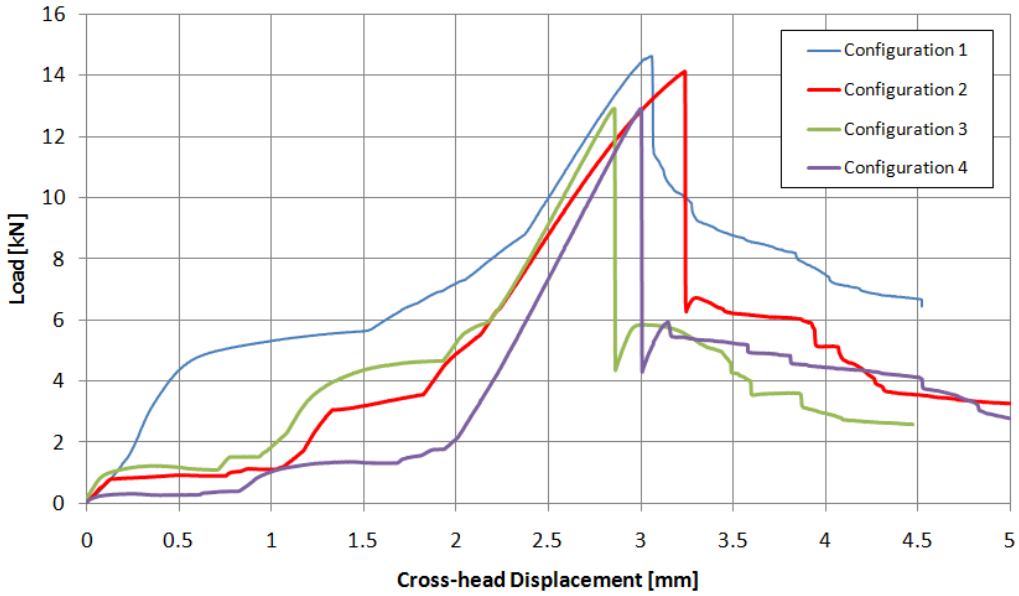

Figure 7-2: Load-displacement curves

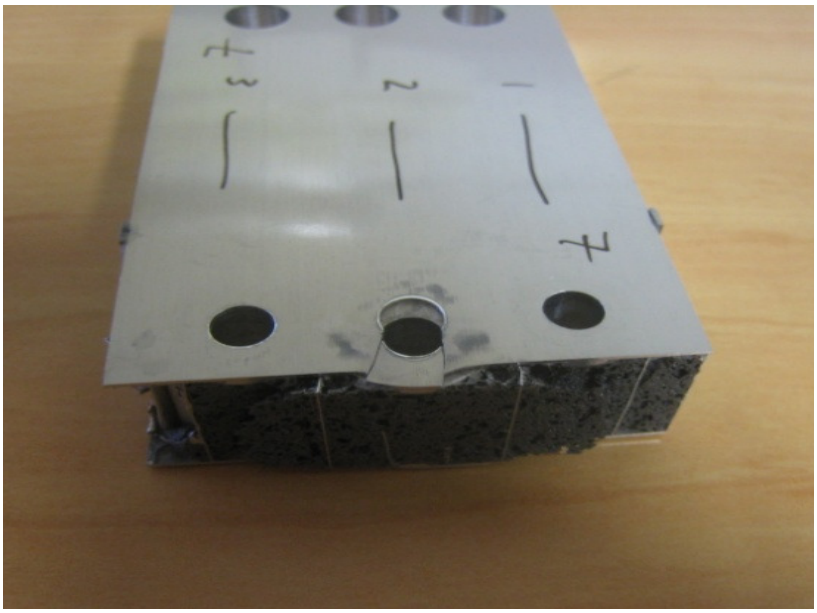

Figure 7-3: Image of one of the failed panel blocks

7.5 Insert Shear Out

From the above results it has been shown that in bearing mode the joint fails by insert shear out. For a hot bonded insert the shear out strength is mainly dependant on the shear strength of the bond with the two face sheets. The honeycomb core that surrounds the core is relatively weak under in-plane loads so its contribution to the shear strength of the insert can be considered negligible, especially if the insert is located along the edge of the panel. Ignoring the effect of the core it is straightforward to determine the theoretical shear strength of the insert based on the shear strength of the adhesive using the following simple expression

$$\boldsymbol{P_{Shear} = 2 \times A_{bob} \times \tau_{ad\ crit}} \quad \textbf{(7-1)}$$

where A_{bob} is the area of the bobbin insert in contact with one face sheet, and $\tau_{ad,crit}$ is the critical shear strength of the adhesive. For the panel blocks in question the adhesive film used to bond the face sheets was Redux 319L which has a quoted lap shear strength of 42 MPa. Based on the dimensions of the bobbin insert (major outer diameter of 16 mm with a central clearance hole 6.5 mm in diameter) the theoretical shear strength of the insert is 14.10 kN. This is very close to the peak loads obtained from the joint tests (see Table 7-2).

As the insert is sheared out from Figure 7-3 it can be seen that the fastener tears away a section of the face sheets. Hence it may be argued that the ultimate strength of the panel block is influenced by the face sheets; however, the bearing resistance of the face sheets alone is small compared to the shear strength of the insert. This can be easily demonstrated by considering the tear out stress on the face sheets resulting from a bearing load equivalent to the peak loads obtained from the tests. It is generally assumed that, for a metallic fitting that fails by tear out, the plug of material that the fastener tears out has a width corresponding to about 80 deg of the fastener hole [2] as shown in Figure 7-4. The shear area for the two skins given by

$$A_s = 4af \quad \textbf{(7-2)}$$

where *f* is the thickness of one face sheet. For the tested panel blocks *e* was equal to 6.8 mm and the face sheets were 0.56 mm thick. For a fastener bearing load of 14 kN this would give a shear stress over the area A_s equal to 615 MPa. This is significantly higher than the yield allowable for the face sheet material (~350 MPa), which suggest that as soon as the insert fails the fastener tears through the face sheets with little resistance.

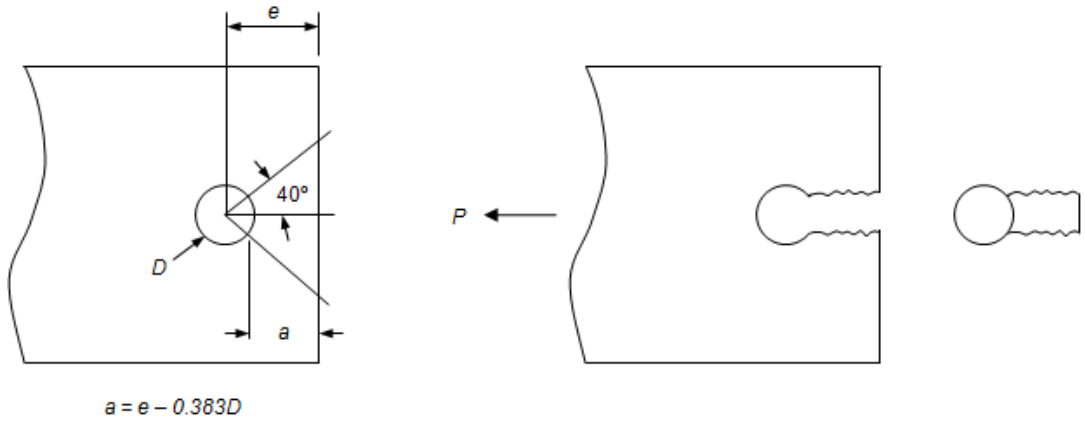

Figure 7-4: Shear tear out failure mode [2]

7.6 Conclusions

A series of tests were carried out to investigate the bearing strength of the panel joints tested for friction in Chapter 6. As was expected the joints all failed by insert shear out so the results provide useful data regarding the strength capability of the hot bonded inserts used in the panel blocks. The joints tested were only 4 but the variability in peak loads was relatively small, despite the fact that different configurations were tested. The different configurations only appeared to have an effect on the load-displacement curves prior to reaching the load maximums. From the curve for the first configuration were both sides of the joint were preloaded to a high level it can be clearly seen that the joint slips at a load that is significantly lower than the peak bearing load demonstrating that the friction grip joint is fail safe.

It was then shown how the based on the shear strength of the adhesive bond between the insert and the face sheets it is possible to determine the theoretical shear strength of the insert. Using the quoted shear strength of the film adhesive this was found to be in good agreement with the test results.

Chapter 8

8 Conclusions and Future Work

The use of honeycomb sandwich panel assemblies is an effective and cost efficient way of producing spacecraft structures, however, it poses several challenges and the techniques used to develop such structures generally rely heavily on design heritage and are far from optimal. Gaining a better understanding of the behavior of honeycomb sandwich structures, and the methods and solutions used to produce structural assemblies out of them is key in order to tackle the posed challenges and improve structural efficiency. This has been the primary focus of this work and, whether directly or indirectly, from the literature reviews it has been shown that there are still significant efforts ongoing in the relevant fields. Since the area of interest was very broad the research work had to be focused and prioritized on specific topics which, for practical applications, were considered of greater importance: honeycomb cores, equipment inserts, and bolted joints. In the thesis it has been shown that contributions have been made in each of these three areas. The main conclusions that can be extracted from the work carried out in these areas are summarized in the following subsections.

8.1 Honeycomb Core

An extensive test campaign was carried out to investigate the shear behavior of hexagonal honeycomb cores under both static and dynamic loads. A numerical investigation was also carried out using nonlinear finite element analysis to further study the effect of loading orientation on the static shear failure behavior of the tested honeycomb cores.

From the static tests it was found that the shear strength and the shear modulus have a non-linear relationship with loading orientation. Moreover it was found that the W orientation normal to the ribbon direction was not the weakest orientation, as is commonly assumed. This was also confirmed in the numerical study. Although

the observed differences (between the W and weaker orientations) were small this is significant since for design the shear strength values quoted for the W orientation are normally taken as the lowest. From the tests it was also observed that the shear strength only increases significantly when the loading orientation is decreased below 45deg, below which the increase rate grows until the maximum strength is reached at 0 deg when the load is aligned with the ribbon direction (i.e. the L orientation).

Using the finite element method it was determined that this non-linear relationship between loading orientation and shear behavior (modulus and strength) is due to the tendency of the core to also displace cross-axis with respect to the loading orientation when the load is not applied parallel to one of the principal orientations.

From the fatigue tests it was observed that in terms of load level (i.e. percentage of static ultimate strength) versus lifetime the core is actually more effective at resisting fatigue damage in the W orientation. By visual inspection of the failed specimens it was found that this may be attributed to the fact that crack propagation appears to be significantly inhibited by cell wall boundaries in the W orientation.

8.2 Equipment Inserts

This part of the work focused on gaining a better understanding of the insert systems used as load introduction points in honeycomb panels. An investigation was carried out to compare the structural performance of hot bonded inserts with cold bonded inserts. A significant part of the study was experimental and involved carrying out numerous insert pull-out tests to measure static pull strength capability. The obtained results were further investigated using the finite element method.

From the test campaign it was found that contrary to what would be normally expected cold bonded fully potted inserts can outperform hot bonded inserts in terms of static strength capability.

The results from the finite element study showed that the unexpectedly lower performance of the hot bonded inserts can be attributed to the stiffness of the filler material. The adhesive foam used as the filler material for the hot bonded inserts has a sensibly lower stiffness than the potting compound used in the cold bonded inserts and hence is less effective at transmitting external insert loads to the surrounding honeycomb core in an evenly distributed manner. For equal filler material stiffness the finite element results showed that the hot bonded insert design performs slightly better than the cold bonded fully potted design.

By comparing results from buckling theory on thin plates subject to uniform shear loads with the results obtained from the finite element model it was shown that when the insert is subject to high loads the inclined single thickness cell walls operate in a post-buckling regime from which recovery is still possible once the load is removed.

8.3 Bolted Joints

The final part of the thesis was devoted to the methods used to connect honeycomb panels to form spacecraft structural assemblies and focused on improving the efficiency of friction grip bolted joints. A simple method to analyze the efficiency of shear joint units was proposed.

A finite element analyses study was carried out to assess the stresses generated in the joint components under different loading conditions. From this investigation it was found that distributing the high clamping loads generated from bolt preload is one of the main challenges in achieving high efficiency joints.

An extensive test campaign was carried out to determine the friction coefficient values that can be expected from various materials, different surface treatments and the effect of surface reuse. From these tests it was found that the thick oxide layer present on the aluminium skins of the honeycomb panel significantly reduces the friction coefficient that can be achieved. The use of different cleat plate metallic materials was not found to have a significant effect on the friction coefficient.

Surface roughness had a significant effect on friction coefficient. Controlling the surface roughness of the faying surfaces is seen as the way forward for increasing the load carrying capability of joints in a repeatable and reliable manner.

A series of tests were also carried out to investigate the in-bearing strength capability of the bolted joints previously tested for friction. As expected all the joints failed by insert shear out so the tests provided useful and novel data regarding the shear strength of the hot bonded inserts used in the panel blocks. It was then found that the theoretical shear strength of the insert could be found based on the shear strength of the adhesive bond between the insert and the face sheets.

8.4 Future Work

From the above conclusions it can be seen how the work presented in this thesis has added to the current level of understanding of aluminium honeycomb sandwich panels and their use in spacecraft structures. However, as discussed above the field covered was very broad and there is still much work that could be done to build up on what has been achieved in this work. The following points, for each of the three major areas covered in the thesis, are seen as areas which could be further investigated.

<u>Honeycomb Core</u>

- From the finite element analysis it was determined that that the nonlinear relationship of core shear strength with loading orientation was due to the tendency of the core to displace off-axis when loaded at an angle. It would be interesting to verify this by using a test jig that constrains off-axis displacements.
- The research here only focused on aluminium hexagonal honeycomb cores; however, it may be interesting to carry out similar test campaigns on different types of cores.

Equipment Inserts

- Here equipment inserts were only investigated for static loads. It would also be interesting to study the fatigue performance of the tested hot bonded and cold bonded insert systems.
- In section 4.8 it was explained that the analytical model could not distinguish between hot bonded and cold bonded inserts because it assumes the insert system as a rigid disk. It would be interesting to modify the analytical model to also take into account the stiffness of the filler material.
- The finite element analysis used to model the insert systems was linear. Nonlinear finite element analysis could be used to model the failure processes of the tested insert systems.

Bolted Joints

- Here friction grip joints were only experimentally tested for static loads; however, it may also be interesting to investigate their performance under dynamic loads.
- An experimental study of other bolted joint configurations (e.g. corner joints) could be another topic for further investigation.
- In the literature review from section 5.2.3 the plasticity index and the adhesion parameter were found to be the two main parameters affecting the friction coefficient. It may be interesting to investigate the use of surface coatings and textures that could be used to control these parameters.

Appendix A: Publications

Journal Papers

Bianchi G., Aglietti G.S. and Richardson G. (2011) **Static Performance of Hot Bonded and Cold Bonded Inserts in Honeycomb Panels.** *Journal of Sandwich Structures and Materials*. Volume 13, Issue 1, pp. 59-82.

Bianchi G., Aglietti G.S. and Richardson G. (2011) **Static and Fatigue Behaviour of Hexagonal Honeycomb Cores under In-plane Shear Loads**, *Applied Composite Materials* (Accepted and in press, available online).

Conference Papers

Bianchi G., Aglietti G.S. and Richardson G. (2009) **Design of Optimized Shear bolted Joints Connecting Honeycomb Panels.** In, *The European Conference on Spacecraft Structures, Materials and Mechanical Testing (ECSSMMT), Toulouse, France, 15-17 Sep 2009*.

Bianchi G., Aglietti G.S. and Richardson G. (2009) **Experimental investigation of static and fatigue behavior of honeycomb panels under in-plane shear loads.** In, *50th AIAA/ASME/ASCE/AHS/ASC Structures, Structural Dynamics, and Materials Conference, California, USA, 4-7 May 2009*.

Bianchi G., Aglietti G.S. and Richardson G. (2008) **Static performance of hot bonded inserts in honeycomb panels.** In, *49thAIAA/ASME/ASCE/AHS/ASC Structures, Structural Dynamics, and Materials Conference, Schaumburg, USA, 7-10 Apr 2008*.

Bianchi G., Aglietti G.S. and Richardson G. (2007) **Optimization of bolted joints connecting honeycomb panels.** In, *1st CEAS,10th European Conference on Spacecraft Structures, Materials and Mechanical Testing, Berlin, Germany, 10-13 Sep 2007*.

Appendix B: Theoretical Pull-Out Strength of Inserts

From Ericksen [64] the distribution of shear stresses in the core of a circular sandwich panel normally loaded at a centrally located insert is given by

$$\tau(r)=\frac{PI_m}{\pi(h+c)I}\left\{\begin{array}{l}\left[\frac{1}{r}-\frac{I_1(\alpha r)}{ab}\times\left[\frac{bK_1(b)-aK_1(a)}{I_1(\alpha a)K_1(\alpha b)-I_1(\alpha b)K_1(\alpha a)}\right]\right]\\ \cdot\frac{K_1(\alpha r)}{ab}\left[\frac{bI_1(\alpha a)-aI_1(\alpha b)}{I_1(\alpha a)K_1(\alpha b)-I_1(\alpha b)K_1(\alpha a)}\right]\end{array}\right\} \qquad \text{(A1)}$$

where
- P = load applied at insert normal to facing plane
- c = core thickness
- f_1, f_2 = facing thicknesses; equal or unequal
- h = total sandwich thickness = $c + f_1 + f_2$
- a = outer radius of panel
- b = potting radius
- I_m* = moment of inertia of panel = $[f_1 f_2 (h + c)^2] / [4 (h-c)]$
- I_f* = moment of inertia of both facings = $(f_1^3 + f_2^3) / 12$
- I* = $I_f + I_m$
- α = $\sqrt{G_C (h - c) I / [E c f_1 f_2 I_f]}$
- E = $E_f / (1 - \upsilon_f^2)$
- $I_1(x)$, $K_1(x)$ = modified Bessel functions (x = αr, αa, αb)

For αr, αa and αb > 5 the modified Bessel functions become the exponential functions

$$I_1(x) = e^x(2\pi x)^{-1/2}$$

* Second moment of area per unit width [mm^3]

$$K_1(x) = -e^{-x}(\pi/2x)^{1/2} \tag{A.2}$$

Substituting Eqs. (A.2) into Eq. (A.1) gives

$$\tau(r) = \frac{PI_m}{\pi b(h+c)I} K \tag{A.3}$$

with
$$K = \frac{b}{r}\left[1 - \sqrt{r}\,\frac{\sqrt{b}\left(e^{\alpha(r-b)} - e^{-a(r-b)}\right) + \sqrt{a}\left(e^{\alpha(a-r)} - e^{-\alpha(a-r)}\right)}{\sqrt{ab}\left(e^{\alpha(a-b)} - e^{-\alpha(a-b)}\right)}\right] \tag{A.4}$$

For r < a, a good approximation for K is

$$K = \frac{b}{r}\left[1 - \sqrt{\frac{r}{b}}e^{\alpha(b-r)}\right] \tag{A.5}$$

For $f = f_1 = f_2$ it is possible to obtain

$I_m = f(c + f)^2/2$

$I_f = f^3/6$

$I = f(c^2/2 + cf + 2f^2 / 3)$

$$\alpha = \frac{1}{f}\sqrt{\frac{G_c}{E_f}12\left(1-\upsilon_f^2\right)(\beta/2+1+2/3\beta)} \tag{A.6}$$

$$\tau(r) = \frac{P\beta(\beta+1)}{2\pi bc\left(\beta^2+2\beta+4/3\right)} K \tag{A.7}$$

with $\beta=c/f$

If the core height is large compared to the thickness of the facings, Eq. (A6) and Eq. (A.7) can be approximated by

$$\alpha = \frac{1}{f}\sqrt{\frac{G_c}{E_f}12\left(1-\upsilon_f^2\right)(1+\beta/2)} \tag{A.8}$$

$$\tau(r) = \frac{P}{2\pi bc}\frac{\beta}{\beta+1}K \tag{A.9}$$

where P is the applied load, b is the potting radius and β is the ratio c/f. A good approximation for K is

$$K = \frac{b}{r}\left[1-\sqrt{\frac{r}{b}}e^{\alpha(b-r)}\right] \tag{A.10}$$

where α is a parameter that mainly controls the effect of bending of the face skins about their own middle plane upon the deflections and stresses in the sandwich and is given by

$$\alpha = \frac{1}{f}\sqrt{\frac{G_c}{E_f}12\left(1-\upsilon_f^2\right)(\beta/2+1+2/3\beta)} \tag{A.11}$$

where G_c is the shear modulus of the core, E_f is the Young's modulus of the facings and υ_f is the Poisson's ratio of the facings. In this approach the IDH refers to MIL-HDBK-23 A [113] for the position of the maximum core shear stress, $r_{\tau max}$, where it is demonstrated that

$$r_{\tau\max} = b/\left[1-e^{c_2(\alpha b)^n}\right] \tag{A.12}$$

with $c_2 = -0.931714$

$n = 0.262866$

The value of $r_{\tau\max}$ can be substituted into Eq. (A.10) to give $K_{\max}$ which in turn can be substituted into Eq. (A.11) to obtain

$$\tau_{\max} = \frac{P}{2\pi bc}\frac{\beta}{\beta+1}K_{\max} \quad \text{(A.13)}$$

or

$$\tau_{\max} = \frac{P}{2\pi bc}C^{*}K_{\max} \quad \text{(A.14)}$$

with $C^{*} = \beta/(\beta+1)$

If the failure mode is by shear rupture of the core then failure will occur when the load is such that τ_{max} exceeds the circular shear strength of the core τ_{Ccrit}. The above expression can be directly used to determine the insert capability by rearranging as follows

$$P_{crit} = \frac{2\pi bc\,\tau_{Ccrit}}{C^{*}K_{\max}} \quad \text{(A.15)}$$

Partially Potted Insert

For a partially potted insert in aluminium core the load applied to the insert consists of 3 parts:

i. P_F load applied to the upper facing

ii. P_S load part carried by shear stresses in the core around the potting

iii. P_N load part carried by normal stresses in the core underneath the potting

The above load components can be expressed as follows

$$\boldsymbol{P_F = (P_{\tau,max} - 2\pi r_{\tau,max} c\tau_{max})/2} \quad \text{(A.16)}$$

$$\boldsymbol{P_S = 2\pi r_{\tau,max} h_p \tau_{max}} \quad \text{(A.17)}$$

$$\boldsymbol{P_N = \pi r_{\tau,max}^2 \sigma_c} \quad \text{(A.18)}$$

where σ_c is the normal core stress underneath the insert, h_p is the potting height, $P_{\tau,max}$ is the load of an equivalent fully potted insert when $\tau=\tau_{max}$ and is given by

$$P_{\tau,max} = {}^{2\pi bc\tau_{max}}/_{C^*K_{max}}$$

which becomes $P_{c\ crit}$ for $\tau_{max}=\tau_{c\ crit}$.

Theoretically shear rupture of the core and tensile rupture of the core should not occur together; however, due to non-linearity effects $\tau_{C,crit}$ and $\sigma_{C,crit}$ are actually reached simultaneously. Hence the critical load components for a partially potted insert are

$$\boldsymbol{P_{F\,crit} = (P_{crit} - 2\pi r_{\tau,max} c\tau_{c\,crit})/2} \quad \text{(A.19)}$$

$$\boldsymbol{P_{S\,crit} = 2\pi r_{\tau,max} h_p \tau_{c\,crit}} \quad \text{(A.20)}$$

$$\boldsymbol{P_{N\,crit} = \pi r_{\tau,max}^2 \sigma_c} \quad \text{(A.21)}$$

Hence the capability of a partially potted insert is given by

$$P_{pcrit} = \frac{1}{2} P_{crit} + \pi r_{\tau\max} \left(2h_p - c\right) \tau_{C,crit} + \pi r_{\tau\max}^2 \sigma_{C,crit} \quad \text{(A.22)}$$

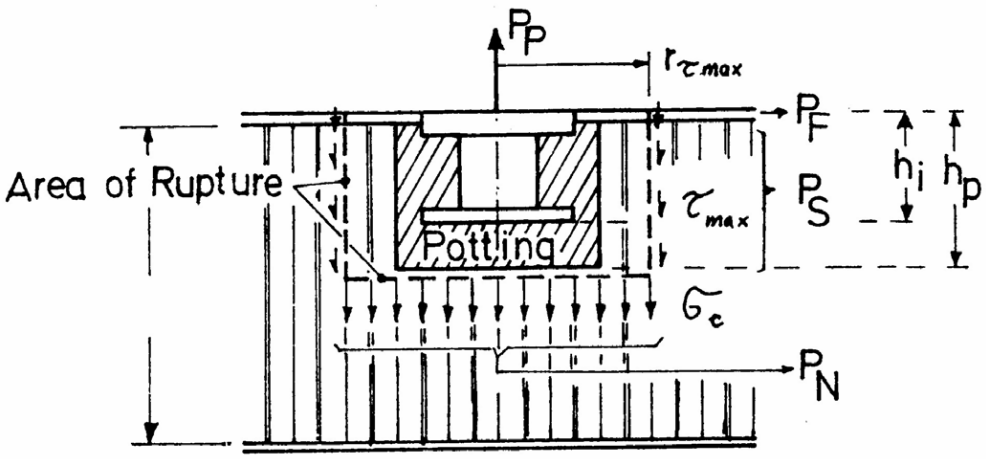

Figure A 1: Partially potted insert [35]

Partially Potted Insert in Heavy Aluminum Core

The external load PR applied to the insert can be split in three parts: (i) PF, part of load carried by the upper facing sheet; (ii) PSR, part of the load carried by shear stresses in the core around the potting over the insert height; (iii) PNR, part of the load carried by normal stresses in the potting underneath the insert. These can be expressed as follows:

$$P_F = \frac{1}{2}\left(P_R - 2\pi r_{\tau,\max} \cdot c \cdot \tau_{\max}\right) \tag{A.23}$$

$$P_{SR} = 2\pi r_{\tau,\max} \cdot h_i \cdot \tau_{\max} \tag{A.24}$$

$$P_{NR} = \pi \cdot b_R^2 \cdot \sigma_R \tag{A.25}$$

The total applied load is given by

$$P_R = P_F + P_{SR} + P_{NR} \tag{A.26}$$

P_{SR} can be expressed in terms of P_R by means of equation (A14) by rewriting as

$$P_R = 2\pi \cdot b \cdot c \cdot \frac{\tau_{\max}}{C^* \cdot K_{\max}} \tag{A.27}$$

which can be rewritten as

$$\tau_{\max} = P_R \cdot C^* \cdot K_{\max} \cdot \frac{1}{b \cdot c \cdot 2\pi} \tag{A.28}$$

substituting in equation (A.24) gives

$$P_{SR} = P_R \cdot C^* \cdot K_{\max} \cdot r_{\tau,\max} \cdot \frac{h_i}{b \cdot c} \tag{A.29}$$

then equation (A.26) can be rewritten as

$$P_R = \frac{1}{2} P_R \left(1 - C^* K_{\max} r_{\tau \max} \frac{1}{b} \right) + P_R \left(C^* K_{\max} r_{\tau \max} \frac{h_i}{b \cdot c} \right) + P_{NR} \tag{A.30}$$

The critical insert load under which the potting compound fails is then given by

$$P_{R,crit} = \frac{2 P_{NR,crit}}{1 + \frac{(c - 2h_i) r_{\tau,\max}}{cb} C^* K_{\max}} \tag{A.31}$$

where

$$P_{NR,crit} = \pi \cdot b_R^2 \cdot \sigma_{R,crit} \tag{A.32}$$

and $\sigma_{R,crit}$ is the tensile strength of the potting compound.

Appendix C: FE Joint Analysis Results

Configurations Tested

Configuration No.	Bolt Material	No. of Bolts	Bobbins Separation [mm]	Configuration Name
1	A2-70	2	1	Joint_s70_no2_sep1
2	A2-70	5	1	Joint_s70_no2_sep6
3	A2-70	2	6	Joint_s70_no5_sep1
4	A2-70	5	6	Joint_s70_no5_sep6
5	Ti	2	1	Joint_Ti_no2_sep1
6	Ti	5	1	Joint_Ti_no2_sep6
7	Ti	2	6	Joint_Ti_no5_sep1
8	Ti	5	6	Joint_Ti_no5_sep6

Table A 1: Tested configurations

Material Properties

Element	Aluminium Alloy	E [GPa]	Tensile Yield Stress [MPa]	Ultimate Tensile Stress [MPa]
Connecting Strip	7075	72	391	447
Aluminium Skin	2014	73	370	426
Bobbin Inserts	6082	72	398	475

Table A 2: Material properties of aluminium joint parts

Core Type	G [MPa]	v	E [MPa]	L Direction Shear Strength [MPa]	W Direction Shear Strength [MPa]
¼"-5056-0.0025"**	64.3	0.3	171.0	3.44	2.07

Table A 3: Material properties used for the honeycomb core (assumed isotropic)**

Safety Factors

FoS yield (FoSy)	FoS ultimate (FoSu)	FEA Factor (Km)
1.50	2.00	1.15

Table A 4: Factors of Safety

Margins of Safety

Margins of safety were calculated for the stress results obtained for the various joint components using equations A.33 – A.35 and the safety factors detailed in Table A 3. Yield and ultimate margins of safety values were calculated for the

aluminum joint elements using equations A.33 – A.34. For the honeycomb core a combined margin of safety was calculated through equation A.35 by using the maximum shear stress results in the XZ and YZ planes and the circular core shear stress allowable, $\tau_{C,crit}$, which can be calculated from the shear strength in the W direction via Eq. **4-4** in section 4.7.

$$MoS_y = \frac{\sigma_y}{\sigma \times FoS_y \times Km} - 1 \quad \text{(A.33)}$$

$$MoS_u = \frac{\sigma_u}{\sigma \times FoS_u \times Km} - 1 \quad \text{(A.34)}$$

$$MoS_C = \frac{\tau_{C,crit}}{((\tau_{XZ}+\tau_{YZ})/2) \times FoS_u \times Km} - 1 \quad \text{(A.35)}$$

Joint_s70_no2_sep1		IN-PLANE TENSION		IN-PLANE COMPRESSION		IN-PLANE SHEAR		OUT-OF-PLANE SHEAR		OUT-OF-PLANE BENDING	
		Max Preload	Min Preload	Max Preload	Min Preload	Max Preload	Min Preload	Max Preload	Min Preload	Max Preload	Min Preload
Bolt Preload [kN]		9.74	6.09	9.74	6.09	9.74	6.09	9.74	6.09	9.74	6.09
External Force Fq [kN]		21.31	21.31	21.31	21.31	21.31	21.31	3.26	3.26	-	-
External Moment Mq [Nm]		-	-	-	-	-	-	-	-	213.07	213.07
RESULTS											
Part	**Result**										
All	Max Stress [MPa]	167.6	133.8	188	133.1	194	190	757.2	752.5	183.2	129.3
	Location	Strips	Strips	Strips	Strips	Strips	Strips	Strips	Strips	Strips	Strips
Strips	Max Stress [MPa]	167.6	133.8	188	133.1	194	190	757.2	752.5	183.2	129.3
	MoSy	0.35	0.69	0.21	0.70	0.17	0.19	-0.70	-0.70	0.24	0.75
	MoSu	0.16	0.45	0.03	0.46	0.00	0.02	-0.74	-0.74	0.06	0.50
Skins	Max Stress [MPa]	104.5	104.5	111.8	109.8	104	102	241.5	242.1	112.7	112.5
	MoSy	1.17	1.17	1.03	1.06	1.18	1.22	-0.06	-0.06	1.01	1.01
	MoSu	0.86	0.86	0.74	0.77	0.87	0.91	-0.20	-0.20	0.72	0.73
Bobbins	Max Stress [MPa]	141.5	108	122.4	107.4	132.5	91.46	240.5	236.5	136.2	99.79
	MoSy	0.60	1.10	0.85	1.11	0.71	1.48	-0.06	-0.04	0.66	1.27
	MoSu	0.37	0.80	0.59	0.81	0.47	1.12	-0.19	-0.18	0.43	0.95
Core	Max Shear Stress [MPa]										
	YZ Plane	0.98	1.09	1.68	1.54	0.77	0.69	0.80	7.25	0.78	0.52
	XZ Plane	0.68	0.43	1.13	0.87	1.44	1.28	0.74	2.47	1.31	1.23
	MoSc	0.47	0.61	-0.13	0.02	0.11	0.24	0.59	-0.75	0.17	0.40

Table A 5: Configuration 1 Results

Joint_s70_no2_sep6		IN-PLANE TENSION		IN-PLANE COMPRESSION		IN-PLANE SHEAR		OUT-OF-PLANE SHEAR		OUT-OF-PLANE BENDING	
		Max Preload	Min Preload	Max Preload	Min Preload	Max Preload	Min Preload	Max Preload	Min Preload	Max Preload	Min Preload
Bolt Preload [kN]		9.74	6.09	9.74	6.09	9.74	6.09	9.74	6.09	9.74	6.09
External Force Fq [kN]		21.31	21.31	21.31	21.31	21.31	21.31	3.26	3.26	-	-
External Moment Mq [Nm]		-	-	-	-	-	-	-	-	213.07	213.07
RESULTS											
Part	**Result**										
All	Max Stress [MPa]	165.9	121.8	172.4	124.7	159	157	599.8	593.3	170.7	124
	Location	Strips	Strips	Strips	Strips	Strips	Strips	Strips	Strips	Strips	Strips
Strips	Max Stress [MPa]	165.9	121.8	172.4	124.7	159	157	599.8	593.3	170.7	124
	MoSy	0.37	0.86	0.31	0.82	0.43	0.44	-0.62	-0.62	0.33	0.83
	MoSu	0.17	0.60	0.13	0.56	0.22	0.24	-0.68	-0.67	0.14	0.57
Skins	Max Stress [MPa]	95.02	94.99	101.5	99.6	98.1	97.9	242.8	245.3	103.9	103.8
	MoSy	1.39	1.39	1.23	1.28	1.31	1.32	-0.07	-0.08	1.18	1.18
	MoSu	1.05	1.05	0.91	0.95	0.98	0.99	-0.20	-0.21	0.87	0.87
Bobbins	Max Stress [MPa]	138.1	97.28	125	89.83	127	87.33	276.6	237.6	130.3	95.73
	MoSy	0.64	1.33	0.81	1.52	0.78	1.60	-0.18	-0.05	0.74	1.37
	MoSu	0.41	1.00	0.55	1.16	0.53	1.23	-0.30	-0.18	0.49	1.03
Core	Max Shear Stress [MPa]										
	YZ Plane	0.96	1.08	1.47	1.30	0.95	0.62	4.80	4.77	0.81	0.49
	XZ Plane	0.73	0.49	1.03	0.77	1.33	1.17	2.95	2.75	1.14	1.11
	MoSc	0.45	0.57	-0.02	0.18	0.08	0.37	-0.68	-0.67	0.25	0.53

Table A 6: Configuration 2 Results

Joint_s70_no5_sep1		IN-PLANE TENSION		IN-PLANE COMPRESSION		IN-PLANE SHEAR		OUT-OF-PLANE SHEAR		OUT-OF-PLANE BENDING	
		Max Preload	Min Preload	Max Preload	Min Preload	Max Preload	Min Preload	Max Preload	Min Preload	Max Preload	Min Preload
Bolt Preload [kN]		9.74	6.09	9.74	6.09	9.74	6.09	9.74	6.09	9.74	6.09
External Force Fq [kN]		21.31	21.31	21.31	21.31	21.31	21.31	3.26	3.26	-	-
External Moment Mq [Nm]		-	-	-	-	-	-	-	-	213.07	213.07
RESULTS											
Part	**Result**										
All	Max Stress [MPa]	202.9	176.8	190.3	153.1	194	193	501.8	498.2	177.1	148.7
	Location	Strips	Strips	Strips	Strips	Skins	Skins	Strips	Strips	Skins	Skins
Strips	Max Stress [MPa]	202.9	176.8	190.3	153.1	193	191	501.8	498.2	177.1	132.5
	MoSy	0.12	0.28	0.19	0.48	0.17	0.19	-0.55	-0.55	0.28	0.71
	MoSu	-0.04	0.10	0.02	0.27	0.01	0.02	-0.61	-0.61	0.10	0.47
Skins	Max Stress [MPa]	145.6	145.2	150.9	149.5	194	193	292.9	291.6	149.8	148.7
	MoSy	0.56	0.56	0.50	0.52	0.17	0.17	-0.23	-0.22	0.51	0.52
	MoSu	0.33	0.34	0.29	0.30	0.00	0.01	-0.34	-0.33	0.30	0.31
Bobbins	Max Stress [MPa]	151.9	135.6	134.7	133.8	159.8	159.5	258.1	256.9	137.3	125.2
	MoSy	0.49	0.67	0.68	0.69	0.42	0.42	-0.12	-0.12	0.65	0.81
	MoSu	0.28	0.43	0.44	0.45	0.22	0.22	-0.25	-0.24	0.42	0.55
Core	Max Shear Stress [MPa]										
	YZ Plane	1.53	1.59	2.00	1.88	1.17	1.15	4.54	4.25	0.96	0.90
	XZ Plane	0.66	0.61	1.22	0.91	1.79	1.78	2.95	2.72	1.96	1.95
	MoSc	0.12	0.11	-0.24	-0.12	-0.17	-0.16	-0.67	-0.65	-0.16	-0.14

Table A 7: Configuration 3 Results

Joint_s70_no5_sep6		IN-PLANE TENSION		IN-PLANE COMPRESSION		IN-PLANE SHEAR		OUT-OF-PLANE SHEAR		OUT-OF-PLANE BENDING	
		Max Preload	Min Preload	Max Preload	Min Preload	Max Preload	Min Preload	Max Preload	Min Preload	Max Preload	Min Preload
Bolt Preload [kN]		9.74	6.09	9.74	6.09	9.74	6.09	9.74	6.09	9.74	6.09
External Force Fq [kN]		21.31	21.31	21.31	21.31	21.31	21.31	3.26	3.26	-	-
External Moment Mq [Nm]		-	-	-	-	-	-	-	-	213.07	213.07
RESULTS											
Part	**Result**										
All	Max Stress [MPa]	173	148.4	168.8	159	256.8	256.3	395.5	394	176.2	147.4
	Location	Strips	Strips	Strips	Strips	Skins	Skins	Strips	Strips	Strips	Strips
Strips	Max Stress [MPa]	173	148.4	168.8	159	156	150	395.5	394	176.2	147.4
	MoSy	0.31	0.53	0.34	0.43	0.45	0.51	-0.43	-0.42	0.29	0.54
	MoSu	0.12	0.31	0.15	0.22	0.25	0.30	-0.51	-0.51	0.10	0.32
Skins	Max Stress [MPa]	137.4	136.3	140.6	139.5	172	172	271	270.7	136.6	134.9
	MoSy	0.65	0.66	0.61	0.62	0.32	0.32	-0.16	-0.16	0.66	0.68
	MoSu	0.41	0.43	0.38	0.39	0.13	0.13	-0.28	-0.28	0.42	0.44
Bobbins	Max Stress [MPa]	146.8	117.2	125.9	119.5	135.5	135.2	238.4	232	142.6	111.4
	MoSy	0.54	0.93	0.80	0.90	0.67	0.68	-0.05	-0.02	0.59	1.03
	MoSu	0.32	0.66	0.54	0.63	0.43	0.44	-0.18	-0.16	0.36	0.74
Core	Max Shear Stress [MPa]										
	YZ Plane	1.28	1.38	1.68	1.57	1.06	0.98	4.23	3.99	0.90	0.81
	XZ Plane	0.74	0.53	1.04	0.80	1.48	1.38	2.47	2.26	1.70	1.60
	MoSc	0.21	0.28	-0.10	0.03	-0.04	0.04	-0.63	-0.61	-0.06	0.02

Table A 8: Configuration 4 Results

Joint_Ti_no2_sep1		IN-PLANE TENSION		IN-PLANE COMPRESSION		IN-PLANE SHEAR		OUT-OF-PLANE SHEAR		OUT-OF-PLANE BENDING	
		Max Preload	Min Preload	Max Preload	Min Preload	Max Preload	Min Preload	Max Preload	Min Preload	Max Preload	Min Preload
Bolt Preload [kN]		9.74	6.09	9.74	6.09	9.74	6.09	9.74	6.09	9.74	6.09
External Force Fq [kN]		21.31	21.31	21.31	21.31	21.31	21.31	3.26	3.26	-	-
External Moment Mq [Nm]		-	-	-	-	-	-	-	-	213.07	213.07
RESULTS											
Part	**Result**										
All	Max Stress [MPa]	234.4	189.5	242.7	174.6	194	190	1340	1324	235.6	168.3
	Location	Strips	Strips	Strips	Strips	Strips	Strips	Strips	Strips	Strips	Strips
Strips	Max Stress [MPa]	234.4	189.5	242.7	174.6	267	265	1340	1324	235.6	168.3
	MoSy	-0.03	0.20	-0.07	0.30	-0.15	-0.14	-0.83	-0.83	-0.04	0.35
	MoSu	-0.17	0.03	-0.20	0.11	-0.27	-0.27	-0.85	-0.85	-0.18	0.15
Skins	Max Stress [MPa]	148.6	148.5	159.3	156.3	142	139	301.4	303.4	164.1	163.7
	MoSy	0.53	0.53	0.42	0.45	0.60	0.63	-0.25	-0.25	0.38	0.38
	MoSu	0.31	0.31	0.22	0.24	0.37	0.40	-0.36	-0.36	0.18	0.19
Bobbins	Max Stress [MPa]	193.3	140.3	152.4	133.5	182.8	127.6	253.4	212.5	182.2	142.6
	MoSy	0.17	0.62	0.49	0.70	0.24	0.78	-0.11	0.07	0.24	0.59
	MoSu	0.01	0.39	0.28	0.46	0.06	0.52	-0.23	-0.09	0.07	0.36
Core	Max Shear Stress [MPa]										
	YZ Plane	1.19	1.18	1.90	1.74	1.13	1.10	7.55	7.63	0.86	0.85
	XZ Plane	0.70	0.53	1.29	1.00	1.94	1.70	3.50	3.25	1.88	1.82
	MoSc	0.30	0.43	-0.23	-0.11	-0.20	-0.13	-0.78	-0.78	-0.11	-0.08

Table A 9: Configuration 5 Results

Joint_Ti_no2_sep6		IN-PLANE TENSION		IN-PLANE COMPRESSION		IN-PLANE SHEAR		OUT-OF-PLANE SHEAR		OUT-OF-PLANE BENDING	
		Max Preload	Min Preload	Max Preload	Min Preload	Max Preload	Min Preload	Max Preload	Min Preload	Max Preload	Min Preload
Bolt Preload [kN]		9.74	6.09	9.74	6.09	9.74	6.09	9.74	6.09	9.74	6.09
External Force Fq [kN]		21.31	21.31	21.31	21.31	21.31	21.31	3.26	3.26	-	-
External Moment Mq [Nm]		-	-	-	-	-	-	-	-	213.07	213.07
RESULTS											
Part	**Result**										
All	Max Stress [MPa]	233.6	170.6	258.6	177.9	226	224	258.3	165.3	229.9	162.2
	Location	Strips	Strips	Strips	Strips	Strips	Strips	Strips	Strips	Strips	Strips
Strips	Max Stress [MPa]	233.6	170.6	258.6	177.9	226	224	258.3	165.3	229.9	162.2
	MoSy	-0.03	0.33	-0.12	0.27	0.00	0.01	-0.12	0.37	-0.01	0.40
	MoSu	-0.17	0.14	-0.25	0.09	-0.14	-0.13	-0.25	0.18	-0.15	0.20
Skins	Max Stress [MPa]	137.9	137.7	148	145.1	137	135	84.87	79.74	149.9	149.8
	MoSy	0.64	0.65	0.53	0.56	0.65	0.68	1.67	1.84	0.51	0.51
	MoSu	0.41	0.41	0.31	0.34	0.42	0.44	1.29	1.44	0.30	0.30
Bobbins	Max Stress [MPa]	187.6	134.1	157.4	130.5	155	119	152.1	126.2	183.1	132.3
	MoSy	0.21	0.69	0.44	0.74	0.46	0.90	0.49	0.80	0.24	0.71
	MoSu	0.04	0.45	0.23	0.49	0.25	0.63	0.28	0.54	0.06	0.47
Core	Max Shear Stress [MPa]										
	YZ Plane	1.09	1.10	1.99	1.80	1.13	0.87	19.55	17.55	0.97	0.60
	XZ Plane	0.86	0.52	1.23	0.89	1.68	1.49	15.23	10.91	1.74	1.68
	MoSc	0.26	0.51	-0.24	-0.09	-0.13	0.04	-0.93	-0.91	-0.10	0.07

Table A 10: Configuration 6 Results

Joint_Ti_no5_sep1		IN-PLANE TENSION		IN-PLANE COMPRESSION		IN-PLANE SHEAR		OUT-OF-PLANE SHEAR		OUT-OF-PLANE BENDING	
		Max Preload	Min Preload	Max Preload	Min Preload	Max Preload	Min Preload	Max Preload	Min Preload	Max Preload	Min Preload
Bolt Preload [kN]		9.74	6.09	9.74	6.09	9.74	6.09	9.74	6.09	9.74	6.09
External Force Fq [kN]		21.31	21.31	21.31	21.31	21.31	21.31	3.26	3.26	-	-
External Moment Mq [Nm]		-	-	-	-	-	-	-	-	213.07	213.07
RESULTS											
Part	**Result**										
All	Max Stress [MPa]	256	236.1	270.5	211.8	177.9	167.9	258.3	165.3	256.1	203.9
	Location	Strips	Strips	Strips	Strips	Strips	Skins	Strips	Strips	Strips	Skins
Strips	Max Stress [MPa]	256	236.1	270.5	211.8	260	257	258.3	165.3	256.1	190.6
	MoSy	-0.11	-0.04	-0.16	0.07	-0.13	-0.12	-0.12	0.37	-0.11	0.19
	MoSu	-0.24	-0.18	-0.28	-0.08	-0.25	-0.24	-0.25	0.18	-0.24	0.02
Skins	Max Stress [MPa]	200	198.4	207.7	205.4	280	279	84.87	79.74	202.3	203.9
	MoSy	0.13	0.14	0.09	0.10	-0.19	-0.19	1.67	1.84	0.12	0.11
	MoSu	-0.03	-0.02	-0.06	-0.05	-0.31	-0.30	1.29	1.44	-0.04	-0.05
Bobbins	Max Stress [MPa]	205	177.4	190.3	184.7	232.5	227.9	152.1	126.2	196.9	181
	MoSy	0.11	0.28	0.19	0.23	-0.03	-0.01	0.49	0.80	0.15	0.25
	MoSu	-0.05	0.10	0.02	0.05	-0.16	-0.15	0.28	0.54	-0.01	0.07
Core	Max Shear Stress [MPa]										
	YZ Plane	1.88	2.04	2.35	2.24	1.67	1.69	19.55	17.55	1.25	1.20
	XZ Plane	0.99	0.77	1.72	1.22	3.06	3.01	15.23	10.91	2.76	2.74
	MoSc	-0.15	-0.13	-0.40	-0.29	-0.48	-0.48	-0.93	-0.91	-0.39	-0.38

Table A 11: Configuration 7 Results

Joint_Ti_no5_sep6		IN-PLANE TENSION		IN-PLANE COMPRESSION		IN-PLANE SHEAR		OUT-OF-PLANE SHEAR		OUT-OF-PLANE BENDING	
		Max Preload	Min Preload	Max Preload	Min Preload	Max Preload	Min Preload	Max Preload	Min Preload	Max Preload	Min Preload
Bolt Preload [kN]		9.74	6.09	9.74	6.09	9.74	6.09	9.74	6.09	9.74	6.09
External Force Fq [kN]		21.31	21.31	21.31	21.31	21.31	21.31	3.26	3.26	-	-
External Moment Mq [Nm]		-	-	-	-	-	-	-	-	213.07	213.07
RESULTS											
Part	**Result**										
All	Max Stress [MPa]	268.6	220.8	256.1	198.8	250	239	258.3	165.3	264	183
	Location	Strips	Strips	Strips	Strips	Strips	Skins	Strips	Strips	Strips	Skins
Strips	Max Stress [MPa]	268.6	220.8	256.1	198.8	250	187	250	165.3	264	182.2
	MoSy	-0.16	0.03	-0.11	0.14	-0.09	0.21	-0.09	0.37	-0.14	0.24
	MoSu	-0.28	-0.12	-0.24	-0.02	-0.22	0.04	-0.22	0.18	-0.26	0.07
Skins	Max Stress [MPa]	179	177.8	186.9	184.7	239	239	84.87	79.74	184.5	183
	MoSy	0.27	0.27	0.21	0.23	-0.05	-0.05	1.67	1.84	0.23	0.24
	MoSu	0.09	0.09	0.04	0.05	-0.19	-0.19	1.29	1.44	0.05	0.06
Bobbins	Max Stress [MPa]	199.9	159.5	164.9	161.7	190.5	182.3	152.1	126.2	195.1	151.5
	MoSy	0.13	0.42	0.37	0.40	0.19	0.24	0.49	0.80	0.16	0.50
	MoSu	-0.03	0.22	0.18	0.20	0.02	0.07	0.28	0.54	0.00	0.28
Core	Max Shear Stress [MPa]										
	YZ Plane	1.60	1.58	2.28	2.16	1.40	1.22	19.55	17.55	1.11	1.06
	XZ Plane	0.89	0.70	1.41	1.12	2.13	1.96	15.23	10.91	2.33	2.28
	MoSc	-0.02	0.08	-0.34	-0.25	-0.31	-0.23	-0.93	-0.91	-0.29	-0.27

Table A 12: Configuration 8 Results

Appendix D: Campaign 1 Friction Test Results

NON-ABRADED TESTS

VIRGIN				
	Slip Load [N]		Fiction Coefficient	
Test No.	Initial	Nominal	Initial	Nominal
Test 1	3252	4173	0.217	0.278
Test 2	2520	3925	0.168	0.262
Test 3	1690	3575	0.113	0.238
		Avg.	**0.166**	**0.259**
REUSE 1				
	Slip Load [N]		Fiction Coefficient	
Test No.	Initial	Nominal	Initial	Nominal
Test 1	2150	4344	0.143	0.290
Test 2	2080	4263	0.139	0.284
Test 3	2000	3790	0.133	0.253
		Avg.	**0.138**	**0.275**
REUSE 2				
	Slip Load [N]		Fiction Coefficient	
Test No.	Initial	Nominal	Initial	Nominal
Test 1	2000	3805	0.133	0.254
Test 2	2320	4357	0.155	0.290
Test 3	1900	3865	0.127	0.258
		Avg.	**0.138**	**0.267**

Table A 13: Al-Al configuration friction test results

VIRGIN				
	Slip Load [N]		Fiction Coefficient	
Test No.	Initial	Nominal	Initial	Nominal
Test 1	1850	3725	0.123	0.248
Test 2	2050	3847	0.137	0.256
Test 3	1970	3515	0.131	0.234
		Avg.	**0.130**	**0.246**
REUSE 1				
	Slip Load [N]		Fiction Coefficient	
Test No.	Initial	Nominal	Initial	Nominal
Test 1	1950	3782	0.130	0.252
Test 2	1920	4108	0.128	0.274
Test 3	2820	3801	0.188	0.253
		Avg.	**0.149**	**0.260**
REUSE 2				
	Slip Load [N]		Fiction Coefficient	
Test No.	Initial	Nominal	Initial	Nominal
Test 1	1930	4112	0.129	0.274
Test 2	1610	3753	0.107	0.250
Test 3	1500	3930	0.100	0.262
		Avg.	**0.112**	**0.262**

Table A 14: Al-Ti configuration friction test results

VIRGIN				
	Slip Load [N]		Fiction Coefficient	
Test No.	Initial	Nominal	Initial	Nominal
Test 1*	-	3700	-	0.247
Test 2	2450	3944	0.163	0.263
Test 3	2200	3813	0.147	0.254
		Avg.	**0.155**	**0.255**
REUSE 1				
	Slip Load [N]		Fiction Coefficient	
Test No.	Initial	Nominal	Initial	Nominal
Test 1	2000	4618	0.133	0.308
Test 2	2310	4206	0.154	0.280
Test 3	1600	3759	0.107	0.251
		Avg.	**0.131**	**0.280**
REUSE 2				
	Slip Load [N]		Fiction Coefficient	
Test No.	Initial	Nominal	Initial	Nominal
Test 1	2170	4777	0.145	0.318
Test 2	3050	4593	0.203	0.306
Test 3	1500	4391	0.100	0.293
		Avg.	**0.149**	**0.306**

Table A 15: Al-Clad configuration friction test results (*Initial slip value missing due to extensometer slip)

ABRADED TESTS

VIRGIN				
	Slip Load [N]		Fiction Coefficient	
Test No.	Initial	Nominal	Initial	Nominal
Test 1	3045	8024	0.203	0.535
Test 2	3215	7527	0.214	0.502
Test 3	3104	7730	0.207	0.515
		Avg.	**0.209**	**0.518**
REUSE 1				
	Slip Load [N]		Fiction Coefficient	
Test No.	Initial	Nominal	Initial	Nominal
Test 1	2825	6718	0.188	0.448
Test 2	2853	7012	0.190	0.467
Test 3	2910	7132	0.194	0.475
		Avg.	**0.189**	**0.458**

Table A 16: Alabr-Alabr configuration friction test results

VIRGIN				
	Slip Load [N]		Fiction Coefficient	
Test No.	Initial	Nominal	Initial	Nominal
Test 1	4250	8933	0.283	0.596
Test 2	3914	8827	0.261	0.588
Test 3	3852	8660	0.257	0.577
		Avg.	**0.267**	**0.587**
REUSE 1				
	Slip Load [N]		Fiction Coefficient	
Test No.	Initial	Nominal	Initial	Nominal
Test 1	3204	7232	0.214	0.482
Test 2	3054	7226	0.204	0.482
Test 3	2950	6162	0.197	0.411
		Avg.	**0.209**	**0.482**

Table A 17: Alabr-Tiabr configuration friction test result

References

1. Chmielewski A.B., Das A., Cassapakis C., Allen D., Shafer W.J., Sarcel J., et al. *New millenium power technology*. 1996 Aug 11-1996 Aug 16.

2. Sarafin P.T. *Spacecraft Structures and Mechanisms: From Concept to Launch*. Microcosm Press, Kluwer Academic Publishers; 2011.

3. Wijker J.J. *Spacecraft Structures*. Springer; 2008.

4. Wijker J.J. *Random Vibrations in Spacecraft Structures Design: Theory and Applications*. Springer; 2009.

5. Plantema F.J. *Sandwich Construction*. Wiley & Sons; 1966.

6. Bruhn E.F. *Analysis and Design of Flight Vehicle Structures*. Jacobs Publishing; 1973.

7. Wang R. *Modelling of Spacecraft Structures Incorporating Damped Bolted Joints* University of Surrey; 2005.

8. Amontons G. *Remarques et expériences physiques sur la construction d'une nouvelle clepsydre*. 1695. Paris.

9. *Composite Design Handbook. ESA PSS-03-203*. 1986. European Space Agency.

10. *ASTM C273. Standard test method for shear properties of sandwich core materials*. 1970. ASTM Committee C19 on Structural Sandwich Construction.

11. *ASTM C394. Standard test method for shear fatigue of sandwich core materials*. 1974. ASTM Committee C19 on Structural Sandwich Construction.

12. Allen H.G. *Analysis and design of structural sandwich panels*. London: Pargamon Press; 1969.

13. Marshall A. *Sandwich Construction. Handbook of Composites*. 557-601. 1982. New York, Van Nostrand Reinhold.

14. Zenkert D. *An introduction to sandwich construction*. Solihull; 1995.

15. Vinson J.R. *The behavior of sandwich structures of isotropic and composite materials*. Technomic Pub. Co.; 1999.

16. Noor A.K., Burton W.S., Bert C.W. *Computational Models for Sandwich Panels and Shells*. Applied Mechanics Reviews 1996 Mar;49(3):155-199.

17. Hohe J. and Becker W. *Effective stress-strain relations for two-dimensional cellular sandwich cores: Homogenization, material models, and properties*. Applied Mechanics Reviews 2002 Jan;55(1):61-87.

18. Schwingshackl C.W., Aglietti G.S., Cunningham P.R. *Detrmination of Honeycomb Material Properties: Existing Theories and an Alternative Dynamic Approach*. Journal of Aerospace Engineering 2006 Jul;19(3):177-183.

19. Gibson L.J. and Ashby M.F. *Cellular Solids: Structures and Properties*. 2nd ed. Cambridge University Press; 1997.

20. Masters I.G. and Evans K.E. *Models for the elastic deformation of honeycombs*. Composite Structures 1996 Aug;35(4):403-422.

21. Becker W. *Closed-form analysis of the thickness effect of regular honeycomb core material*. Composite Structures 2001 Jan;48(1-3):67-70.

22. Kelsey S., Gallatly R.A., Clark B.W. *The shear modulus of foil honeycomb core*. Aircraft Engineering 1958;30:294-302.

23. Shames D. *Solid Mechanics. A Variational Approach*. New York: McGraw-Hill; 1973.

24. Grediac M. *A finite element study of the transverse shear in honeycomb cores*. International Journal of Solids and Structures 1993;30(13):1777-1788.

25. Meraghni F., Desrumaux F., Benzeggagh M.L. *Mechanical behaviour of cellular core for structural sandwich panels*. Composites Part A: Applied Science and Manufacturing 1999 Jun;30(6):767-779.

26. Heimbs S. *Virtual testing of sandwich core structures using dynamic finite element simulations*. Computational Materials Science 2009 Apr;45(2):205-216.

27. Lee H.S., Hong S.H., Lee J.R., Kim Y.K. *Mechanical behavior and failure process during compressive and shear deformation of honeycomb composite at elevated temperatures*. Journal of Materials Science 2002 Mar 21;37(6):1265-1272.

28. Pan S.D., Wu L.Z., Sun Y.G., Zhou Z.G., Qu J.L. *Longitudinal shear strength and failure process of honeycomb cores*. Composite Structures 2006 Jan;72(1):42-46.

29. Belouettar S., Abbadi A., Azari Z., Belouettar R., Freres P. *Experimental investigation of static and fatigue behaviour of composites honeycomb materials using four point bending tests*. Composite Structures 2009 Feb;87(3):265-273.

30. Hwang W. and Han K.S. *Fatigue of composites fatigue modulus concept and life prediction*. Journal of Composite Materials 1986;20:155-165.

31. Miner M. *Cumulative damage in fatigue*. Journal of Applied Mechanics Part A 1945;159-164.

32. Belingardi G., Martella P., Peroni L. *Fatigue analysis of honeycomb-composite sandwich beams*. Composites Part A: Applied Science and Manufacturing 2007 Apr;38(4):1183-1191.

33. Demelio G., Genovese K., Pappalettere C. *An experimental investigation of static and fatigue behaviour of sandwich composite panels joined by fasteners*. Composites Part B: Engineering 2001;32(4):299-308.

34. Heimbs S. and Pein M. *Failure behaviour of honeycomb sandwich corner joints and inserts*. Composite Structures 2009 Aug;89(4):575-588.

35. *Insert Design Handbook. ESA PSS-03-1202*. [1]. 1987. European Space Agency.

36. Norris C. *An analysis of the compressive strength of honeycomb cores for sandwich constructions*. National Advisory Committee for Aeronautics; 1947. Report No.: NACA TN-1251.

37. Ringelstetter L., Voss A., Norris C. *Effect of cell shape on compressive strength of hexagonal honeycomb structures*. National Advisory Committee for Aeronautics; 1950. Report No.: NACA TN-2243.

38. Warren F., Norris C. *Analysis of shear strength of honeycomb cores for sandwich construction*. National Advisory Committee for Aeronautics; 1950. Report No.: NACA TN-2208.

39. *ASTM C297. Standard Test Method for Flatwise Tensile Strength of Sandwich Constructions*. 1984. ASTM Committee C19 on Structural Sandwich Construction.

40. Guo X.E. and Gibson L.J. *Behavior of intact and damaged honeycombs: a finite element study*. International Journal of Mechanical Sciences 1999 Jan;41(1):85-105.

41. Chamis C. and Aiello R. *Fibre composite sandwich thermostructural behavior*. J Compos Technol Res 1988;10(3):93-99.

42. Allegri G., Lecci U., Marchetti M., Poscente F. *FEM simulation of the mechanical behavior of sandwich materials for aerospace structures*. Key Engineering Materials 2002;221-222.

43. Aminanda Y., Castanie B., Barrau J., Thevenet P. *Experimental Analysis and Modeling of the Crushing of Honeycomb Cores*. Applied Composite Materials 2005 May 1;12(3):213-227.

44. Aktay L., Johnson A.F., Kroplin B.H. *Numerical modelling of honeycomb core crush behaviour*. Engineering Fracture Mechanics 2008 Jun;75(9):2616-2630.

45. Gotoh M., Yamashita M., Kawakita A. *Crush behavior of honeycomb structure impacted by drop-hammer and its numerical analysis*. Material science research international 1996;2(4):261-266.

46. Li K., Gao X.L., Wang J. *Dynamic crushing behavior of honeycomb structures with irregular cell shapes and non-uniform cell wall thickness*. International Journal of Solids and Structures 2007 Jul;44(14-15):5003-5026.

47. Yang M.Y., Huang J.S., Hu J.W. *Elastic buckling of hexagonal honeycombs with dual imperfections*. Composite Structures 2008 Feb;82(3):326-335.

48. Yang M.Y. and Huang J.S. *Numerical analysis of the stiffness and strength of regular hexagonal honeycombs with plateau borders*. Composite Structures 2004 Apr;64(1):107-114.

49. Simone A.E. and Gibson L.J. *The effects of cell face curvature and corrugations on the stiffness and strength of metallic foams*. Acta Materialia 1998 Jul 1;46(11):3929-3935.

50. Xue Z. and Hutchinson J.W. *Crush dynamics of square honeycomb sandwich cores*. Int J Numer Meth Engng 2006;65(13):2221-2245.

51. Heimbs S., Middendorf P., Kilchert S., Johnson A., Maier M. *Experimental and Numerical Analysis of Composite Folded Sandwich Core Structures Under Compression*. Applied Composite Materials 2007 Nov 1;14(5):363-377.

52. *Implicit Nonlinear (SOL 600) User's Guide*. 2007. MSC Nastran.

53. Thomsen O.T. *Sandwich plates with 'through-the-thickness' and 'fully potted' inserts: evaluation of differences in structural performance*. Composite Structures 1997 Dec 2;40(2):159-174.

54. Thomsen O.T. and Rits W. *Analysis and design of sandwich plates with inserts - a high-order sandwich plate theory approach*. Composites Part B: Engineering 1998 Nov;29(6):795-807.

55. Bozhevolnaya E., Lyckegaard A., Thomsen O., Skvortsov V. *Local effects in the vicinity of inserts in sandwich panels*. Composites Part B: Engineering 2009 Sep;35(6-8):619-627.

56. Bozhevolnaya E. and Lyckegaard A. *Structurally graded core inserts in sandwich panels*. Composite Structures 2005 Apr;68(1):23-29.

57. Skvortsov V., Thomsen O.T. *Analytical estimates for the stress in face sheets of sandwich panels at the junctions between different core materials*. 2002; p. 551-9.

58. Lyckegaard A., Bozhevolnaya E., Thomsen O. *Parametric Study of Structurally Graded Core Junctions*. Journal of Sandwich Structures and Materials 2006;8(5):423-435.

59. Bunyawanichakul P., Castanie B., Barrau J.-J. *Experimental and Numerical Analysis of Inserts in Sandwich Structures*. Applied Composite Materials 2005 May 1;12(3):177-191.

60. Raghu N., Battley M., Southward T. *Strength variability of inserts for composite sandwich panels*.8th International Conference on Sandwich Structures (ICSS 8) 2008.

61. Kim B.J. and Lee D.G. *Characteristics of joining inserts for composite sandwich panels*. Composite Structures 2008 Nov;86(1-3):55-60.

62. Song K.I., Choi J.Y., Kweon J.H., Choi J.H., Kim K.S. *An experimental study of the insert joint strength of composite sandwich structures*. Composite Structures 2008 Nov;86(1-3):107-113.

63. *MIL-HDBK-5H. Metallic materials and elements for aerospace vehicle structures*. 1998. US Department of Defence.

64. Ericksen W.S. *The Bending of a Circular Sandwich Plate Under Normal Load*. Forest Product Laboratory; 1953. Report No.: 1828.

65. Roark R.J. and Young W.C. *Formulas for Stress and Strain*. Pargamon Press; 1975.

66. Finckenor M., Spurrier M. *Design Optimization and Analysis of a Composite Honeycomb Intertank*. 1999. NASA, Marshall Space Flight Centre.

67. Kradinov V., Madenci E., Ambur D.R. *Application of genetic algorithm for optimum design of bolted composite lap joints*. Composite Structures 2007 Jan;77(2):148-159.

68. Kontoleon M.J., Kaziolas D.N., Zygomalas M.D., Baniotopoulos C.C. *Analysis of steel bolted connections by means of a nonsmooth optimization procedure*. Computers & Structures 2003 Oct;81(26-27):2455-2465.

69. *Guidelines for Threaded Fasteners. ESA PSS-030-208*. [1]. 1987. European Space Agency.

70. Karamis M.B. and Selτuk B. *Analysis of the friction behaviour of bolted joints*. Wear 1993 Jun 15;166(1):73-83.

71. Butterworth J. *Finite Element Analysis of Structural Steelwork Beam to Column Bolted Connections*. Constructional Research Unit, School of Science and Technology, University of Teesside; 1995.

72. Jiang Y., Chang J., Lee C.H. *An experimental study of the torque-tension relationship for bolted joints*. International Journal of Materials and Product Technology 2003 Jul 1;16:417-429.

73. Nassar S.A., El-Khiamy H., Barber G.C., Zou Q., Sun T.S. *An Experimental Study of Bearing and Thread Friction in Fasteners*. Journal of Tribology 2005 Apr;127(2):263-272.

74. Williams J. *Engineering Tribology*. Cambridge University Press; 2005.

75. Jiang Y., Zhang M., Park T.W., Lee C.H. *An Experimental Investigation on Frictional Properties of Bolted Joints*. ASME Conference Proceedings 2002 Jan 1;2002(19442):59-66.

76. Blau P.J. *Mechanisms for transitional friction and wear behavior of sliding metals*. Wear 1981 Oct 1;72(1):55-66.

77. Blau P.J. *Friction Science and Technology: From Concepts to Applications*. Marcel Dekker Inc.; 1996.

78. Desai C.S. *Mechanics of Materials and Interfaces*. Amsterdam: Elsevir Science Ltd.; 1986.

79. Jhonson K.L. *Contact Mechanics*. Cambridge: Cambridge University Press; 1985.

80. Martins J.A.C., Oden J.T., Simeos F.M.F. *Recent advances in science - a study of static and kinetic friction*. International Journal of Engineering Science 1990;28(1):29-92.

81. Selvadurai A.P.S. and Boulon M.J. *Mechanics of Geomaterial Interfaces*. Amsterdam: Elsevir Science Ltd.; 1995.

82. Singer I.L., Pollock H. *Fundamentals of Friction: Macroscopic and Microscopic Processes*.

83. Groper M. *Modern Friction Theories as Applied to Bolted Joints*.SEM Spring Conference on Experimental Mechanics June 10-13; p. 892-4.

84. Paslay P.R. and Plunkett R. *Design of Shrink-Fits*. ASME Transactions 1953;75:1199-1202.

85. Nolle H. and Richardson R.S.H. *Static friction coefficients for mechanical and structural joints*. Wear 1974 Apr;28(1):1-13.

86. Bickford H.J. *An Introduction to the Design and Behaviour of Bolted Joints*. New York: Marcel Dekker Inc.; 1981.

87. Gould H.H. and Mikic B.B. *Areas of Contact and Pressure Distribution in Bolted Joints*. Journal of Engineering for Industry 1972;94(3):864.

88. Mayer G., Sterlow D. *Simple Diagrams Aid in Analyzing Forces in Bolted Joints*. 1972. Assembly Engineering.

89. Groper M., Hamelink J. *Clamping Pressure and Friction Distribution in Bolted Joints*.Applied Mechanics and Engineering Science Conference, ASME .

90. Gaul L. and Lenz J. *Nonlinear dynamics of structures assembled by bolted joints*. Acta Mechanica 1997 Mar 29;125(1):169-181.

91. Groper M. *Microslip and macroslip in bolted joints*. Experimental Mechanics 1985 Jun 18;25(2):171-174.

92. Ma X., Bergman L., Vakakis A. *Identification of bolted joints through laser vibrometry*. Journal of Sound and Vibration 2001 Sep 20;246(3):441-460.

93. Koike Y., Tarao K. *An Experimental Study on Slip Strength of HSFG Bolted Joints Treated with High Friction Inorganic Zinc-Rich Paint* Yokogawa Bridge Corp. Research Laboratory; 2011.

94. Plecnik J.M. and Ship J.G. *Bolted Joints on Trans-Alaska Pipeline Structures*. Journal of the Structural Division 1977;103(1):87-104.

95. Lark R.J. *HSFG Bolted Connections using Weathering Steel Materials*. Bridhe Engineering 2004;157(2):103-110.

96. Nah H.-S., Lee H.-J., Kim K.-S. *Establishment of Slip Coefficients of Slip Resistant Connections*.

97. Baylis R.J. *Slip Coefficients for Shear Joints: The Effect of Dynamic Loading and Surface Treatment*.

98. Chang W.R., Etsion I., Bogy D.B. *An Elastic-Plastic Model for the Contact of Rough Surfaces*. Journal of Tribology 1988;109(2):257-263.

99. Koura M.M. *The effect of surface texture on friction mechanisms*. Wear 1980 Aug 15;63(1):1-12.

100. Chang W.R., Etsion I., Bogy D.B. *Static Friction Coefficient Model for Metallic Rough Surfaces*. Journal of Tribology 1988;110(1):57-63.

101. Greenwood J.A. and Williamson J.B.P. *Contact of Nominally Flat Surfaces*. Proceedings of the Royal Society 1966;295(Ser. A):300-319.

102. Handzel-Powierza Z., Klimczak T., Polijaniuk A. *On the experimental verification of the Greenwood-Williamson model for the contact of rough surfaces*. Wear 1992 Apr 15;154(1):115-124.

103. Jeng Y.R. and Peng S.R. *Static Friction Model of Elastic-Plastic Contact Behavior of Surface With Elliptical Asperities*. Journal of Tribology 2009 Apr;131(2):021403-021410.

104. Kogut L., Etsion I. *A Static Friction Model for Elastic-Plastic Contacting Rough Surfaces*.

105. Tsukizoe T. and Hisakado T. *Influence of Surface Roughness on Mechanisms of Friction*. Journal of Lubrication Technology 1970;92(2):264.

106. Fuller K.N.J. and Tabor D. *The Effect of Surface Roughness on the Adhesion of Elastic Solids*. Proceedings of the Royal Society 1975;A345:327-342.

107. Gadelmawla E.S. *Roughness Parameters*. Journal of Materials Processing Technology 2002;123(1):133-145.

108. Lundberg J. *Influence of surface roughness on normal-sliding lubrication*. Tribology International 1995 Aug;28(5):317-322.

109. Menezes P.L., Kishore, Kailas S.V. *Influence of surface texture and roughness parameters on friction and transfer layer formation during sliding of aluminium pin on steel plate*. Wear 2009 Sep 9;267(9-10):1534-1549.

110. Frank K.H., Yura J.A., Fouad F.H. *Bolted Shear Connectioins with Painted Surfaces*. Engineering Journal-American Institute of Steel Construction 1984;21(3):171-184.

111. Yura J.A. and Frank K.H. *Testing Method to Determine the Slip Coefficient for Coatings Used in Bolted Joints*. Engineering Journal-American Institute of Steel Construction 1985;22(3):151-155.

112. Lusher A.F., Lee S.C., Frysinger C. *Increasing Abutment Friction at Bolted Joint Interfaces through Particle Enhanced Sealants*. International Journal of Vehicle Design 2002;29(3):288-306.

113. *MIL-HDBK-23 A. Structural Sandwich Composites*. 1986. US Department of Defence.